5-2012

Modeling Spatial Surface Energy Fluxes of Agricultural and Riparian Vegetation Using Remote Sensing

Hatim M.E. Geli
Utah State University

MODELING SPATIAL SURFACE ENERGY FLUXES OF AGRICULTURAL AND RIPARIAN VEGETATION USING REMOTE SENSING

by

Hatim Mohammed Eisa Geli

A dissertation submitted in partial fulfillment
of the requirements of the degree

of

DOCTOR OF PHILOSOPHY

in

Civil and Environmental Engineering

Approved:

Christopher M. U. Neale Major Professor	David G. Tarboton Committee Member
Mac Mckee Committee Member	Luis A. Bastidas Committee Member
Lawrence E. Hipps Committee Member	Mark R. McLellan Vice President for Research and Dean of the School of Graduate Studies

UTAH STATE UNIVERSITY
Logan, Utah

2012

ABSTRACT

Modeling Spatial Surface Energy Fluxes of Agricultural and

Riparian Vegetation Using Remote Sensing

by

Hatim M. E. Geli, Doctor of Philosophy

Utah State University, 2012

Major Professor: Dr. Christopher M. U. Neale
Department: Civil and Environmental Engineering

Modeling of surface energy fluxes and evapotranspiration (*ET*) requires the understanding of the interaction between land and atmosphere as well as the appropriate representation of the associated spatial and temporal variability and heterogeneity. This dissertation provides new methodology showing how to rationally and properly incorporate surface features characteristics/properties, including the leaf area index, fraction of cover, vegetation height, and temperature, using different representations as well as identify the related effects on energy balance flux estimates including *ET*.

The main research objectives were addressed in Chapters 2 through 4 with each presented in a separate paper format with Chapter 1 presenting an introduction and Chapter 5 providing summary and recommendations. Chapter 2 discusses a new approach of incorporating temporal and spatial variability of surface features. We coupled a remote sensing-based energy balance model with a traditional water balance

method to provide improved estimates of *ET*. This approach was tested over rainfed agricultural fields ~ 10 km by 30 km in Ames, Iowa. Before coupling, we modified the water balance method by incorporating a remote sensing-based estimate for one of its parameters to ameliorate its performance on a spatial basis. Promising results were obtained with indications of improved estimates of *ET* and soil moisture in the root zone.

The effects of surface features heterogeneity on measurements of turbulence were investigated in Chapter 3. Scintillometer-based measurements/estimates of sensible heat flux (*H*) were obtained over the riparian zone of the Cibola National Wildlife Refuge (CNWR), California. Surface roughness including canopy height (h_c), roughness length, and zero-plane displacement height were incorporated in different ways, to improve estimates of *H*. High resolution, 1-m maps of ground surface digital elevation model and canopy height, h_c, were derived from airborne LiDAR sensor data to support the analysis.

The effects of using different pixel resolutions to account for surface feature variability on modeling energy fluxes, e.g., net radiation, soil, sensible, and latent heat, were studied in Chapter 4. Two different modeling approaches were applied to estimate energy fluxes and *ET* using high and low pixel resolution datasets obtained from airborne and Landsat sensors, respectively, provided over the riparian zone of the CNWR, California. Enhanced LiDAR-based h_c maps were also used to support the modeling process. The related effects were described relative to leaf area index, fraction of cover, h_c, soil moisture status at root zone, groundwater table level, and vegetation stress conditions.

(182 pages)

PUBLIC ABSTRACT

Modeling Spatial Surface Energy Fluxes of Agricultural and Riparian Vegetation Using Remote Sensing

Evapotranspiration (*ET*) represents the amount of water consumed by vegetation through transpiration plus the direct evaporation from the soil surface. Understanding the amount of *ET* is important as it represents a portion of fresh water that is consumed and not available for further use. *ET* is used as indication of how much water needed for agricultural activities. This research is aimed towards providing improved estimates of *ET*.

The technological advances in remote sensing provide us with images of the Earth's surface from space, using satellites, and sometimes with more detail from aircraft. We used these data in models to estimate *ET* for different land surface cover, including agricultural and natural vegetation. The research objectives were achieved as described in specific technical papers presented in Chapters 2 through 4. Chapter 1 provided a general introduction and Chapter 5 presented a summary and recommendations for future research. In Chapter 2 we introduced new method to estimate daily *ET* for an entire growing season of rainfed corn and soybean fields of about 10 km by 30 km in Ames, Iowa. This method allowed us to improve our knowledge about how much water is available in the soil in agriculture that depends on natural precipitation.

In Chapters 3 and 4 we studied the ability of using this remote sensing data and other related methods to estimate *ET* over natural vegetation such as riparian zones that exist within river floodplains. This part of the analysis was carried out over a naturally

vegetated area of about 5 km^2 at the Cibola National Wildlife Refuge in southern California. This area is covered with invasive vegetation species namely tamarisk (saltcedar) trees that consume considerable amounts of water. We compared estimates of *ET* which were obtained from using different methods and models.

The research findings provided improved estimates of *ET* over natural and agricultural area that can be used to better the way we manage our water resources. It also corroborated the usefulness of remote sensing information in this type of application.

(182 pages)

ACKNOWLEDGMENTS

I am grateful to my parents, Mohammed and Samira, for their spiritual endless support and to whom I dedicated my dissertation. My complete appreciation for all kinds of support I received from my sister, Nashwa, brother, Yasir, and their families. Special thanks to my beloved family, my dear wife, Ruba, and my adored son, Mohammed, for their patience and supportive and joyful environment they provided throughout the time till the completion of this work.

I am truly indebted to Dr. Christopher M. U. Neale for his endless guidance, support, understanding in various topics as a major advisor, and as a true friend. Whom without his intelligent directions this would not have been completed.

Special thanks to Dr. Lawrence E. Hipps, Dr. David Tarboton, Dr. Mac Mckee, and Dr. Luis A. Bastidas who served as members of my committee and through their support, comments, and suggestions made my research even stronger.

It is an honor talking to, and having fruitful discussions with, Dr. William P. Kustas and Dr. Martha C. Anderson of the USDA-ARS about the application of the two-source model. Our discussions enlightened me throughout my work. My deepest gratitude to Dr. Henk De Bruins and Wim Kohsiek for their valuable comments and suggestions on the application of scintillometry. Thanks to Dr. Doyle Watts of WSU, Dr. Robert T. Pack of USU, and John Osterberg of the USBR for being keen and patient in providing vital research information as well as intellectual support.

I am obliged to my colleagues at the Remote Sensing Services Laboratory, Daniele Zaccaria, Saleh Taghvaeian, Saravanan Sivarajan, Ashish Masih, and Jonna van Opstal, for the friendly environment they provided.

Thanks to Utah Water Research Laboratory (UWRL) and the Remote Sensing Services Laboratory (RSSL) for their logistic and financial support, which made the completion of this work possible. Also, thanks to the Water Initiative program at Utah State University for their support in text books.

This research has been supported in part by the UWRL, USBR through a contract with the Alliance of Universities, through Central State University, Wilburforce, Ohio, under grant # 04FC811041, and the RSSL with computer and field equipment and remote sensing data.

Hatim M. E. Geli

CONTENTS

LIST OF TABLES

LIST OF FIGURES

CHAPTER 1

INTRODUCTION

The exchange of energy, mass, and momentum are the main processes through which the surface and the atmosphere interact (Arya 2001). These processes evolve due to the turbulence transfer mechanism and are significantly noticed near the Earth's surface within what's called as the Atmospheric Boundary Llayer (ABL). The ABL represents about one-tenth of the troposphere layer and encompasses the signature of the surface features (Brutsaert 1982; Arya 2001). The exchange processes for a surface are usually examined in a layer close to the surface that extends on the order of 10 m above the ground. The radiation and energy balance at or near the surface plays an important role in driving these exchange processes supplying the energy to do work. These processes can occur at different spatial scales including micro, macro, and mesoscales and each is important depending on the type of the application. This research is limited to processes occurring at the microscale or local scale.

The surface energy balance fluxes (SEBF) are the net radiative flux or net radiation (*Rn*), the soil (*G*), the sensible (*H*), and the latent (*LE*) heat fluxes that are usually considered in the simplified form of the energy balance equation under a short averaging period. Note there are other fluxes in the surface energy balance that can generally be neglected such as energy used for photosynthesis or storage of energy by vegetation. *Rn* is partitioned into fluxes of energy following the energy balance equation : $Rn = G + H + LE$. *Rn* results from the balance of the incoming and outgoing shortwave and longwave radiation at the surface. *G* represents the heat flux into or out from the soil medium due the temperature differences between the soil surface and the sub-medium. *H*

is the turbulence flux to or from the surface due to difference in temperatures of the surface and the air. *LE* is the flux of latent heat at the surface due to evaporation of water and represents a measure of *ET*.

Estimates of these fluxes are required for wide range applications. For example spatial SEBF are used as a boundary conditions in weather forecasting and climate modeling (Warner 2011), air pollution meteorology (Arya 2001), and hydrological modeling and water budget (Schmugge and Andre 1991) to name but a few. In this dissertation we consider a modeling approach to obtain *LE* from the other fluxes of the energy balance equation, as it is considered one of the major components of the global water cycle. In general, it represents the main consumptive use of water, so reliable estimates of *LE* or *ET* are necessary for improved water resources management.

The dependency of these fluxes on the type of land surface makes the need to obtain information about the Earth's surface features at a reasonable accuracy and appropriate temporal and spatial scales inevitable. Such spatial information can now be obtained by the means of remote sensing from a suite of systems. Fortunately spaceborne/extraterrestrial satellites provide routine snapshots of the Earth's surface, providing near real time data. For example, the Moderate Resolution Imaging Spectroradiometer (MODIS) can provide visible and thermal infrared hourly and daily images for the entire globe and the Land Remote-Sensing Satellite (Landsat) provides a 16-day re-visit for the exact same location on Earth. This is useful in obtaining seasonal estimations of SEBF and *ET* required in many applications especially for global and regional energy/water balance studies. However, this data is available at different spatial resolutions that affect the way the features on the surface are being represented (Norman

et al. 2003; Kustas et al. 2004). For example MODIS image data are available at 250 m to 1 km pixel resolution at a 2-3 day frequency, Landsat provides 30-120 m every 16 days,while airborne sensors can provide high resolution imagery at the sub-meter scale. These wide ranges of temporal and spatial scales in remote sensing data are generally due to sensor configurations and altitude.

Taking advantage of these remote sensing data, spatial estimates of SEBF and *ET* can be obtained by applying different models available in literature if required data inputs are available. The application of most of these models requires knowledge about certain surface features and their properties/characteristics. These properties/characteristics may include surface type, leaf area index (*LAI*), fraction of cover (f_c), vegetation height (h_c), and surface temperature. A reasonable level of accuracy and representativeness is required for these model inputs in order to provide reliable estimates (Kustas et al. 2003, 2004; Norman et al. 2003). Over homogeneous surfaces such as croplands, especially when the crops are at full cover, it might not be an issue to obtain such information from relatively low pixel resolution imagery, e.g. 30-120 m (Kustas et al. 2003, 2004). Such pixel resolutions can capture the field to field differences (Kustas et al. 2004). At the early growing stages of crop growth, sparse vegetation conditions may exist that might not be well represented using typical available pixel resolutions of extraterrestrial sensors. Over semi-arid naturally vegetated areas it becomes an issue in how to well represent the surface heterogeneity as vegetation tends to be randomly distributed over the surface and interspersed with bare soil (Kustas and Norman 2000; Norman et al. 2003). This reflects typical surface conditions over naturally vegetated areas such riparian

zone of rivers. A relatively higher pixel resolution of < 30 m might be needed over such areas (Kustas and Norman 2000; Kustas et al. 2004).

The temporal variability of surface features properties/characteristics also needs to be considered in modeling *ET*. This is generally accomplished by using the available routine remote sensing data from different sensors such as GOES, MODIS, and Landsat . However, the presence of clouds during some days over an area of interest sometimes makes these data of a limited use and can increase the overpass period from ~16 days to 4 weeks or more in the case of the Landsat sensors (Norman et al. 2003). To overcome this problem, airborne sensors are used to provide intermediate on demand data to assure the consideration of a reasonable temporal coverage (Norman et al. 2003). Despite its high temporal resolution (~daily) the use of MODIS data is limited due to its coarse resolution (1 km) which is not sufficient for agriculture and riparian vegetated areas (Kustas et al. 2004). Over such areas a pixel resolution of about 30-60 m can provide relatively reasonable coverage of surface features (Kustas et al. 2004) so data from Landsat are preferred most of the time for modeling *ET*. However, estimates of *ET* on a daily bases are hindered due to its coarse temporal coverage.

As this dissertation is aimed towards providing improved understanding of the land atmosphere interaction it particularly focuses on how to well the energy exchange within the soil-vegetation-atmosphere interface can be modeled considering the inherent spatial and temporal variability of cropped and naturally vegetated systems. The following questions formulate the research objectives to be achieved:

a) What is the effect of the spatial resolution of the remote sensing data on the modeled surface energy fluxes in riparian vegetation? Will the use of higher spatial resolution as 1-4 m improve estimates of surface energy fluxes or will it overwhelm the models with too much information considering most models that rely on remote sensing data were developed during the era of relatively low pixel resolution?

b) What would be the effect of coupling a traditional approach of modeling soil water balance and a remote sensing based method of estimating SEBF, specifically exploring their ability in capturing the inherent temporal and spatial variability of surface features, for providing seasonal estimates of *ET* over agricultural areas?

This dissertation is organized into five chapters with the three middle chapters addressing the main research objectives, Chapter 1 is this introduction, with an overall summary and conclusions statement provided in Chapter 5.

Chapter 2 deals with the issue of how to capture both temporal and spatial variability of surface features for improved estimates of *ET*. Two different modeling approaches were coupled, namely the two source energy balance (TSEB) (Norman et al. 1995) and the traditional and impirical " crop coefficient" method of FAO Paper 56 of the Food and Agriculture Organization [here-in called FAO-56] (Allen et al. 1998). The TSEB is a soil-vegetation-atmosphere scheme based on applying the energy balance equation using thermal remote sensing techniques (Norman et al. 1995). As most models of a similar nature, the TSEB uses radiometric surface temperature as key boundary condition to estimate surface energy fluxes on a diagnostic basis (Kustas et al. 2004).

This approach proves to better handle a wide range of surface heterogeneity (Anderson et al. 2011). By extrapolating instantaneous fluxes of *LE* to daily values we obtained spatial estimates of *ET* at intervals of ~7 days using Landsat and airborne datasets. The missing *ET* estimates in between satellite overpass dates were filled by coupling the TSEB model with the FAO-56 model.

We used the traditional FAO-56 method to obtain seasonal estimates of crop *ET* using the crop coefficient approach which is denoted by ET_c. This method basically relates ET_c to reference crop *ET* (ET_o) with crop coefficients (K_c) (Allen et al. 1998). We estimated ET_o using the Penman-Monteith equation based on grass reference crop. The use of tabulated values for K_c in Allen et al. (1998) could result in misrepresentation of the spatial growing pattern variability. Instead we incorporated spatial estimates of K_{cbrf} which is a reflectance based basal crop coefficient (K_{cb}) obtained from remote sensing (Neale et al. 1989; Bausch 1993). K_{cbrf} were obtained during satellite overpass dates and linear interpolation applied to get values during the period in between. K_{cbrf} estimates are an improvement over tabulated K_c since they are not simply a function of the crop development stages, but instead describe the actual field growing conditions, and capture the spatial and temporal variability of the growing pattern within the same field (Wagner et al. 2003; Neale et al. 2005; Hunsaker et al. 2007). Note that the FAO-56 method is a water balance based approach that requires updates of soil moisture status in the root zone. Hence coupling of these two methods resulted not only in improved estimates of *ET* but also the soil moisture of the root zone.

The effects of land surface topography, vegetation aerodynamic roughness, and spatial heterogeneity on turbulence based measurements of *H* using a large aperture

scintillometer (LAS) is presented in Chapter 3. Scintillometer measurements of turbulence are generally used in hydrological, micrometeorological, agricultural, and water resources studies. These systems are able to provide measurements of H that cover large spatial scales up to ~10 km (Kohsiek et al. 2006), effectively and efficiently, depending on the type of instrument, compared to Bowen ratio (BR) and eddy covariance (EC) methods that generally provide estimates at scales of ~100s of meters. Scintillometers were initially parameterized and applied over ideal homogenous surfaces, horizontal beam path, and flat terrain. Their use over heterogonous surfaces and non-flat terrain is challenging and, in some cases, provide less accurate estimates of surface energy fluxes (Hartogensis et al. 2003).

We tested its application over a surface characterized with moderate heterogeneity. We used measurements obtained over a riparian zone covered mostly with tamarisk trees interspersed with bare soil at the Cibola National Wildlife Refuge (CNWR), California. The area is characterized with aridity conditions, dry soil surface, variable soil moisture status in the root zone, and a highly variable tree heights. The analysis was supported by using high spatial resolution 1-m topographic and canopy height maps obtained from Light Detection and Ranging (LiDAR) remote sensing. This was an original application of these combined technologies. As scintillometry requires knowledge about surface roughness we tested its measurements by using different representations of canopy height (h_c), zero-plane displacement height (d), roughness length (z_0), and LAS beam effective height (z_{eff}). The study used simple average, path-weighted, and LAS 3D footprint integrated values for these parameters. It was found that using LAS 3D footprint analysis provided the best represent of surface feature

heterogeneity and hence improved LAS-based estimates of *H* as compared to BR measurements.

Chapter 4 examines the effects of using different pixel resolutions to represent surface features when modeling energy exchange in the soil-vegetation-atmosphere transfer interface through estimates of SEBF/*ET*. The thermal remote sensing based approach was used, namely the TSEB (Norman et al. 1995), and the traditional Matt-Shuttleworth (M-S) method (Shuttleworth 2006) –a modified version of the Penman-Montieth equation as the modeling framework. The TSEB requires knowledge about canopy height h_c, *LAI*, fraction of vegetation cover f_c, and surface temperature. The M-S method depends mostly on h_c and stomatal conductance r_s. Satellite and airborne remote sensing datasets at 30-60 m and 1-4 m pixel resolution, respectively, were used along with h_c maps at 1-m resolution derived from LiDAR. These data were acquired over the riparian zone of the CNWR which had heterogeneous surface conditions suitable to test the SEBF and models.

This research provided a) a new method of coupling surface and sub-surface energy and soil moisture exchanges in the soil-vegetation-atmosphere interface, b) quantifying the associated effects of the representation of surface spatial and temporal variability, c) methods and indications of how to well incorporate surface heterogeneity in the modeling phase.

References

Allen, R. G., L. S. Pereira, D. Raes, and M. Smith, 1998: *Crop evapotranspiration: Guidelines for computing crop water requirements.* Paper No. 56. Food and Agricultural Organization of the UN, 328 pp.

Anderson, M. C., W. P. Kustas, J. M. Norman, C. R. Hain, J. R. Mecikalski, L. Schultz, M. P. Gonz´alez-Dugo, C. Cammalleri, G. d'Urso, A. Pimstein, and F. Gao, 2011: Mapping daily evapotranspiration at field to continental scales using geostationary and polar orbiting satellite imagery. *Hydrol. Earth Syst. Sci.*, **15,** 223–239.

Arya, S. P., 2001: *Introduction to Micrometeorology*, 2nd edit. Academic Press, 420 pp.

Bausch, W. C., 1993: Soil background effects on reflectance-based crop coefficients for corn. *Remote Sens.Environ.,* **46,** 213–222.

Brutsaert, W., 1982: *Evaporation into the Atmosphere: Theory, History, and Applications.* Springer, 299 pp.

Hartogensis, O. K., C. J. Watts, J. -C. Rodriguez, & H. A. R. De Bruin, 2003: Derivation of an effective height for scintillometers: La Poza experiment in northwest Mexico, *J. Hydrometeor.,* **4,** 915–928.

Hunsaker, D. J., G. J. Fitzgerald, A. N. French, T. R. Clarke, M. J. Ottman, & P. J. Pinter Jr., 2007: Wheat irrigation management using multispectral crop coefficients: I. Crop evapotranspiration prediction. *Trans.Amer. Soc. Agric. Biolog. Eng.,* **50(6),** 2017–2033.

Kohsiek, W., W. M. Meijninger, H. A. R. De Bruin, & F. Beyrich, 2006: Saturation of the large aperture scintillometer. *Bound.-Layer Meteor.*, **121,** 111–126.

Kustas, W. P., & J. M. Norman, (2000). Evaluating the effects of subpixel heterogeneity on pixel average fluxes. *Remote Sens. Environ.*, **74,** 327– 342.

Kustas, W. P., F. Li, T. J. Jackson, J. H. Prueger, J. I. MacPherson, & M. Wolde, 2004: Effect of remote sensing pixel resolution on modeled energy flux variability of cropland in Iowa. *Remote Sens. Environ.*, **92,** 545–547.

Kustas, W. P., J. M., Norman, M. C. Anderson, & A. N. French, 2003: Estimating subpixel surface temperatures and energy fluxes from the vegetation index – radiometric temperature relationship. *Remote Sens. Environ.*, **85,** 429– 440.

Neale, C. M. U., H. Jayanthi, & J. L. Wright, 2005: Irrigation water management using high resolution airborne remote sensing. *Irrig. Drain. Syst.*, **19,** 321–336.

Neale, C. M. U., W. C. Bausch, & D. F. Heermann, 1989: Development of reflectance-based crop coefficients for corn. *Trans. Amer. Soc. Agric.Biolog. Eng.*, **32(6),** 1891–1899.

Norman, J. M., W. P. Kustas, & K. S. Humes, 1995: A two-source approach for estimating soil and vegetation energy fluxes in observations of directional radiometric surface temperature. *Agric. Forest Meteor.,* **77,** 263–293.

Norman, J. M., M. C. Anderson, W. P. Kustas, A. N. French, J. Mecikalski, R. Torn, G. R. Diak, T. J. Schmugge, & B. C. W. Tanner, 2003: Remote sensing of surface energy fluxes at 10^1-m pixel resolutions. *Water Resour. Res.,* **39(8),** 1221, doi:10.1029/2002WR001775.

Schmugge, T. J., & J.-C. Andre, 1991: *Land Surface Evaporation Measurements and Parameterization*. Springer-Verlag, 424 pp.

Shuttleworth, W. J., 2006: Towards one-step estimation of crop water requirements, *Irrig. Drain. Syst.,* **49,** 925–935.

Wagner, D. G., R. M. Hoffer, & T. H. Podmore, 2003: Determination of consumptive water use for river basins by remote sensing and GIS techniques. *Irrig. Drain. Syst.,* **46(6),** 1515–1523.

Warner, T. T., 2011: *Numerical Weather and Climate Prediction*. Cambridge University Press, 548 pp.

CHAPTER 2

A HYBRID APPROACH FOR IMPROVED ESTIMATES OF EVAPOTRANSPIRATION AND SOIL MOISTURE OF THE ROOT ZONE IN AGRICULTURAL AREAS USING REMOTE SENSING AND DATA ASSIMILATION TECHNIQUES[1]

Abstract

Two different models that utilize remote sensing data inputs and techniques are combined to form the Hybrid Evapotranspiration (HET) approach that provides improved spatio-temporal estimates of evapotranspration (*ET*). The first is a Soil Vegetation Atmosphere Transfer (SVAT) model namely the two-source model (TSM) with the series resistance formulation which was used to provide spatial diagnostic estimates of the actual *ET* (ET_{TSM}). The second is the water balance (WB) model of the root zone of the traditional FAO-56 approach used to provide prognostic estimate of *ET* (ET_{WB}) and soil moisture (SM_{WB}) on daily basis. A modification to the WB model is introduced by using the reflectance based basal-crop coefficient (K_{cbrf}) estimated from remote sensing techniques instead of the tabulated averaged values basal-crop coefficient (K_{cb}).

The HET approach basically utilizes the same remote sensing imagery in a hybrid form to estimate ET_{TSM} and at the same time it estimates the K_{cbrf} which are used to estimate ET_{WB}. A data assimilation technique is then implemented to assimilate ET_{TSM} into WB model. This approach is applied over rainfed agricultural area planted with corn and soybean crops near Ames, Iowa, using data from the Soil Moisture-Atmosphere Coupling Experiment (SMACEX) conducted during the summer of 2002. The data assimilation resulted in improved estimate of the actual *ET* and the SM of the root zone.

[1] Co-authored by Hatim M. E. Geli, Christopher M. U. Neale, William P. Kustas

Estimates of *ET* resulted in a RMSE of 1.26 and 0.67 mm day^{-1}, before and after assimilation, respectively. These promising results can potentially lead to improved estimates of crop water requirements, managing of water resources, and help in better diagnosing actual crop growing conditions and yield estimation in rainfed areas.

2.1 Introduction

The significant amount of research and effort made throughout the past two decades to obtain a high level of accuracy for evapotranspiration (*ET*) estimates on temporal and spatial basis rises from its importance in all aspects of water resources. In the field of agriculture, reliable estimates of spatially distributed *ET* is used as a diagnostic tool to aid in the detection of water and other kinds of stresses in cropped fields. Also, temporal and/or seasonal estimates of *ET* can provide improved crop water demand for irrigation scheduling, water distribution and assessing the impacts of drought.

The traditional method to obtain seasonal estimates of crop *ET* (ET_c) of the Food and Agricultural Organization (FAO) paper 56 [here after FAO-56] by Allen et al. (1998) has been the core of practical application in the field of agriculture and water resources management. This method basically relates ET_c to reference crop *ET* (ET_o) and crop coefficient (K_c) (Doorenbos and Pruitt 1977; Wright 1982; Allen et al. 1998). Generally, ET_o is estimated using the Penman-Monteith reference evapotranspiration equation for a reference crop such as grass or alfalfa assumed to grow under optimal water and health conditions. The tabulated values of K_c reported for most crops (Allen et al. 1998) are estimated based on crop characteristics and development stages assuming optimal agronomical conditions. However, to incorporate local climatic and agronomical conditions**,** recommendations such as those suggested by Allen et al. (1998) need to be

followed, although they might not fully represent actual local conditions (Neale et al. 1989). Furthermore, these tabulated K_c values essentially represent average crop growth conditions and do not reflect the spatial variability within the fields or variation due to the climatic region being studied. These concerns in obtaining reliable estimates for ET_c have resulted in numerous investigations into different methods to improve estimates of ET_c as well as K_c (Li et al. 2005; Bausch and Neale 1987; Neale et al. 1989).

Improved estimates of K_c have been explored through the application of remote sensing which then led to the development of relationships between vegetation indices (VI) and both K_c and the basal crop coefficient (K_{cb}). This is now known as reflectance-based crop coefficient (K_{crf}) and reflectance-based basal crop coefficient (K_{cbrf}) techniques. There have been K_{cbrf} values derived for wheat by Hunsaker et al. (2005), corn by Neale et al. (1989) and Bausch (1993), potatoes (Jayanathi et al. 2007), and several other crops by Tasumi et al. (2005). The K_{crf} and K_{cbrf} estimates are an improvement over tabulated K_c since they are not simply a function of the crop development stages, but instead describe the actual field growing conditions, and capture the spatial and temporal variability of the growing pattern within the same field (Wagner et al. 2003; Neale et al. 2005; and Hunsaker et al. 2007). Also recently Shuttleworth (2006) suggested a methodology to eliminate the need to use K_c to estimate ET_c following the FAO-56 approach. In his work he formulated a surface aerodynamic resistance approach that can be used for all types of crops and applied for all climatic conditions.

In order to provide spatially-distributed maps of *ET*, there have been numerous remote sensing-based methods developed (Kalma et al. 2008). Crow et al. (2005) defined two classes of models. The first class uses thermal-infrared remote sensing as the key

surface boundary condition to model energy exchange in the soil-vegetation-atmosphere interface (herein referred to as RS-SVAT). The other class couples water and energy balance to simulate changes in the soil moisture in the root zone (herein referred to as WEB-SVAT). The RS-SVAT models utilize radiometric temperature (T_R) to estimate surface energy fluxes in a diagnostic way. While the WEB-SVAT models use rainfall observations as the key input to estimate surface temperature, energy fluxes, and water content in the soil profile and considered as prognostic tool. Examples of RS-SVAT scheme include one-source modeling approaches such as the Surface Energy Balance Index (SEBI) (Menenti and Choudhury 1993), the Surface Energy Balance (SEBAL) (Bastiaanssen et al. 1998), the Mapping EvapoTranspiration with Internalized Calibration (METRIC) (Allen et al. 2005, 2007), and two-source modeling schemes which includes the Two-Source Model (TSM) (Norman et al. 1995) and the Atmosphere-Land Exchange Inverse (ALEXI) (Anderson et al. 1997, 2007). The model implemented in this study is the TSM by Norman et al. (1995) with its recent modifications by Kustas and Norman (1999, 2000) and Li et al. (2005). The TSM provides instantaneous spatial estimates of surface energy fluxes including the latent heat flux which can be converted to equivalent estimates of *ET*.

As soil moisture (SM) plays a significant role in the estimation of *ET* (Allen et al. 1998), understanding of the spatial and temporal variability of this variable is crucial for improved estimates of both SM and *ET*. The FAO-56 approach bases its estimation of *ET* on modeling the water balance in the root zone assuming that the SM for the entire root zone is represented by a single averaged value. Generally, an average value of the SM for the root zone will not represent its actual variability. A more representative and accurate

approach would be to provide estimates of the SM at multiple soil layers (Feddes et al. 1978; Li et al. 2001). Such estimates are important especially in rainfed agricultural areas that have greater potential to develop water stress conditions. Such estimates of SM can be obtained using models simulating soil moisture dynamics in the profile (Feddes et al. 1978; Li et al. 2001). Different levels of complexity exist for soil moisture dynamics models depending on the type of the application and the required inputs. Examples of soil moisture dynamics models include the Soil Water and Actual Transpiration Rate Extended (SWATRE) for the simulation of field water use and crop yield by (Feddes et al. 1976, 1978; Bastiaanssen et al. 1996), the soil water and salt balance model BUDGET (Raes 2002), the Soil-Water-Atmosphere-Plant (SWAP) (Van Dam et al. 1997; Li et al. 2001, 2006), and the modeling approach implemented in the simple biosphere model (SiB) (Sellers et al. 1986; Luo et al. 2003). In this study the modeling approach described by Sellers et al. (1986) and Luo et al. (2003) is implemented to estimate the soil moisture for multiple layers in the root zone. This model was chosen because it allows for the inclusion of a recently updated root distribution and water uptake models by Li et al. (2006) developed specificaly for cropped lands, as well as its ability to multiple specifiy soil layer depths. The model is applied on a daily time step for the entire year of 2002 taking into account the spatial and temporal variability of the hydroclimatological variables and soil properties.

Data assimilation (DA) techniques are heavily used in the analyses of atmospheric states, oceanography, and climatological studies (Daley 1991). Different DA methods in the literature are applied based on the complexity and objectives of the problems being studied. Among these methods are the nudging or Newton Relaxation, direct insertion,

and the statistical interpolation (Hoke and Anthes 1976; Stauffer and Seaman 1990; Daley 1991). Examples of application of DA in the field of land observations include assimilation of RS-SVAT model results into WEB-SVAT model for improved soil moisture prediction by Crow et al. (2008). Schuurmans et al. (2003) assimilated RS-SVAT model estimates into hydrological models for improved water balance calculations. Meijerink et al. (2005) provided improved water balance calculation for watershed scale study using inputs from RS-SVAT in irrigated and wetland region. Also Houser et al. (1998) applied different DA methods with one of the RS-SVAT models to synthesize soil moisture in a hydrological model. In this study we used the statistical interpolation (SI) method which is considered a simplified case of Kalman filter (Daley 1991).

Estimates of *ET* from the TSM and the FAO-56 WB in combination with K_{cbrf} method are considered independent RS-SVAT and WEB-SVAT schemes, respectively. Through DA techniques, it is possible to combine these modeling schemes in order to obtain estimates of *ET*. So can the coupling of these two models lead to improvements in spatial and temporal estimates of *ET*?

In this paper we introduce the Hybrid EvapoTranspiration (HET) approach to provide spatio-temporal estimates of *ET* through the combination of estimates of *ET* from TSM with those from the modified WB calculation of the FAO-56 approach. In addition to providing estimates of *ET*, HET approach also provides estimates of SM of the crop root zone.

2.2 Methodology

2.2.1 Estimation of spatial *ET* using TSM

The original TSM with the series resistance formulation of Norman et al. (1995) has been extensively reviewed in different aspects to improve its performance over different climate regions and vegetation conditions.

Generally, the TSM separates the surface into soil and vegetation canopy components and solves the energy balance equation for each. At a level above the ground surface called the air-canopy interface, the energy fluxes of each component are then combined to represent the total surface energy fluxes. One of the recent modifications to the TSM with the series resistance formulation is the use of the physically based model developed by Campbell and Norman (1998) for the decomposition and estimation of the soil and canopy components of the net radiation Rn_s and Rn_c, respectively (Kustas and Norman, 2000; Li et al. 2005), which can be estimated using Eqs. (1)–(2) as

$$Rn_c = Ln_c + (1-\tau_s)(1-\alpha_c)S \tag{1}$$

$$Rn_s = Ln_s + \tau_s(1-\alpha_s)S \tag{2}$$

where Ln_c and Ln_s are the longwave radiation of the canopy and soil components, respectively, estimated using Eqs. (3)–(4), α_s the soil albedo, α_c the canopy albedo, τ_s the solar transmittance in the canopy, and S the incoming solar radiation.

$$Ln_c = [1-\exp(-k_L \Omega LAI)][L_{sky} + L_c + L_s] \tag{3}$$

$$Ln_s = \exp(-k_L \Omega LAI)L_{sky} + [1-\exp(-k_L \Omega LAI)]L_c + L_s \tag{4}$$

where k_L is an extinction coefficient, L_{sky}, L_c, and L_s the longwave radiation from the sky, canopy, and soil, calculated based on air, canopy, and soil temperatures, respectively, *LAI*

the leaf area index estimated following Anderson et al. (2004),and Ω the clumping factor estimated using Eq. (5) as function of the sun zenith angle (θ). Vegetation clumping can significantly affect the partitioning of radiometric surface temperature and heat fluxes (Li et al. 2005).

$$\Omega(\theta) = \frac{\Omega(0)\Omega(90)}{\Omega(0) + [\Omega(90) - \Omega(0)]\exp(k\theta^P)} \tag{5}$$

where k is an empirical coefficient equal to -2.2, p an empirical coefficient equal to 3.8-0.46D with D represents the ratio of vegetation height to width of clumps, $\Omega(90) \approx 1.0$, and $\Omega(0)$ the clumping factor when canopy viewed at nadir. The $\Omega(0)$ is estimated from the general knowledge and the definition of fraction of vegetation cover occupying the row (f_{veg}) and soil gap (f_{gap}) (i.e. bare soil seen through canopy elements along the row). The total fraction of canopy gap (i.e. bare soil seen at nadir) equals to $exp\ (-0.5\Omega(0)\ LAI/cos(0))$. Also, the total fraction of bare soil seen at nadir equals the sum of the fraction of bare soil area in the inter-row ($1-f_{veg}$) plus the fraction of bare soil seen through vegetation ($f_{veg}f_{gap}$) (Kustas and Norman 2000; Li et al. 2005). Thus,

$$(1 - f_{veg}) + f_{veg} f_{gap} = \exp\left(\frac{-0.5\Omega(0)LAI}{\cos(0)}\right) \tag{6}$$

$$f_{gap} = \exp\left(\frac{-0.5LAI_L}{\cos(0)}\right) \tag{7}$$

$$f_{veg} = \left(\frac{NDVI - NDVI_{\min}}{NDVI_{\max} - NDVI_{\min}}\right)^2 \tag{8}$$

where $NDVI_{min}$ and $NDVI_{max}$ are the normalized vegetation index (NDVI) for bare soil and for full vegetation cover, respectively. For the current study $NDVI_{min} = 0.10$ and $NDVI_{max} = 0.925$.

Also, the clumping factor as a function of the view zenith angle (ϕ) is used in the decomposition of the surface radiometric temperature, T_R, into soil and canopy temperatures T_s and T_c, respectively, as described in Eq. (9).

$$T_R(\phi) \approx \left[f_c(\phi) T_c^4 + (1 - f_c(\phi)) T_s^4 \right]^{1/4} \tag{9}$$

where $f_c(\phi)$ is the fraction of vegetation cover as function of ϕ estimated using Eq. (10).

$$f_c(\phi) = 1 - \exp\left(\frac{-0.5 \Omega LAI}{\cos(\phi)} \right) \tag{10}$$

Furthermore, the effect of vegetation clumping appears in the calculation of the wind speed above the soil surface and within the canopy which is needed to estimate the soil and canopy resistances to heat transfere R_s and R_x (Eqs. 13–14) , respectively. These wind speed estimates use an exponential decaying function requiring the calculation of extinction coefficients a_s *and* a_x,. These coefficients can be estimated using Eq. (11) (Kustas and Norman 2000).

$$a_s = 0.28 (\Omega(\phi) LAI)^{2/3} h_c^{1/3} w_c^{-1/3} \tag{11a}$$

$$a_x = 0.28 (\Omega(\phi) LAI_L)^{2/3} h_c^{1/3} w_c^{-1/3} \tag{11b}$$

where h_c is the canopy height estimated following Anderson et al. (2004), w_c the mean canopy leaf width, and LAI_L the local leaf area index equals to LAI/f_{veg}.

The sensible heat flux, H, is estimated as $H = H_c + H_s$, where H_c and H_s are the canopy and soil components of H, respectively, estimated using Eqs. (12)–(15) as

$$H = \rho C_p \frac{T_{ac} - T_a}{R_a} \tag{12}$$

$$H_c = \rho C_p \frac{T_c - T_{ac}}{R_x} \tag{13}$$

$$H_s = \rho C_p \frac{T_s - T_a}{R_s} \tag{14}$$

where R_a is the aerodynamic resistance to heat transfer estimated using Eq. (16), ρ the air density taken as 1.24 (kg m^{-3}), C_p the specific heat of air taken as 1005 (J kg^{-1} K^{-1}), and T_{ac} the air-canopy interface temperature.

$$R_a = \frac{\left[\ln\left(\frac{z_u - d_o}{z_{om}}\right) - \psi_M\right]\left[\ln\left(\frac{z_t - d_o}{z_{om}}\right) - \psi_H\right]}{k^2 u} \tag{16}$$

where z_u and z_t are the measurement heights for wind speed and air temperature, respectively, d_o the displacement height estimated as a fraction of canopy height (h_c) as d_o = (2/3) h_c , z_{om} the roughness length for momentum taken as a fraction of h_c as z_{om} = (1/8) h_c (Garratt and Hicks 1973), ψ_H and ψ_M the stability correction factor for atmospheric heat and momentum transfer, respectively (Brutsaert 1982), R_x the total boundary layer resistance of the complete canopy leaves estimated using the formulation described by Norman et al. (1995), and R_s the resistance to heat flow in the boundary layer immediately above the soil surface estimated using Eq. 17 (Norman et al. 1995).

$$R_s = \frac{1}{a + bu_s} \tag{17}$$

where a and b are constants equals to 0.004 and 0.012, respectively, and u_s the wind speed at height above the soil surface where the effect of soil surface roughness is minimal estimated using the formulation described by Norman et al. (1995). One of the recent modifications to Eq. (17) includes the update of R_s through the knowledge of T_s and T_c in which a=0.004 replaced by c $(T_s\text{-}T_c)^{(1/3)}$, where c = 0.0025 (Kustas and Norman 1999, 2000; Li et al. 2005).

The latent heat flux, *LE*, is estimated as $LE = LE_c + LE_s$, where LE_c and LE_s are the canopy and soil components of *LE*, respectively. The model started with an initial estimate of LE_c following Priestly-Taylor formulation (Norman et al. 1995) as $LE_c = \alpha_{PT} f_G [\Delta/(\Delta+\gamma)] Rn_c$, where α_{PT} is the Priestly-Taylor constant taken as 1.26, f_G the fraction of *LAI* that is green (f_G =1), Δ the slope of the saturation vapor pressure versus temperature curve, and γ the psychrometric constant. For stressed vegetation condition an iterative process typically results where the Priestly-Taylor (PT) constant = 1.26 produces a non-physical solution (such as LE_s <0, condensation on soil surface during daytime convective conditions) which then forces the PT to be reduced until a physical solution is obtained (see Kustas et al. 2004).

The soil heat flux, *G*, is estimated as $G = C_g Rn_s$, where C_g taken as 0.35 as suggested by Li et al. (2005) using the formulation described by Kustas et al. (1998).

2.2.2 Modified WB model of the FAO-56

2.2.2.1 Estimation of *ET* using the WB model

The traditional FAO-56 (Allen et al. 1998) approach to estimate *ET* using the dual crop coefficient method described in Eq. (18) represents conditions when crops are under soil water stress.

$$ET_c = (K_s K_{cb} + K_e) ET_o \tag{18}$$

where ET_c is the crop *ET*, K_s the soil water stress coefficient with K_s = 1.0 for no soil water tress and K_s< 1.0 with water stress conditions exist, K_e the soil evaporation coefficient, and ET_o the reference crop *ET* based on a grass reference crop. To estimate K_s

and K_e, water balance calculations for the root zone and the top soil are required on a daily bases with more details found in Allen et al. (1998).

The water balance, WB, of the root zone is

$$SMD_i = SMD_{i-1} - (P_i - RO_i) - I_i - CR_i + ET_{ci} + DP_i \quad (19)$$

where SMD_i is the soil moisture deficit at the end of day i, P the precipitation, RO the losses due to water runoff, I the irrigation water, CR the capillary rise, ET_c the crop ET, and DP losses due to deep percolation. The study area is a rainfed agricultural system characterized by deep groundwater table, therefore, I and CR as well as DP and RO can be neglected.

2.2.2.2 Reflectance-based basal crop coefficient Kcbrf

In the traditional FAO-56 approach tabulated K_{cb} values are used to estimate ET (Allen et al. 1998). Over the last two decades considerable efforts have been made to improve ET and crop water requirement estimates by using remote sensing techniques as in Bausch and Neale (1987), Neale et al. (1989, 2005), and Bausch (1993). They proposed a linear relationship between K_{cb} and the soil adjusted vegetation index ($SAVI$) for corn yielding what's known as the reflectance-based basal crop coefficient (K_{cbrf}). The K_{cbrf} for corn and soybean estimated using Eqs. (20a–b) resulted from Bausch (1993) and an adaptation of the Bean K_{cbrf} developed by (Jayanthi et al. 2001), respectively.

$$K_{cbrf\_corn} = 1.835 \times SAVI - 0.034 \quad (20a)$$

$$K_{cbrf\_soybean} = 1.638 \times SAVI - 0.003 \quad (20b)$$

The use of K_{cbrf} provides improved estimates of actual ET_c at times when remotely sensed images are available. Also the use of linearly interpolated K_{cb} values in

between those K_{cbrf} values instead of the tabulated ones can result in improved estimates of *ET* between satellite overpass dates. Interpolation of K_{cb} from the K_{cbrf} is more effective especially at a shorter time periods in between satellite image acquisition, as is the case for the current study, compared to the crop growing stages periods suggested by Allen et al. (1998).

2.2.3 Soil moisture dynamics model

Because the SM measurements in the study were available for multiple depths but only for the top 30 cm while the WB model provides SM estimates for the entire root zone, further analysis was carried out to provide SM estimates at multiple layers so it could be compared to the measurements. Therefore, a soil moisture dynamics model is implemented to provide such estimates. The model used in this study is a simple one-dimensional modeling scheme similar to the modeling approach described in the simple biosphere SiB model by Sellers et al. (1986) and applied as in Luo et al. (2003) (Eq. (21)).

$$D_1 \frac{d\theta_1}{dt} = I - E - S_1 - Q_{1,2} \tag{21a}$$

$$D_i \frac{d\theta_i}{dt} = Q_{i-1,i} - S_i - Q_{i,i+1} \tag{21b}$$

$$D_n \frac{d\theta_n}{dt} = Q_{i-1,n} - S_n - Q_n \tag{21c}$$

where θ is the soil moisture content, t the time increment, i number increment from 1 to n the total number of soil layers, D layer thickness, I infiltration rate, E evaporation rate from the soil surface and the upper most layer, S_i water uptake from a layer i the root zone, $Q_{i,i+1}$ leakage or soil water flux from layer i to $i+1$, and Q_n the drainage from the

bottom most layer. The root zone up to the maximum root extent of the crops is divided into 7 layers for both corn and soybean fields with the top six layers depths of 0–10, 10–20, 20–30, 30–45, 45–60, and 60–80 cm and the bottom most layer depths of 80–120 and 80–100 cm for corn and soybean fields, respectively.

The estimated *ET* components, the soil evaporation *E* and plant transpiration *T*, obtained from the WB model are used as inputs to the soil moisture dynamics model assuming unstressed water condition as initial boundary condition. The soil moisture content at the root zone for each soil layer is then recalculated by introducing the soil water potential ψ with the corresponding Feddes reduction function $\alpha(\psi)$ (Feddes et al. 1976, 1978) to account for soil moisture stress conditions and to update root water uptake by plants roots. Following an iterative procedure at each time step, the soil moisture content is updated until reaching an acceptable minimum error for the entire analysis period of the year 2002. Detailed description of how to estimate the different components of soil moisture dynamics models is shown in appendix A with the corresponding soil water characteristics shown in Table B1 (Appendix B).

2.2.4 Data assimilation

The application of statistical interpolation SI method in data assimilation (DA) started in the 1940s to improve spatial estimates or forecast of different state variables such as temperature and water vapor using a network of point measurements through minimizing error variances (Daley 1991). For instance if it is required to improve model estimates at location r_0 based on measurement points at locations r_k the SI algorithm can be described by Eq. (22) as

$$ET_{WB}^{A}(r_0) = ET_{WB}^{B}(r_0) + \sum_{k=1}^{K} W_k \left(ET_{TSM}(r_k) - ET_{WB}^{B}(r_k) \right) \quad (22)$$

where superscripts *A* and *B* refer to after and before assimilation, respectively, ρ the model error correlation, ET_{WB} the estimated *ET* based on WB model, ET_{TSM} the estimated *ET* based on the TSM, ε^2 the normalized observation error equals $\sigma_O^2(r_k)/\sigma_B^2$, σ_O^2 and σ_B^2 the variances in ET_{TSM} and ET_{WB} estimates with respect to measured ET_{BR}, respectively, and *W* the weight or Kalman gain of the error for each of the observation points. The least square estimates for *W* can be described as $\sum_{l=1}^{K} W_l \left[\rho_{kl} + \varepsilon_k^2 \right] = \rho_{k0}$, $1 \le k \le K$ with the goal of minimize the after assimilation error variance and it yields the normalized error variance as $\varepsilon_A^2 = \sigma_A^2 / \sigma_B^2 = 1 - \sum_{k=1}^{K} \rho_{k0} W_k$, where ε_A^2 and σ_A^2 are the error and the error variance after assimilation.

In the current study each model point is updated from a single observation point hence a single constant *W* applied for each analysis point. Also the observation points and the model points coincide hence $r_0 = r_k$ and $\rho_{l0} = 1$. Consequently Eq. (22) is then simplified to Eq. (23) with a minimized model variance equal to ε^2 and $W = \varepsilon^2 / (1 + \varepsilon^2) = \sigma_B^2 / (\sigma_B^2 + \sigma_A^2)$.

$$ET_{WB}^{A} = ET_{WB}^{B} + W\left(ET_{TSM} - ET_{WB}^{B} \right) \quad (23)$$

Furthermore analysis of the error variances showed that the resulted values of *W* for all observation points are approximately equal compared to each other; hence, a constant value of *W* is used for all observation points. This is similar to the approach that was followed by Schuurmans et al. (2003) except that they used arbitrary values for *W*.

In this study the SI method is applied using two different options for the value of *W*. First, assuming the weights as time invariant hence a constant value for *W* is used for

all images dates throughout the analysis and hereafter referred to as SIC method, and secondly assuming the weights as time variant hence a different value for W used on each of the images dates and hereafter referred to as SIV method. Consequently, assimilation of ET_{TSM} into WB resulted in ET_{SIC} and SM_{SIC} following the SIC method and ET_{SIV} and SM_{SIV} following the SIV method.

2.2.5 Update of Ks and SMD

On the assimilation dates (i.e. the dates of the images used for assimilation), the estimated ET_c value is used to update the WB calculation of the root zone by back calculating new values for K_s and SMD. Due to assimilation, the resulting new value for ET_c is followed by updating only the values of K_s and K_e to satisfy Eq. (18) since ET_o remains unchanged and K_{cb} is replaced by the remotely sensed value K_{cbrf}. Estimation of K_e is based on moisture conditions of the top 10 cm of the soil hence it is expected to have less variation than the value of K_e, specially on days with no rainfall, and therefore assumed to remain unchanged after assimilation. While estimation of K_s requires knowing the soil moisture content for the root zone, the water balance condition of the root zone is then updated by back calculating a new value for K_s and consequently updating the value of SMD as well. The updated value of SMD is then transferred to the next time step which then leads to an updated soil moisture status after assimilation for subsequent days depending on the water stress conditions at the specific field.

2.3 Data

2.3.1 Study area

The methodology is applied at the same study area of the Soil Moisture-Atmosphere Coupling Experiment (SMACEX) conducted during the summer of 2002 in south central Ames, Iowa. The area covers about 10 km north–south by 30 km east–west centered at 41.96 °N 93.6 °W and it includes the Walnut Creek watershed as shown in Fig. 2.1. The region is rainfed agriculture with 95% of the area covered by corn and soybean crops and a growing season lasting about 5 months starting late April/early May until late September/ early October. The climatic region is considered humid with an average annual precipitation of 835 mm. Most of data used were acquired from SMACEX with detailed descriptions found in Kustas et al. (2005).

2.3.2 Remote sensing data

The remote sensing data used consists of Landsat Thematic Mapper (TM5) and (TM7) images acquired on day of year (DOY) 174, 182, 189 and 198 in addition to an airborne multispectral image acquired on DOY 167 by the research aircraft from the Remote Sensing Services Lab (RSSL) at Utah State University. All the images are atmospherically corrected by Li et al. (2004) using MODTRAN (Berk et al. 1989) to obtain at-surface reflectance and radiometric surface temperature. Only the four bands red (RED), near infrared (NIR), mid infrared1 (MIDIR1), and the thermal infrared band are used in the analysis in addition to the land use image produced during SMACEX to identify the crop types and locations during the study period.

2.3.3 Meteorological and energy flux data

Daily hydrometeorological observations from the meteorological and rain gauge network acquired for the entire year of 2002 included air temperature, wind speed, height of measurements, vapor pressure, relative humidity, rainfall measurements, and instantaneous and daily ET_o for grass reference crop. Rainfall measurements were also obtained from the Iowa Environmental Network for a station named Colo Elem for the purpose of representing the spatial and temporal variability of the rainfall on the east side the study area near Fields 23 and–24 (Fig. 2.2).

Initial analysis of spatial and temporal variability of daily rainfall measurements made with the rain gauge network within the Walnut Creek watershed for the year of 2002 showed that the watershed can be divided into three regions east, west, and central. The east and west regions received above average to maximum amounts of rainfall, while the central region received below average amounts of rainfall. An additional source of rainfall measurements occurred during the short period of soil moisture measurements and surface energy fluxes which allowed for a comparison of what was measured at the soil moisture monitoring fields with precipitation measured at the rain gauge network. Based on this comparison, an average value from measurements of the rain gauges 705–707 were deemed representative and used in the soil moisture analysis for Fields 15–16 (Fig. 2.2). Fields 23–24 were located outside the Walnut Creek watershed and during the short period of rainfall measurements made within these two fields, the amounts were considerably different than those registered by rain gauges 722–723 which were the closest to these two fields but still within the watershed. Rainfall depths from another station named Colo Elem (Fig. 2.2) located about 4 km to the east of Fields

23–24 were much closer to those measured outside and therefore were used for the soil moisture analysis in these two fields. The spatial variability of the rainfall can explain, to some extent, the results obtained in Field 24 that showed a relatively lower improvement in estimates of SM_{SIC} compared to SM_{WB} with an IA of 0.67 to 0.72, respectively. Rain gauges 705–707 were located within a few dozen meters from Fields 15–16 hence provided realistic inputs to the soil moisture profile modeling. Kriging techniques were not used due to the sparse network of stations.

Ground-based instantaneous observations of surface energy fluxes and other meteorological observations were obtained from the meteorological-flux (METFLUX) towers network which consisted of 12 eddy covariance (EC) systems operated for about 2 month period during SMACEX. The surface energy flux measurements included *Rn*, *H*, *LE*, and *G* while the meteorological observations included incoming solar radiation, air temperature, vapor and atmospheric pressure, wind speed and direction, standard deviation of wind direction, and friction velocity. Data from 10 EC systems were used and distributed evenly between corn fields identified as Fields 6, 24, 33, 15.1, and 15.2 and soybean fields identified as Fields 3, 13, 23, 16.1, and 16.2 (Fig. 2.2).

2.3.4 Soil data

Volumetric soil moisture profile measurements were available at 2, 5, 10, 15, 20, and 30 cm depths at four fields identified as Fields 15, 16, 23, and 24. Hourly measurements were reported for DOY 174–191 for Fields 15–16, and for DOY 175–204 for Fields 23–24. For each field, the soil moisture was measured at two different sites from which a weighted average soil moisture profile was calculated to represent the measurements for each field.

A soils map that identified the different soil types, texture type, and characteristics was also used to provide the required information for the water balance calculations. The map also provides the available water holding capacity and the percentage weights for sand, clay, and organic matter contents which are used to calculate the required soil water characteristics such as the soil moisture at field capacity and the permanent wilting point is shown in Table B1 (Appendix B).

2.4 Model verification

The estimated spatial surface energy fluxes from the TSM were compared with ground-based measured fluxes using upwind Source Area (SA) or flux footprint method. The flux footprints for each of the images dates were identified using the Flux Source Area Model (FSAM) developed by Schmid (1995) and georeferenced to the specified EC tower location. Comparison of *ET* estimates to measurements was performed by integrating the estimated spatial fluxes using the resulting footprint weights. FSAM provides weights of the contribution of the upwind SA from which flux measurements are integrated and it represents approximately 90 % of the total SA that contributes to the measured fluxes.

EC system measurements of surface energy fluxes typically result in lack of closure (Massman and Lee 2002), which means that the measured fluxes do not close the energy balance equation as they should. The SMACEX flux data typically resulted in a difference of ≈ 100 W m^{-2} between $Rn - G$ and $LE+H$ as shown in Prueger et al. (2005). This problem can be solved using one of the closure methods suggested in the literature such as the residual or the Bowen ratio *H/LE* methods (Twine et al. 2000; Li et al. 2005). The two methods are used in order to show that the selection of closure method could

affect the quality of the results. The residual method relies in placing all the closure error of the energy balance into *LE* yielding the adjusted latent heat flux (LE_{Re}). The Bowen ratio relies on proportionally distributing the error between *LE* and *H* based on the Bowen ratio *H/LE* yielding the adjusted latent and sensible heat fluxes LE_{BR} and H_{BR}, respectively.

The estimated and measured instantaneous LE_{TSM} and LE_{BR} (W m^{-2}) are extrapolated to equivalent daily ET_{TSM} and ET_{BR} (mm day^{-1}), respectively, and compared with each other. The reference *ET* fraction (ET_{rF}) method described and used by Romero (2004), Allen et al. (2007), and Chavez et al. (2008) is used for the extrapolation of the instantaneous *ET*. ET_{rF} is the ratio between instantaneous values of ET_{TSM} or ET_{BR} and ground-based measured ET_o and is assumed to be constant throughout the day. The corresponding ET_{rF} is multiplied by the daily ET_o to extrapolate to daily ET_{TSM} and ET_{BR}.

Estimates of SM_{WB} and ET_{WB} resulting from the WB model before assimilation were compared with ground-based measurements of *SM* and ET_{BR}, respectively. Soil moisture (SM) profile measurements were available at only four fields; Fields 15, 16, 23, and 24, while the extrapolated ET_{BR} were available at all of the 10 EC locations. After assimilation, the resulting ET_{SIC} and SM_{SIC}, using the SIC method, and ET_{SIV} and SM_{SIV}, using the SIV method, were also compared to the measured *SM* and ET_{BR}, respectively. The soil moisture estimates at the three top layer 0–10, 10–20, and 20–30 cm layers in addition the entire top 30 cm layer were compared with the corresponding measurements at Fields 15, 16, and 24.

The model performance statistics are presented using the root mean square error (RMSE), the mean absolute error (MAE), the mean error (ME), and the modified index

of agreement (IA) (Legates and McCabe 1999) which ranges between 0.0–1.0 with higher values for better model performance (Eqs. 24–27).

. $$\mathrm{RMSE} = \frac{1}{n}\sqrt{\sum_{i=1}^{n}(P_i - O_i)^2} \quad (24)$$

$$\mathrm{MAE} = \frac{1}{n}\sum_{i=1}^{n}|P_i - O_i| \quad (25)$$

$$\mathrm{ME} = \frac{1}{n}\sum_{i=1}^{n}(P_i - O_i) \quad (26)$$

$$\mathrm{IA} = 1 - \frac{\sum_{i=1}^{n}|P_i - O_i|}{\sum_{i=1}^{n}|P_i - \overline{O}| + \sum_{i=1}^{n}|O_i - \overline{O}|} \quad (27)$$

where P_i and O_i are the estimated and measured values, respectively, n the total number of data record, and $\overline{O}$ the mean value of observations.

2.5 Results and discussion

Scatter plots of the estimated surface energy fluxes using the TSM compared to measurements are shown in Fig. 2.3 and the corresponding model performance statistics summarized in Table 2.1. The estimated *Rn* resulted in the lowest RMSE of 18 W m^{-2}, which is ≈ 3% of the measurement mean, and a MAE of 14 W m^{-2}, while both LE_{Re} and LE_{BR} resulted in the highest RMSE of 47 and 43 W m^{-2}, respectively, which represent ≈ 11% of the corresponding measurement mean, and both reported MAE of 35 and 34 W m^{-2}, respectively. The RMSE for *G* is about 28 Wm^{-2} which represents ≈ 28% of the measurements mean while the RMSE for *H* and H_{BR} were 30 and 35 Wm^{-2} which represent ≈ 34 % of the measurements mean equally for both. The MAE of *G*, *H*, and H_{BR} are 22, 24 and 28 W m^{-2}, respectively. Considering the percentages of the RMSE to the corresponding measurement means the results indicate that the TSM performed

adequately, within the typical measurement errors of eddy covariance systems. Moreover, the results also indicate that, except for *G*, the TSM slightly underestimates all of the fluxes as shown in the reported ME values. The effect of using different closure methods on the model performance is inconclusive, as the reported statistics indicate differences of 3 to 5 W m^{-2} which are small considering the lack of closure of up to 100 W m^{-2} in the EC measurements. Overall, the RMSE statistics for all fluxes were similar to those presented by Li et al. (2005) which resulted from the comparisons using fluxes estimated from 4 Landsat images. Extrapolated daily estimates of ET_{TSM} from LE_{TSM} were also compared with measurements of ET_{Re} and ET_{BR} with the statistics summarized in Table 2.2, indicating similar results.

Scatter plots of the estimated ET_{TSM} using the TSM and the estimated ET_{WB} using the WB model are both compared to the measured ET_{BR} as shown in Figs. 2.4a–b, respectively, with corresponding performance statistics shown in Table 2.2. The results show that ET_{TSM} has a lower RMSE of 0.67 mm day^{-1} and MAE of 0.54 mm day^{-1} compared the RMSE of 1.26 mm day^{-1} and MAE of 1.00 mm day^{-1} for ET_{WB}, respectively, while both ET_{TSM} and ET_{WB} resulted in a slight overestimation when compared to measurements as indicated by their corresponding ME values. These results indicate that the ET_{TSM} provided a better quality estimates than $ET_{WB,}$ despite the fact that remote sensing is partly used in the WB model through introducing K_{cbrf} that is based on image reflectance instead of the tabulated K_{cb}. This significantly greater difference with ET_{BR} estimates using the WB model is related to several of the model assumptions/approximations, it uses average agronomic and climatic conditions which is not expected to adequately describe actual crop growth conditions for a specific area.

However, the use of remote sensing techniques can provide site specific actual conditions and hence result in improved estimates for both K_{cbrf} (instead of the tabulated K_{cb} values) and correspondingly actual *ET* estimates. This capability can potentially lead to an improvement in monitoring and predicting actual crop growth conditions including soil moisture stress.

Based on the resulting error variances of the estimated ET_{TSM} and ET_{WB}, the calculated weight or Kalman gain *W* used in the SIC method is about 0.78, while the calculated weights that are used in the SIV method are about 0.45, 0.28, 0.31,0.81 and 0.81 for each of the images dates DOY 167, 174, 182, 189 and 198, respectively. Scatter plots of the estimated ET_{SIV} and ET_{SIC} due to the assimilation compared to ET_{BR} are shown in Figs. 2.4c–d and the related model performance statistics are listed in Table 2.2. From Table 2.2, the estimated ET_{SIC} resulted in the lowest RMSE of value 0.67 mm day^{-1} compared to 1.26 and 1.01 mm day^{-1} for ET_{WB} and ET_{SIV}, respectively. Also ET_{SIC} resulted in the lowest MAE of 0.62 mm day^{-1} compared to 1.00 and 0.80 mm day^{-1} for ET_{SIV} and ET_{WB}, respectively. The ME values in Table 2.2 indicate ET_{WB} slightly overestimated ET_{BR} while both ET_{SIC} and ET_{SIV} underestimated by ~0.3 mm/day. Moreover, the highest IA value of 0.80 is reported for ET_{SIC} compared to 0.68 and 0.75 for ET_{WB} and ET_{SIC}, respectively. Overall, ET_{SIC} yielded the best performance when compared to the estimated ET_{WB} and ET_{SIV} and is comparable to ET_{TSM}. More specifically, the use of the DA following either the SIC or SIV methods, has clearly resulted in improved estimates of *ET* from the water balance model as the reported difference statistics rank the estimated ET_{WB} with no data assimilation as yielding the lowest performance.

The effect of data assimilation on the estimated values of *ET* is shown in time series plots of ET_{WB}, ET_{SIC} and ET_{SIV} for each of the analysis fields (Fig. 2.5). It shows that, on the dates with remote sensing imagery, estimated ET_{WB} before assimilation showed higher values compared to estimated ET_{SIC} and ET_{SIV}. Consequently, and as a result of updating the soil moisture on these dates, the status of the soil moisture for several days following the remotely sensed observation is also updated and hence affects estimates of *ET* on those days as well. Depending on the value of the assimilated ET_{TSM} , water stress conditions, and the crop growth the impact of updating the soil moisture can be significant for an extended period, namely up to two weeks beyond the date of the last image as indicated in the results for Field 16 soybean (Fig. 2.5b) and Field 24 corn (Fig. 2.5d).

Time series plots of estimates of SM_{WB}, before assimilation together with measured *SM* for each of the soil layers including the entire top 30 cm are shown in Figs. 2.6a–b for Fields 15 and 16, respectively, with the corresponding scatterplots shown in Figs. 2.7a–b. With application of DA, output of soil moisture time series from SM_{SIC} versus measured *SM* is illustrated for each of the soil layers including the entire top 30 cm are shown in Figs. 2.8a–b for Fields 15 and 16, respectively, with the corresponding scatterplots shown in Figs. 2.9a–b. The corresponding performance statistics for these fields including Field 24 are shown in Tables 2.3 and 2.4. Note that *SM* measurements for Field 23 were not included because they were determined to be unreliable based on the field data sheet. The time series plots show that both SM_{WB} and SM_{SIC} dynamically follow the measured *SM* , but with SM_{WB} generally underestimating measurements and SM_{SIC} showing relatively better performance (unbiased) over the entire top 30 cm layer. This is

supported in Tables 2.3 and 2.4 where the statistics for SM_{SIC} are consistently better for layers below 10 cm and for the top 30 cm. Both assimilation methods (SIV and SIC) produce an improvement in the difference statistics when compared to the WB method, but overall the SIC method yields closer results with measured *SM*. This suggests that the assimilation of ET_{TSM} from the TSM into the WB model led to an improvement in soil moisture estimates. Because of improvements in *ET* and SM estimation using either assimilation it can be inferred that there will be an improvement in the soil moisture estimates for the entire root zone.

2.6 Summary and conclusions

This study presented the Hybrid Evapotranspiration (HET) approach for improved spatio-temporal estimates of evapotranspiration (*ET*) and soil moisture (SM). The HET approach was applied on the Walnut Creek watershed, Iowa. The remote sensing-based two source model (TSM) of the surface energy balance was used to estimate actual *ET* for 5 satellite and airborne image acquisition dates. Also the water balance (WB) model of the traditional FAO-56 approach was modified to incorporate reflectance based basal crop coefficient (K_{cbrf}) in the place of basal crop coefficient (K_{cb}) and used to estimate actual daily *ET*. Both estimates of *ET* were then compared to daily *ET* from ground-based latent heat flux measurements from EC systems. The results showed that the TSM provided improved estimates of *ET* when compared to the WB model. The statistical interpolation method for data assimilation was used to assimilate the estimated *ET* from the TSM into the WB model. This assimilation resulted in updating the soil moisture status and provided improved estimates of *ET* and SM for several days following the assimilation dates which, overall, is an indication of improved WB model performance.

Generally, combining the remote sensing techniques with the WB model of the traditional FAO-56 approach led to a better representation of some key factors that can affect *ET* such as the available energy at surface, local variability of surface conditions (e.g. surface temperature), and agronomical conditions (e.g. plant biomass, and cover). It also resulted in better prediction capabilities in the spatial and temporal variability in evapotranspiration and soil moisture within this agricultural study area. This approach of combining remotely sensed *ET* using a reliable two-source scheme with a relatively simple water balance model using data assimilation is a promising methodology for assessing actual crop agronomical and growing conditions, improved root zone soil moisture and *ET* estimation which could lead to more accurate yield estimation in agricultural areas The improved estimates of *ET* and soil moisture will also be useful for updating regional hydrological and atmospheric models (Crow et al. 2008).

References

Allen, R. G., L. S. Pereira, D. Raes, and M. Smith, 1998: *Crop evapotranspiration: Guidelines for computing crop water requirements.* Paper No. 56. Food and Agricultural Organization of the UN, 328 pp.

Allen, R. G., M. Tasumi, A. Morse, and R. Trezza, 2005: A Landsat-based energy balance and evapotranspiration model in Western US water rights regulation and planning. *Irri. Drain. Syst.*, **19,** 251–268.

Allen, R. G., M. Tasumi, and R. Trezza, 2007: Satellite-based energy balance for mapping evapotranspiration with internalized calibration (METRIC)-Model. *J. Irrig. Drain. Eng.*, **133(4),** 380–394.

Anderson, M. C., C. M. U. Neale, F. Li, J. M. Norman, W. P. Kustas, H. Jayanthi, and J. Chavez, 2004: Upscaling ground observations of vegetation water content, canopy height, and leaf area index during SMEX02 using aircraft and Landsat imagery. *Remote Sens. Environ.*, **92,** 447–464.

Anderson, M. C., J. M. Norman, G. R. Diak, W. P. Kustas, and J. R. Mecikalski, 1997: A two-source time integrated model for estimating surface fluxes using thermal infrared remote sensing. *Remote Sens. Environ.*, **60,** 195–216.

Anderson, M. C., J. M. Norman, J. R. Mecikalski, J. A. Otkin, and W. P. Kustas, 2007: A climatological study of evapotranspiration and moisture stress across the continental United States based on thermal remote sensing: 1. Model formulation. *J. Geophys. Res.*, **112,** doi: 10.1029/2006JD007506.

Bastiaanssen W. G. M., J. Hugen, J. K. Schakel, and B. J. van den Broek, 1996: Modeling the soil-water-crop-atmosphere system to improve agricultural water management in arid zone (SWATRE). In: Van Den Broek, B.J. (Ed.), *Dutch Experiences in Irrigation Water Management Modeling*, Report 123, DLO Winand Staring Centre, Wageningen, the Netherlands, 13-30.

Bastiaanssen, W., M. Menenti, R. Feddes, and A. Holtslag, 1998: A remote sensing surface energy balance algorithm for land (SEBAL) 1. Formulation. *J. Hydrol.*, **212–213,** 198–212. doi:10.1016/S0022-1694(98)00253-4.

Bausch, W. C., 1993: Soil background effects on reflectance-based crop coefficients for corn. *Remote Sens. Environ.,* **46,** 213–222.

Bausch, W. C., and C. M. U. Neale, 1987: Crop coefficients derived from reflected canopy radiation: A concept. *Trans. Amer. Soc. Agric. Engin.* **30**, 703–709.

Berk, A., L. S. Bernstein, and D. C. Robertson, 1989: MODTRAN: A moderate resolution model for LOWTRAN 7. Geophysics Laboratory, Bedford, Maryland, Rep. GL-TR-89-0122, 37 pp.

Brutsaert, W., 1982: *Evaporation into the Atmosphere: Theory, History, and Applications.* Springer, 299 pp.

Campbell, G. S., and J. M. Norman, 1998: *An introduction to Environmental Biophysics*. 2nd ed. Springer, 286 pp.

Chavez, J. L., C. M. U. Neale, J. H., Prueger, and W. P. Kustas, 2008: Daily evapotranspiration estimates from extrapolating instantaneous airborne remote sensing ET values. *Irrig. Sci.*, **27,** 67–81.

Crow, W. T., W. P. Kustas, and J. H. Prueger, 2008: Monitoring root-zone soil moisture through the assimilation of a thermal remote sensing-based soil moisture proxy into a water balance model, *Remote Sens. Environ.*, **112,** 1268–1281.

Crow, W. T., F. Li, and W. P. Kustas, 2005: Intercomparison of spatially explicit models for predicting surface energy flux patterns during the 2002 SMACEX field experiment. *J. Hydrometeor.*, **6,** 941–953.

Daley, R., 1991: *Atmospheric Data Analysis*. Cambridge University Press, 457 pp.

Doorenbos, J., and W. O. Pruitt, 1977: *Guidelines for predicting crop water requirements*. Paper No. 24. Food and Agricultural Organization of the UN, 144 pp.

Feddes, R. A., P. J. Kowalik, K. Kolinska–Malinka, and H. Zaradny, 1976: Simulation of field water uptake by plants using a soil water dependent root extraction function. *J. Hydrol.*, **31,** 13–26.

Feddes, R. A., P. J. Kowalik, and H. Zaradny, 1978: *Simulation of field water use and crop yield*. Centre for Agricultural Publishing and Documentation, 188 pp.

Garratt, J. R. and B. B. Hicks, 1973: Momentum, heat and water vapor transfer to and from natural and artificial surfaces. *Quart. J. Roy. Meteor. Soc.*, **99,** 680–687.

Hoke, J., and R. A. Anthes, 1976: The initialization of numerical models by a dynamic initialization technique. *Mon. Weather Rev.*, **104,** 1551–1556.

Houser, P. R., W. J. Shuttleworth, J. S. Famiglietti, H. V. Gupta, K. H. Syed, and D. C. Goodrich, 1998: Integration of soil moisture remote sensing and hydrologic modeling using data assimilation. *Water Resour. Res.*, **34,** 3405–3420.

Hunsaker, D. J., G. J. Fitzgerald, A. N. French, T. R. Clarke, M. J. Ottman, and P. J. Pinter Jr., 2007: Wheat irrigation management using multispectral crop coefficients: I. Crop evapotranspiration prediction. *Trans. Amer. Soc. Agric. Biolo. Eng.*, **50(6),** 2017–2033.

Hunsaker, D. J., P. J. Pinter Jr., and B. A. Kimball, 2005: Wheat basal crop coefficients determined by normalized difference vegetation index. *Irrig. Sci.*, **24,** 1–14.

Jayanthi, H., C. M. U. Neale, and J. L. Wright, 2001: Seasonal Evapotranspiration Estimation Using Canopy Reflectance - A Case Study Involving Pink Beans. *Proc. Symp. Remote Sens. Hydrol.*, 267, Santa Fe, NM, Inter. Assoc. Hydrol. Sci., 302–305.

Jayanthi, H., C. M. U. Neale, and J. L. Wright, 2007: Development and validation of canopy reflectance-based crop coefficient for potato. *Agriculturl Water Management*,**88** 235–246.

Kalma, J. D., McVicar, T. R., and McCabe, M. F., 2008: Estimating land surface evaporation: a review of methods using remotely sensing surface temperature data. *Surv.Geophys.*, doi:10.1007/s10712-008-9037-z.

Kustas, W. P., J. L. Hatfield, and J. H. Prueger, 2005: The Soil Moisture–Atmosphere Coupling Experiment (SMACEX): Background, hydrometeorological conditions, and preliminary findings. *J. Hydrometeor.*, **6,** 791–804.

Kustas, W. P., and J. M. Norman, 1999: Evaluation of soil and vegetation heat flux predictions using a simple two-source model with radiometric temperatures for partial canopy cover. *Agric. For. Meteorl.*, **94,** 13–29.

Kustas W. P., and J. M. Norman, 2000: A two-source energy balance approach using directional radiometric temperature observations for sparse canopy covered surface. *Agron. J.*, **92,** 847–854.

Kustas, W. P., J. M. Norman, T. J. Schmugge, and M. C. Anderson, 2004: Mapping surface energy fluxes with radiometric temperature. (Chapter 7) In: D. A. Quattrochi, & J. C. Luvall (Eds.), Thermal Remote Sensing in Land Surface Processes (pp. 205 – 253). Boca Raton, Florida: CRC Press.

Kustas, W. P., X. Zhan, and T. J. Schmugge, 1998: Combining optical and microwave remote sensing for mapping energy fluxes in a semiarid watershed. *Remote Sens. Environ.,* **64,** 116–131.

Legates, D. R., and G. J. McCabe Jr., 1999: Evaluating the use of ‘‘goodness-of-fit’’ measures in hydrologic and hydroclimatic model validation. *Water Resour. Res.* **35 (1)**, 233–241.

Li, F, T. J. Jackson, W. P. Kustas, T. J. Schmugge, A. N. French, M. H. Cosh, and R. Bindlish, 2004: Deriving land surface temperature from Landsat 5 and 7 during SMEX02/SMACEX. *Remote Sens. Environ.*, **92,** 521–534.

Li, F, W. P. Kustas, J.H. Prueger, C. M. U. Neale, and T. J. Jackson, 2005: Utility of remote sensing based two-source energy balance model under low and high vegetation cover conditions. *J. Hydrometeor.*, **6(6),** 878–891.

Li, K.Y., R. De Jong, and J. B. Boisvert, 2001: An exponential root-water-uptake model with water stress compensation. *J. Hydrol.*, **252,** 189–204.

Li, K. Y., R. De Jong, M. T. Coe, and N. Ramankutty, 2006: Root-water-uptake based upon a new water stress reduction and an asymptotic root distribution function. *Earth Interact.*, **10,** 1–22.

Luo, Y., Z. Ouyang, G. Yuan, D. Tang, and X. Xie, 2003: Evaluation of macroscopic root water uptake models using lysimeter data. *Trans. Amer. Soc. Agric. Eng.*, **46(3),** 625–634.

Massman, W. J., and X. Lee, 2002: Eddy covariance flux corrections and uncertainties in long term studies of carbon and energy exchanges. *Agric. For. Meteorl.*, **113,** 121–144.

Meijerink, A. M. J., A. S. M. Gieske, and D. Vekerdy, 2005: Surface energy balance using satellite data for the water balance of a traditional irrigation wetland system in SW Iran. *Irrig. Drain. Syst.*, **19,** 89−105.

Menenti, M., and B. Choudhury, 1993: Parameterization of land surface evaporation by means of location dependent potential evaporation and surface temperature range. *Proc. Conf. on Exchange processes at the Land Surface for a range of Space and Time Scales*, 212, Yokohama, Japan, Inter. Assoc. Hydrol. Sci., 561–568.

Neale, C. M. U., H. Jayanthi, and J. L. Wright, 2005: Irrigation water management using high resolution airborne remote sensing. *Irrig. Drain. Syst.*, **19,** 321–336.

Neale, C. M. U., W. C. Bausch, and D. F. Heermann, 1989: Development of reflectance-based crop coefficients for corn. *Trans. Amer. Soc. Agirc. Eng.*, **32(6),** 1891–1899.

Norman, J. M., W. P. Kustas, and K. S. Humes, 1995: A two-source approach for estimating soil and vegetation energy fluxes in observations of directional radiometric surface temperature. *Agric. For. Meteorl.,* **77,** 263–293.

Prueger, J. H., J. L. Hatfield, T. B. Parkin, W. P. Kustas, L. E. Hipps, C. M. U. Neale, J. I. MacPherson, W. E. Eichinger, and D. I. Cooper, 2005: Tower and aircraft eddy covariance measurements of water, energy, and carbon dioxide fluxes during SMACEX. *J. Hydrometeor.*, **6,** 954–960.

Raes, D., 2002: *BUDGET: A Soil Water and Salt Balance Model Reference Manual Version 5.0*. Catholic University of Leuven, 79 pp.

Romero, M. G., 2004: Daily evapotranspiration estimation by means of evaporative fraction and reference evapotranspiration fraction. Ph.D. dissertation, Utah State University, 190 pp.

Schmid, H. P., 1995: Source area for scalars and scalar fluxes. *Bound.-Layer Meteor.*, **67,** 293–318.

Schuurmans, J. M., P. A. Troch, A. A. Veldhuizen, W. G. M. Bastiaanssen, and M. F. P. Bierkens, 2003: Assimilation of remotely sensed latent heat flux in a distributed hydrological model. *Adv. Water Resour.*, **26,** 151–159.

Sellers, P. J., Y. Mintz, Y. C. Sud, and A. Dalcher, 1986: A simple biosphere model (SIB) for use within general circulation models. *J. Atmos. Sci.*, **43,** 505–531.

Shuttleworth, W. J., 2006: Towards one-step estimation of crop water requirements, *Trans. Ameri. Soc. Agric. Biol. Eng.*, **49**, 925–935.

Stauffer, D. R., and N. L. Seaman, 1990: Use of four-dimensional data assimilation in a limited-area mesoscale model: Part I: Experiments with synoptic-scale data. *Mon. Weather Rev.*, **118,** 1250–1277.

Tasumi, M., R. G. Allen, R. Trezza, and J. L. Wright, 2005: Satellite-based energy balance to assess within-population variance of crop coefficient curves. *J. Irrig. Drian. Engin.,* **131,** 94–109.

Twine, T. E., W. P. Kustas, J. M. Norman, D. R. Cook, P. R. Houser, T. P. Meyers, J. H. Prueger, P. J. Starks, and M. L. Wesely, 2000: Correcting eddy-covariance flux underestimates over grassland. *Agric. Forest Meteor.*, **103,** 279–300.

Van Dam, J. C., J. Huygen, J. G. Wesseling, R. A. Feddes, P. Kabat, P. E. V. van Walsum, P. Groenendijk, and C. A. van Diepen, 1997: Theory of SWAP 2.0: Simulation of water flow, solution transport and plant growth in the Soil-Water-Atmosphere-Plant environment. Wageningen Agricultural University and DLO-Winand Staring Centre. Tech. Doc. 45, 167 pp.

Wagner, D. G., R. M. Hoffer, and T. H. Podmore, 2003: Determination of consumptive water use for river basins by remote sensing and GIS techniques. *Trans. Amer. Soc. Agric. Eng.,* **46(6),** 1515–1523.

Wright, J. L., 1982: New evapotranspiration crop coefficients. *J. Irrig. Drain. Div.*, **108,** 57–74.

TABLE 2.1. Summary of model performance statistics of the TSM estimates compared with measurements for the sensible heat flux (*H*), the latent heat flux (*LE*), the soil heat flux (*G*), and the net radiation (*Rn*). Subscripts Re and BR refer to when the obtained estimates fluxes using TSM are compared to measured fluxes adjusted to residual and to Bowen ratio closure methods, respectively. The values in packets are the related mean of the measurements.

		RMSE ($W\ m^{-2}$)	MAE ($W\ m^{-2}$)	ME ($W\ m^{-2}$)
All	H (89)	30	24	-7
	H_{BR} (103)	35	28	-17
	LE_{Re} (414)	47	35	-21
	LE_{BR} (394)	43	34	-2
	G (100)	28	22	19
	R_n (583)	18	14	-8
	Re (298)	32	23	-5
	BR (316)	31	23	-1

TABLE 2.2. Summary of model performance statistics of the TSM and WB estimates of *ET* compared with measurements. Subscripts Re and BR refer to TSM estimates are compared with measured fluxes adjusted to residual and to Bowen ratio closure methods, respectively. ET_{WB} estimates of ET_{WB} using WB and ET_{SIC}, ET_{SIV} estimates of *ET* using assimilation methods.

		RMSE (mm/day)	MAE (mm/day)	ME (mm/day)	IA
ET_{TSM}	Re	0.72	0.54	-0.33	0.84
	BR	0.67	0.54	0.02	0.85
ET_{WB}		1.26	1.00	0.05	0.68
ET_{SIV}		1.01	0.80	-0.31	0.75
ET_{SIC}		0.67	0.62	-0.30	0.81

TABLE 2.3. Summary of models performance statistics comparing estimated $SM_{WB,}$ SM_{SIC}, SM_{SIV}, using the WB model, SIC, and SIV methods, respectively, with measured SM for 0–10, 10–20, 20–30 and the top 30 cm soil layers using for Field 15 corn and Field 16 soybean.

Statistics	Soil Layers	Field 15 corn			Field 16 soybean		
	(cm)	SM_{WB}	SM_{SIV}	SM_{SIC}	SM_{WB}	SM_{SIV}	SM_{SIC}
RMSE (mm)	0–10	8.10	8.34	8.25	8.10	8.35	8.34
	10–20	5.13	4.83	4.55	5.13	4.49	4.14
	20–30	7.10	5.40	4.95	9.46	7.34	6.68
	top 30	5.99	5.08	4.63	6.30	3.86	3.62
IA	0–10	0.40	0.39	0.40	0.36	0.36	0.36
	10–20	0.51	0.53	0.54	0.55	0.60	0.63
	20–30	0.38	0.49	0.56	0.34	0.43	0.46
	top 30	0.76	0.80	0.83	0.76	0.86	0.87
MAE (mm)	0–10	6.74	7.04	6.94	6.23	6.44	6.43
	10–20	5.01	4.70	4.40	4.89	4.23	3.88
	20–30	6.24	4.24	3.45	7.38	5.18	4.54
	top 30	5.44	4.17	3.46	5.80	3.14	2.82
ME (mm)	0–10	6.38	6.70	6.62	6.15	6.38	6.40
	10–20	-3.66	-3.33	-3.04	-3.83	-2.93	-2.06
	20–30	-6.23	-4.24	-3.45	-7.32	-5.00	-4.06
	top 30	-3.52	-0.88	0.13	-5.01	-1.54	0.29

TABLE 2.4. Summary of models performance statistics comparing estimated $SM_{WB,}$ SM_{SIC}, SM_{SIV}, using the WB model, SIC, and SIV methods, respectively, with measured SM for 0–10, 10–20, 20–30 and the top 30 cm soil layers using for Field 23 soybean and Field 24 corn.

Statistics	Soil Layers	Field 24 corn		
	(cm)	SM_{WB}	SM_{SIV}	SM_{SIC}
RMSE (mm)	0–10	3.72	3.84	3.84
	10–20	4.07	4.18	4.08
	20–30	4.61	4.12	4.25
	top 30	5.55	5.31	5.25
IA	0–10	0.65	0.63	0.63
	10–20	0.42	0.42	0.44
	20–30	0.33	0.35	0.32
	top 30	0.67	0.71	0.72
MAE (mm)	0–10	2.44	2.55	2.55
	10–20	3.61	3.60	3.41
	20–30	4.00	3.45	3.69
	top 30	4.79	4.14	3.94
ME (mm)	0–10	1.32	1.52	1.51
	10–20	-0.25	0.07	0.26
	20–30	-3.39	-2.28	-1.99
	top 30	-2.32	-0.68	-0.22

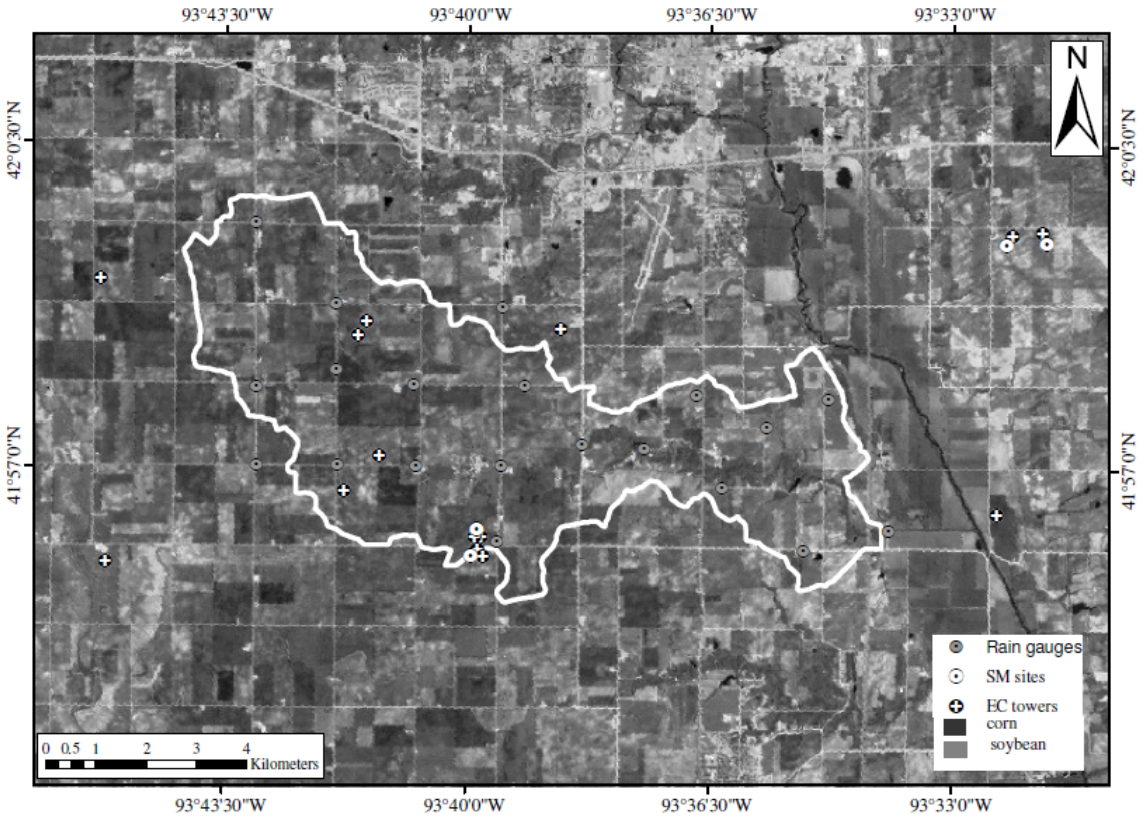

Fig. 2.1. Satellite image in gray color scale for the NIR, RED, and MIDIR1 bands on June 23rd ,2002 (DOY 174) showing the location of the study area including the Walnut Creek watershed boundary (white line), eddy covariance EC towers (circle with plus), soil moisture sites (circle with dot), and the crop types soybean (light gray) and corn (dark gray) .

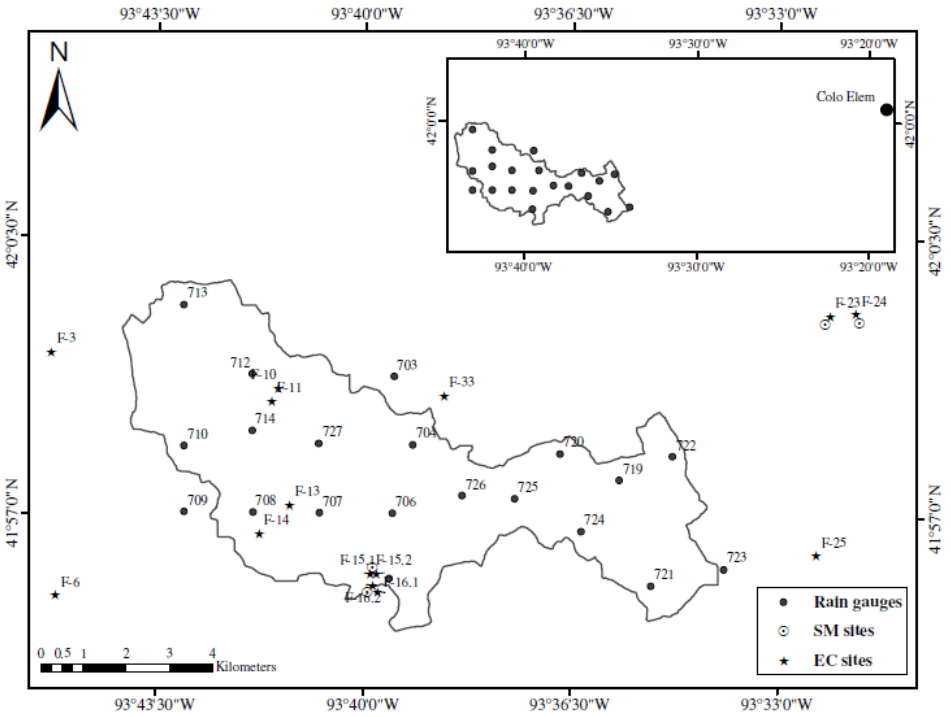

Fig. 2.2. Location of the available rain gauges (solid circles), the soil moisture measurements (circles with dots) and the eddy covariance systems (stars).

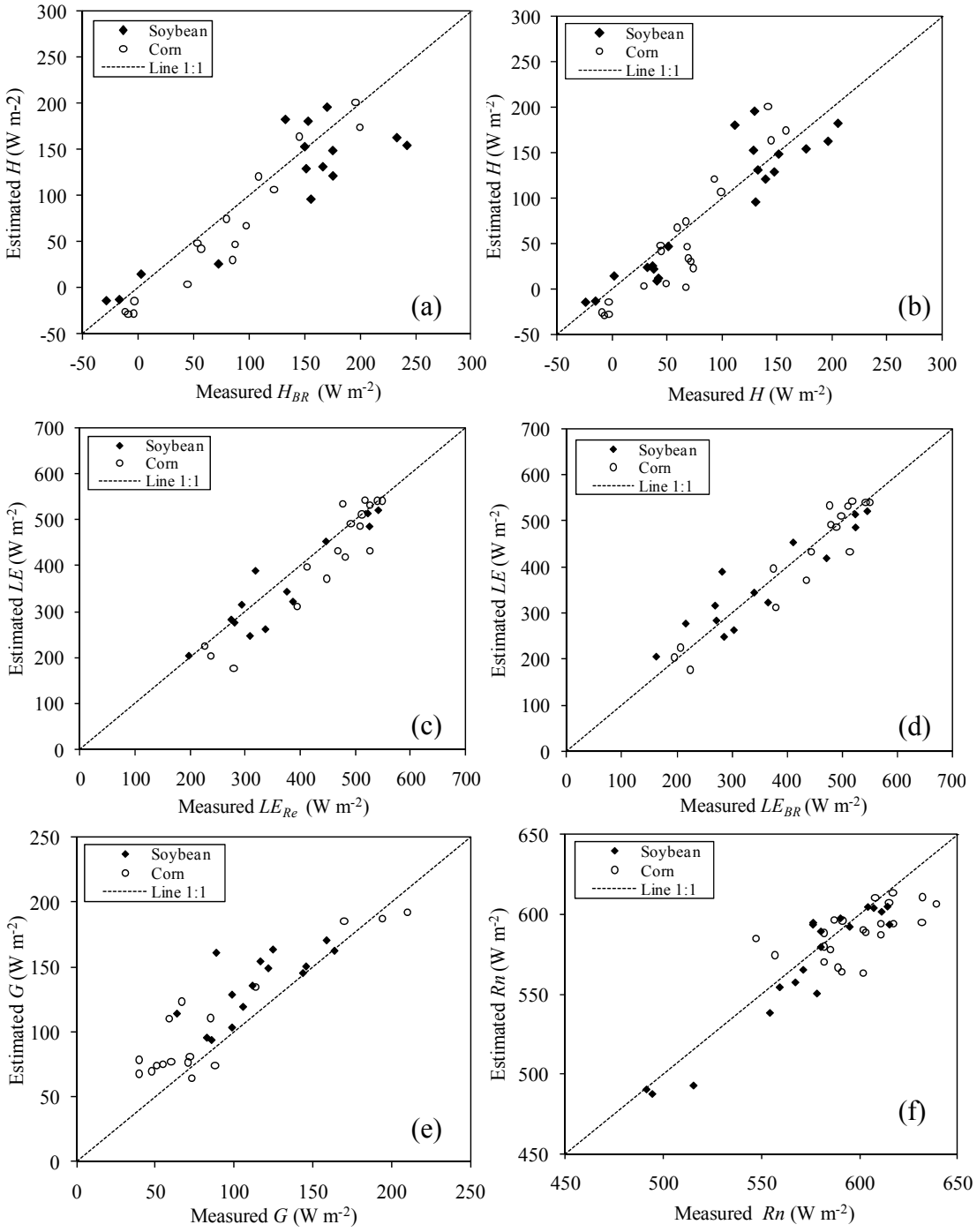

Fig. 2.3. Comparison between TSM estimates versus ground-based measured surface energy fluxes, estimated sensible heat flux compared with a) measured H and b) H_{BR} adjusted to Bowen ratio, estimated latent heat flux compared with c) LE_{BR} adjusted to Bowen ratio and d) LE_{Re} adjusted to residual, e) soil heat flux G, and f) net radiation Rn.

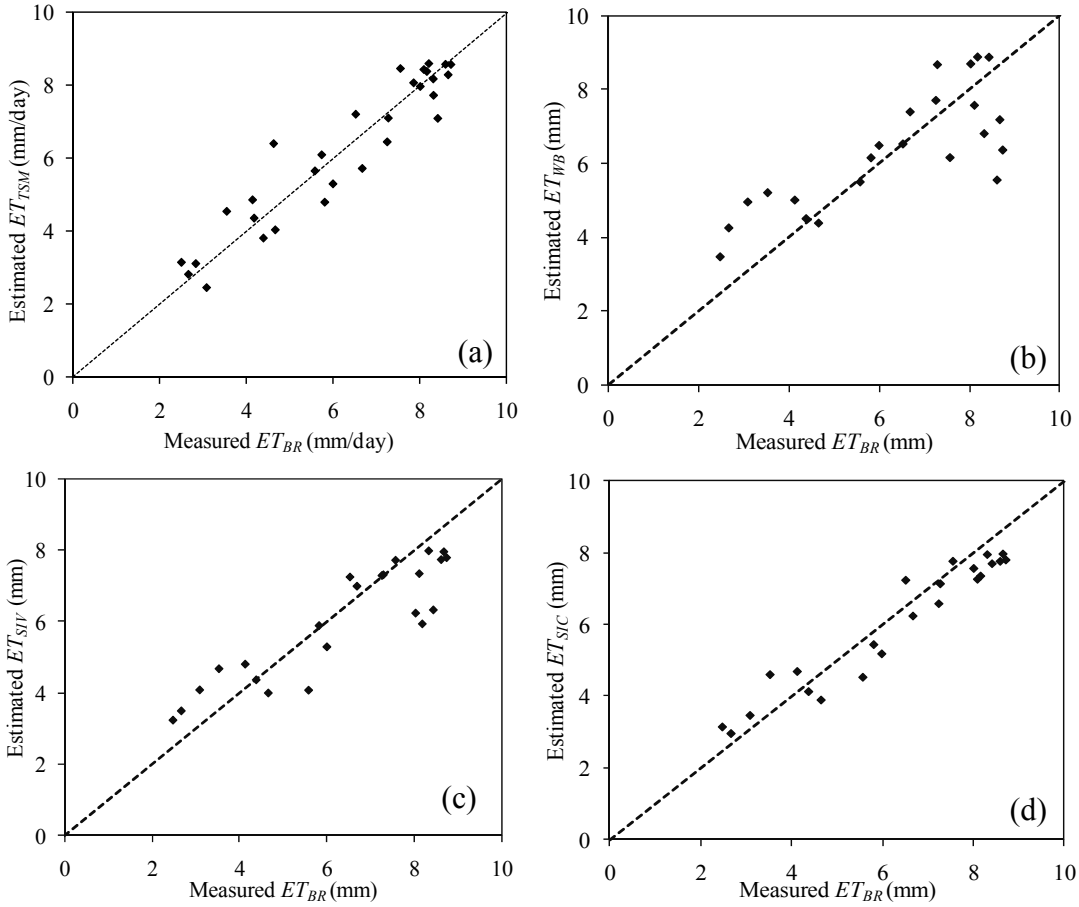

Fig. 2.4. Comparison between measured ET_{BR} and estimated ET a), ET_{TSM} b) ET_{WB} c) ET_{SIC}, and d) ET_{SIV} obtained using WB model, SIC, and SIV methods, respectively.

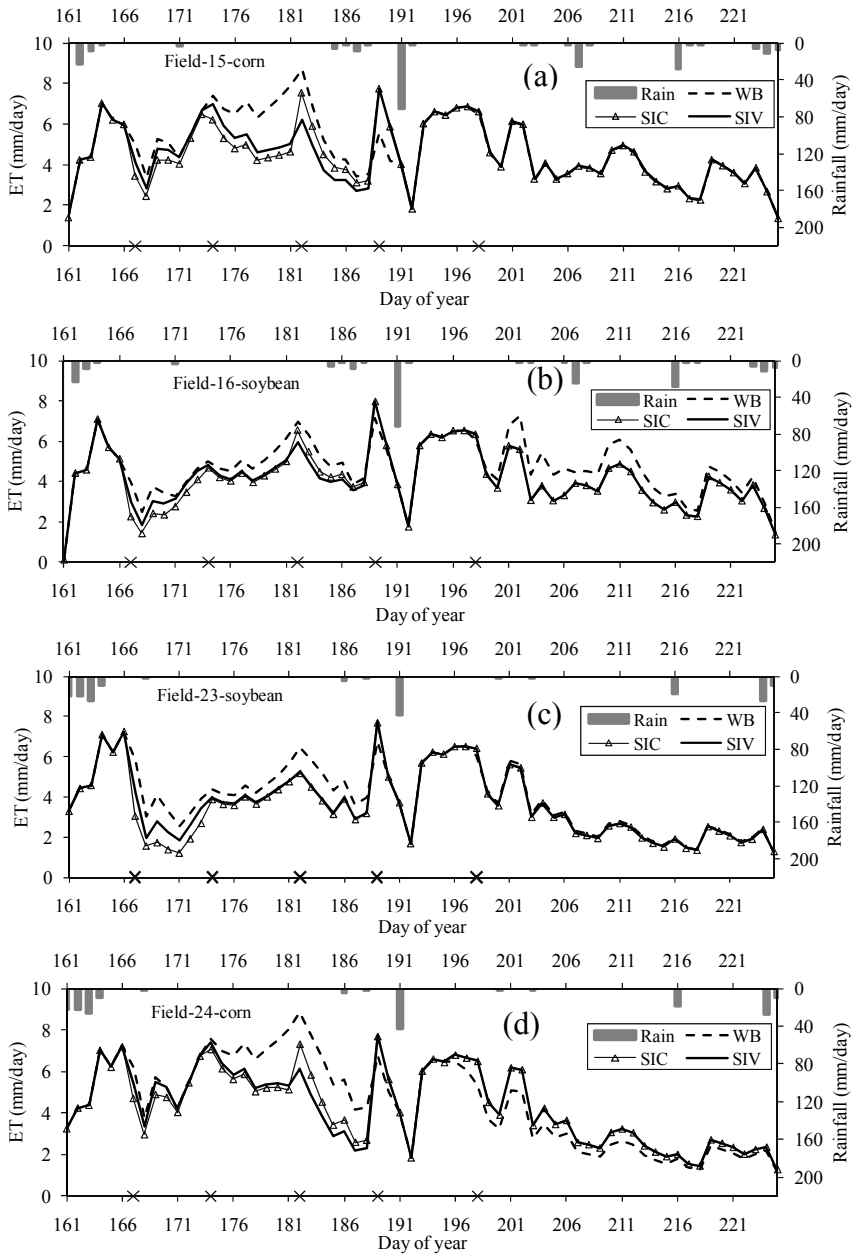

Fig. 2.5. Time series plots showing the estimated ET_{WB} (dashed lines), ET_{SIC} (lines with diamonds), ET_{VIC} (solid lines), the rainfall (gray bars), and the day of year of the images (cross) shown at the bottom axis of each subplot, for a) Field 15 corn, b) Field 16 soybean, c) Field 23 soybean, and d) Field 24 corn.

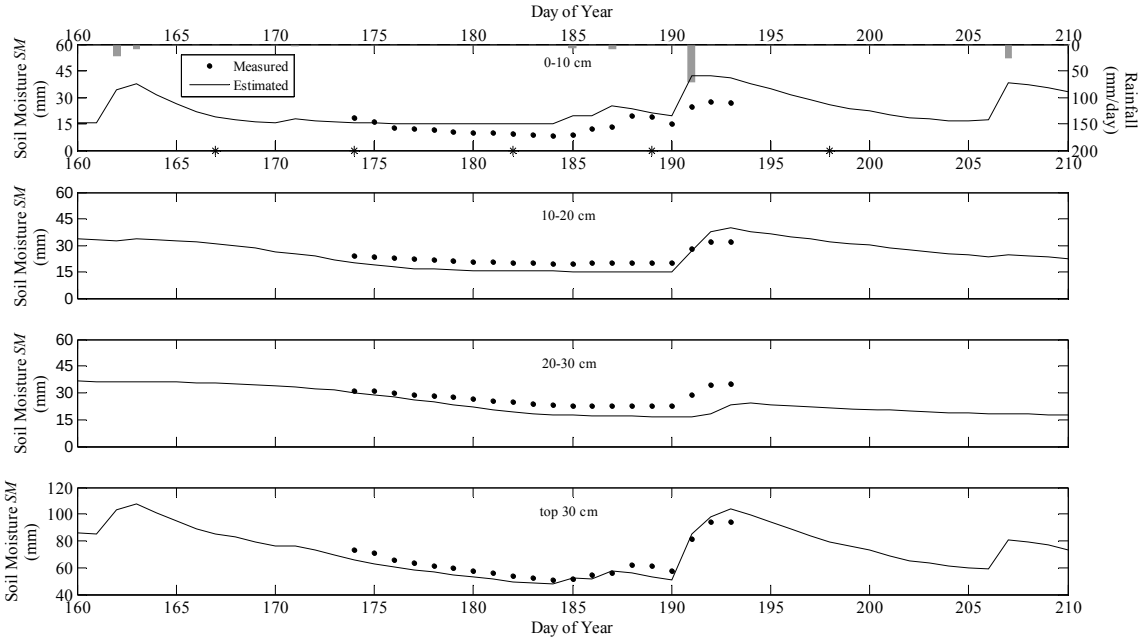

Fig. 2.6a. Time series plots of measured *SM* (dots) and estimated SM_{WB} (solid line) using the WB model for 0–10, 10–20, 20–30, and the top 30 cm soil layers for Field 15 corn with the rainfall events (gray bars) and the satellite overpass dates (stars).

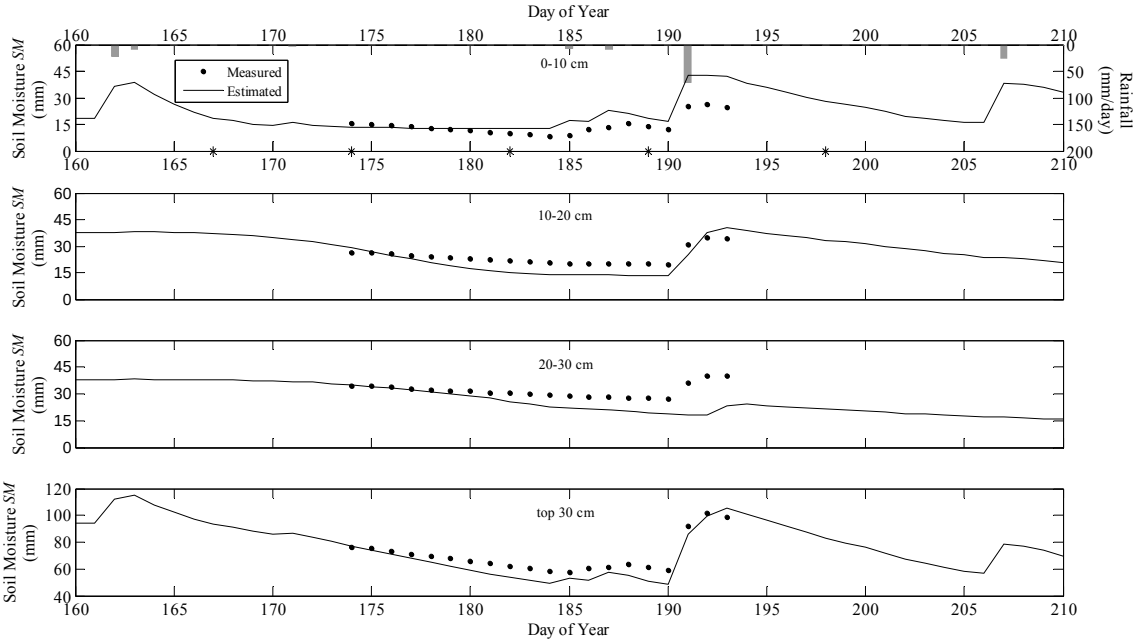

Fig. 2.6b. Time series plots for measured *SM* (dots) and estimated SM_{WB} using the WB model (solid line) for 0–10, 10–20, 20–30, and the top 30 cm soil layers for Field 16 soybean with the rainfall events (gray bars) and the images dates (stars).

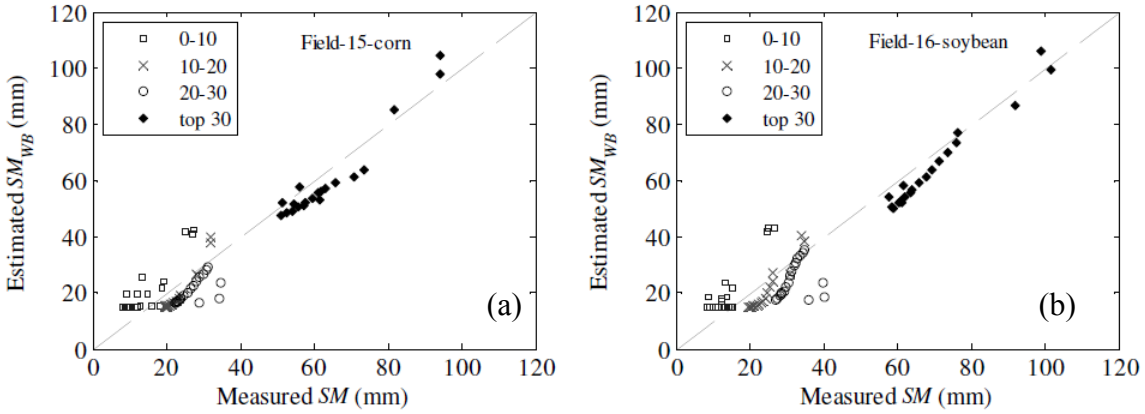

Fig. 2.7. Scatterplot of measured SM and estimated SM_{WB} using the WB model for a) Field 15 corn, and (b) Field 16 soybean for 0–10 (hollow squares), 10–20 (cross), 20–30 layer (hollow diamond), and the top 30 (solid diamonds) soil layers.

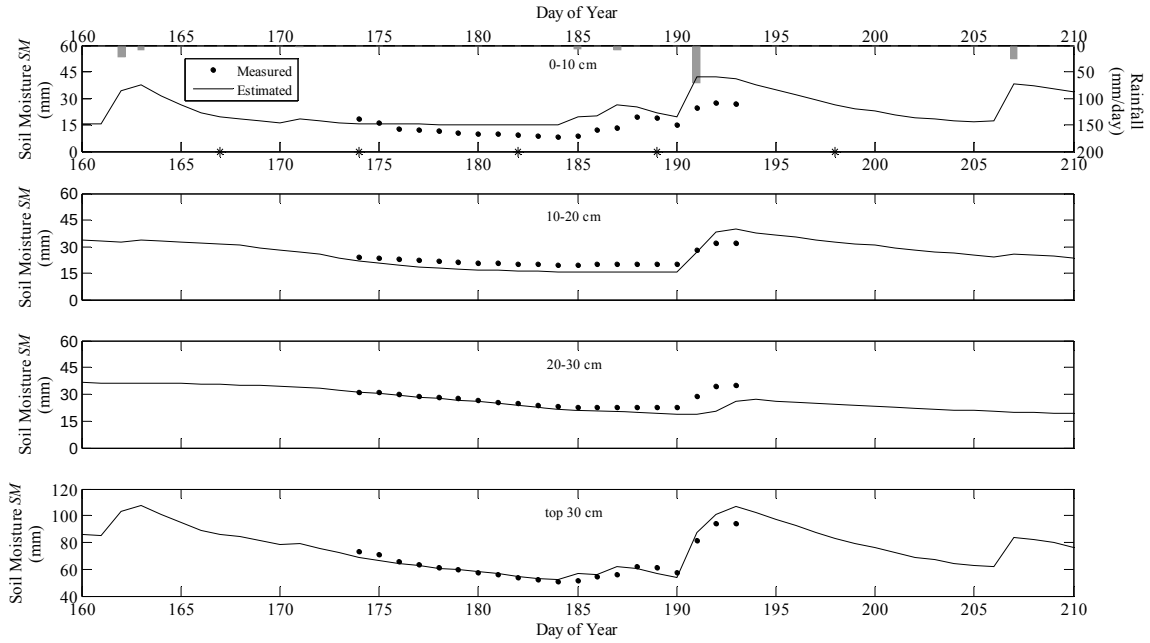

Fig. 2.8a. Time series plots for measured *SM* (dots) and estimated SM_{SIC} (solid line) using the SIC method for 0–10, 10–20, 20–30, and the top 30 cm soil layers for Field 15 corn with the rainfall events (gray bars) and the images dates (stars).

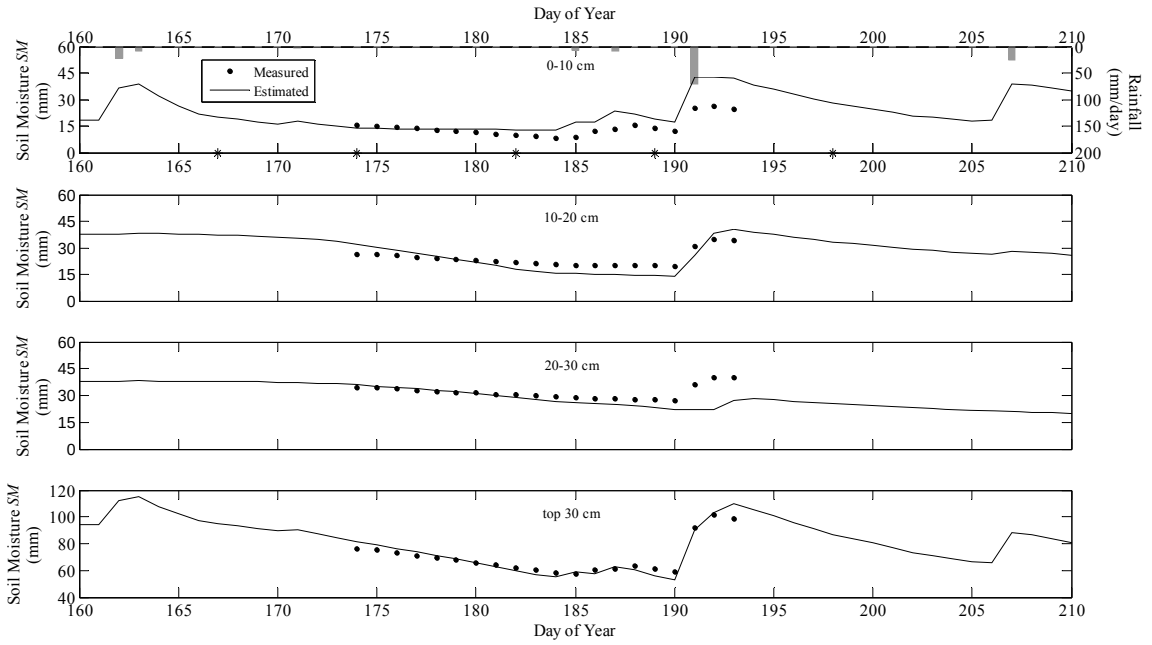

Fig. 2.8b. Time series plots for measured *SM* (dots) and estimated SM_{SIC} (solid line) using the SIC method for 0–10, 10–20, 20–30, and the top 30 cm soil layers for Field 16 soybean with the rainfall events (gray bars) and the images dates (stars).

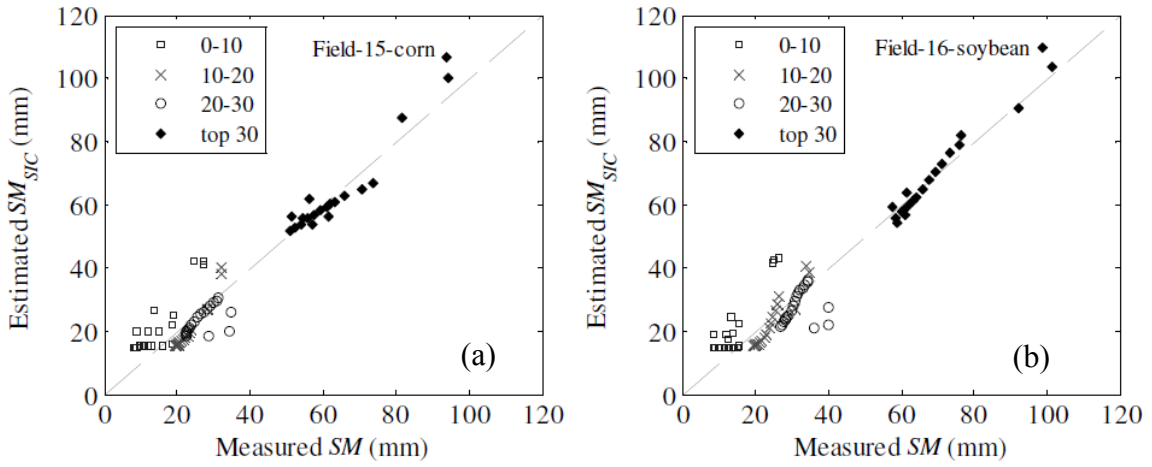

Fig. 2.9. Scatterplot of measured *SM* and estimated SM_{WB} using the WB model for a) Field 15 corn, and (b) Field 16 soybean for 0–10 (hollow squares), 10–20 (cross), 20–30 layer (hollow diamond), and the top 30 (solid diamonds) soil layers.

CHAPTER 3

SCINTILLOMETER-BASED ESTIMATES OF SENSIBLE HEAT FLUX USING LiDAR-DERIVED SURFACE ROUGHNESS[2]

Abstract

Estimation of sensible heat flux, *H*, using large aperture scintillometer (LAS) under varying surface heterogeneity conditions was investigated. Surface roughness features characterized by variable topography and vegetation heights were represented using data derived from the highly accurate Light Detection and Range (LiDAR) techniques as well as from traditional vegetation survey and topographic maps methods. The study was conducted at the Cibola National Wildlife Refuge, southern California, over a riparian zone covered with natural vegetation dominated with tamarisk trees interspersed with bare soil and the region characterized with arid to semi-arid conditions.

Estimates of *H* were obtained using different surface roughness features representations derived from both traditional and LiDAR methods to estimate LAS beam height ($z(u)$) at each increment u along its path, vegetation height, h_c, displacement height (d), and roughness length (z_0) combined with the LAS weighing function, $W(u)$, along the path. The effect of LAS 3D footprint was examined to account for the contribution from the individual patches in the upwind direction, hence on the estimates of *H*. The results showed better agreement between LAS and Bowen Ratio sensible heat fluxes when LiDAR-derived surface roughness was used especially when considering the LAS 3D footprint effects. We also found that, under certain conditions, the LAS path weighted h_c

[2] Coauthored by Hatim M. E. Geli, Christopher M. U. Neale, Doyle Watts, John Osterberg, Henk A. R. De Bruin, Wim Kohsiek, Robert T. Pack, and Lawrence E. Hipps.

and *d* obtained using the LAS weighting function *W*(*u*) is a good approximation to the 3D weighted footprint values.

3.1 Introduction

Scintillometer measurements of turbulence are used in hydrological, micrometeorological, agricultural, and water resources studies. Their importance and effectiveness rises from the ability to provide path-averaged and area-average estimates of sensible (*H*) and latent (*LE*) heat flux that cover large spatial scales. Depending on the type of instrument, these estimates could cover several kilometers (Meijninger et al. 2002a, 2002b; Chehbouni et al. 1999) as compared to Bowen ratio or eddy covariance systems which essentially provide local scale measurements of 100s of meters. They can be used as ground measurements for verification and calibration of hydrological, remote sensing algorithms, and regional atmospheric models that provide spatial estimates of surface energy fluxes.

Scintillometry is increasingly being applied following a period of extensive studies and improvements to theory of the scintillation method (Tatarskii 1961; Hill and Clifford 1978; Andreas 1990; De Bruin 2002). It is based on measuring light intensity fluctuations caused by the refractive scattering of turbulent eddies along a specific path of emitted electromagnetic radiation from a transmitter. These fluctuations represent a measure of the structure parameters of the refractive index (C_n^2), temperature (C_T^2), and humidity (C_Q^2), which can be related to each other using the relationships developed by Wesley (1976) and Hill et al. (1980). These relationships along with the Monin-Obukhov Similarity Theory (MOST) can be utilized to estimate *H* and *LE* as described by Wyngaard et al. (1971) and Andreas (1988).

Since both, the scintillation method and MOST were initially developed for, and hence have good performance in, conditions with homogeneous surfaces and flat terrain; their use over heterogonous surfaces and non-flat terrain is challenging and in some cases can provide less accurate estimates of surface energy fluxes. Also, because of the slanted path geometry of the scintillometer beam in certain situations, as well as varying topography and heterogeneously vegetated surfaces, their application for estimating surface energy fluxes requires special considerations (Hartogensis et al. 2003).

Over the past two decades most of the research effort on scintillometry focused on its applicability in handling more practical situations including different climatic regions, areas characterized with variable terrain, heterogeneous surfaces, and relatively increased surface roughness. Examples of such applications include the work by Meijninger et al. (2002a, 2002b) in which they provided estimates of area-averaged H and LE over the Flevoland agricultural fields that are completely flat but contained different kinds of crops representing the surface heterogeneity with no change in the roughness length, z_0, as estimated from traditional vegetation survey; the study presented by Meijninger et al. (2006) over the LIFTASS-2003 area which also contained different types of crops and trees but with slanted scintillometer path and variable terrain. In their analysis, they used topographic maps (1:25000) to estimate the scintillometer beam height, $z(u)$ with u as the dimensionless coordinate of the path length, and roughness length z_0. De Bruin et al. (1995) used estimates of displacement height (d) and z_0 from eddy covariance data in a study that took place over vineyard field in La Mancha, Spain. Their measurements were carried out during a fast growing stage of the vineyard so both z_0 and d varied with time which had introduced uncertainty in their estimates of H. They conducted a sensitivity

analysis using different values for d and concluded that estimates of H were less sensitive to changes in d. Note that the vineyard was rather short with maximum vegetation height of about 1.0 m and leaf area index (LAI) of 0.4. Also because of the irregular terrain along the path, De Bruin et al. (1995) used weighted average effective beam height by utilizing topographic maps adding to the uncertainty in their estimates of H. Note that, unlike the studies by Meijninger et al. (2002a, 2002b, 2006), in which the scintillometers were installed well above the surface and thus reliable estimates can be obtained with the free convection formula, in De Bruin et al. (1995) it was installed relatively close to surface at about 3.25 m. Hartogensis et al. (2003) developed formulas to properly estimate scintillometer effective height, z_{eff}, considering the effects of the slanted path of the scintillometer beam height, non-flat terrain, and the stability conditions that lead to improved estimates of H. Their analysis was carried over the La Poza region in Mexico, a region characterized by heterogeneous land surface and variable terrain, where z_0 determined from vegetation survey and the $z(u)$ estimated from topographic maps.

In most of these research examples the use of traditional methods i.e. topographic maps and vegetation survey to estimate $z(u)$ and the related surface roughness parameters makes it less accurate and challenging to properly represent surface heterogeneity and roughness. These methods in some cases, as for the conditions of the current study, could lead to misrepresentation of the actual variability of the terrain and hence $z(u)$. Also to properly characterize surface heterogeneity in areas covered with mixed natural vegetation with variable height interspersed with bare soils, z_0 and d need to be estimated reasonably well from h_c and that could be quite an issue.

The recent and significant advances in the remote sensing technique known as the Light Detection and Ranging (LiDAR) has resulted in the unprecedented capability of providing highly accurate representation of the Earth's surface and its features. The LiDAR in this study is a system consisting of a sensor that emits a laser beam at high frequency (greater than 150 kHz) and receives the reflected light at a specific wavelength. It is usually an airborne mounted system flown over the required region combined with Global Positioning System (GPS) and Inertial Measurements Units (IMU). It collects point clouds of densely spaced accurately geo-referenced elevation data with accuracy of up to few centimeters. These data can later be used to generate maps of the three dimensional Earth's surface and its features including ground surface elevation and vegetation height maps (Schmid et al. 2008).

The question being asked here: will the use of LiDAR-derived surface features (i.e. topography and canopy heights) available at spatial resolution of up to 1.0 m or less to represent surface roughness and heterogeneity, as opposed to using traditional methods, improve the scintillometer based estimates of *H*? In other words, what will be the effect of using measured values to characterize surface features on the scintillometer-based estimates of *H*? In order to find an answer for such a question we tried to identify and quantify these effects by investigating the incorporation of LiDAR-derived surface features into Large Aperture Scintillometer (LAS) measurements taken over a heterogeneous area to estimate *H* under unstable and stable atmospheric conditions. We also considered the effects of representing this variability in surface features along the LAS path as well as at its footprint that could cover several hundred meters in the upwind direction.

3.2 Methods

3.2.1 Sensible heat flux

The scintillometer measures the intensity flucuations of the refractive index of air (n) that mostly influence the propagation of EM. This scintillation can be expressed in terms of the structure parameter of the refractive index (C_n^2) using the statistical characteristics of random functions (i.e. structure functions) to describe the spatial structure of turbulence. The variance of the logarithm of the intensity fluctuation (σ_{Int}^2) of the measured light intensity for a spherical wave propagating through homogenous refractive atmosphere is related to C_n^2 as described by Tatariskii (1961) and Wang et al. (1978) as

$$\sigma_{Int}^2 = 0.892 D^{-\frac{7}{3}} L^3 \left\langle C_n^2 \right\rangle \tag{1}$$

where the angle brackets $\langle\ \rangle$ represent the path weighted average, L the path length, and D the aperture diameter.

Generally, C_n^2 is related to the structure parameters of temperature, humidity, and the covariance of temperature and humidity fluctuations C_T^2, C_Q^2, and C_{TQ}, respectively (Hill et al. 1980). For scintillometers operating in the visible to infrared region of the electromagnetic spectrum–as the LAS used in this study–turbulence fluctuation described by C_n^2 is more sensitive to C_T^2 as described by Wesely (1976) as

$$C_T^2 = C_n^2 \left(\frac{T^2}{0.78 \times 10^{-6} P} \right)^2 \left(1 + \frac{0.03}{\beta} \right)^{-2} \tag{2}$$

where T is the temperature (K), P is the air pressure (Pa), and β is the Bowen ratio.

Wyngaard et al. (1971) introduced a general formula in which the scintillation method can be combined with MOST to obtain estimates of H as

$$\left[C_T^2\left(z_{eff}-d\right)^{2/3}/\theta_*^2\right]=f_T\left(\left(z_{eff}-d\right)/L_{MO}\right) \tag{3}$$

where z_{eff} is the scintillometer effective height (m), d the displacement height (m), $L_{MO}=Tu_*^2/kg\theta_*$ the Monin–Obukhov length (m) with k the von Kármán constant taken as 0.40 and g the gravitational acceleration, $\theta_*=-H/\rho C_P u_*$ the temperature scale of turbulence with ρ the air density (kg m^{-3}) and C_p the specific heat of air (J kg^{-1} K^{-1}), and f_T a dimensionless universal function with different formulation for stable and unstable atmospheric conditions (Wyngaard et al. 1971). Herein for unstable conditions we applied the modified form of f_T by Andreas (1989) as

$$f_T=4.9\left(1-6.1\left(z_{eff}-d\right)/L_{MO}\right)^{-2/3} \tag{4}$$

Note that, a value of 9.0 was reported by De Bruin et al. (1993) for the constant 6.1 (Wyngaard et al. 1971; Andreas 1989). The effect of using a constant 9.0 is briefly discussed in section 4 as it is beyond the objective of the paper.

For stable conditions f_T can be expressed by the modified form by Hartogensis et al. (2005) and De Bruin (2005a) as

$$f_T=4.7\left(1+1.6\left(\left(z_{eff}-d\right)/L_{MO}\right)^{2/3}\right) \tag{5}$$

The friction velocity, u_*, is estimated using the standard Businger-Dyer flux profile (see e.g. Panofsky and Dutton 1984) as

$$u_*=\frac{kU}{\ln\left(\frac{z_{eff}-d}{z_0}\right)-\psi_m\left(\frac{z_{eff}-d}{L_{MO}}\right)+\psi_m\left(\frac{z_0}{L_{MO}}\right)} \tag{6}$$

where ψ_m is the stability correction function for momentum transfer. For unstable conditions $\psi_m = 2\ln[(1+x)/2] + \ln[(1+x^2)/2] - 2\arctan(x) + \pi/2$, with $x = [1 - 16(z_{eff}/L_{MO})]^{1/4}$, and for stable conditions $\psi_m = 5$.

Under free convection (i.e. very unstable conditions) with - $(z\text{-}d)/L_{MO} > 1$, H becomes independent of L_{MO} and can be estimated as described by Andreas (1991) as $H = \rho c_P b z (g/T)^{1/2} (C_T^2)^{3/4}$, with $b = 0.47$.

3.2.2 Utilizing LiDAR data

The LiDAR data were incorporated in the analysis first by using the detailed surface topography to estimate the LAS beam height along the path, $z(u)$, a term that is necessary for estimating z_{eff}. Secondly, we used the detailed vegetation height, h_c, map to estimate the surface roughness parameters i.e. d and z_0. Note that the spatial resolution of LiDAR-derived topographic and vegetation height maps is 1.0 m.

The LAS effective height z_{eff} needs be estimated iteratively using the approach described by Hartogensis et al. (2003) where they showed the importance of considering the effect of the stability conditions represented by L_{MO}.

$$z_{eff}^{-2/3} f_T\left(\frac{z_{eff}}{L_{MO}}\right) = \int_0^1 z(u)^{-2/3} f_T\left(\frac{z(u)}{L_{MO}}\right) W(u)\,du \qquad (7)$$

where $z(u)$ is the variable scintillometer beam height along the path, z_{eff} estimated at every time increment of the available data as L_{MO} changes with time, and $W(u)$ the LAS weighting function along the path representing the contribution of $C_n^2(u)$ to the total LAS signal at each location u and. $W(u)$ has a bell shape with maximum value at the center of the path and zeros at both ends (Appendix C).

The displacement height, *d*, which represents and quantifies surface obstacles and roughness due to the presence of vegetation, as for the current study, can be estimated as 2/3 h_c (Brutsaert 1982). Because of the varying canopy height along the LAS path, an integrated displacement height *d* is estimated by evaluating the elemental *d(u) = 2/3 * $h_c(u)$* at each increment *u* along the path and then weighted by incorporating the LAS weighting function *W(u)*; an aggregation approach described by Shuttleworth et al. (1997) and Chehbouni et al (1999).

$$d = \sum W(u)d(u) \tag{8}$$

Similarly, an integrated roughness length is estimated as a function of the incremental $z_0(u)$ and *d(u)* (Shuttleworth et al. 1997) as

$$\ln^{-2}\left(\frac{z_b - d}{z_o}\right) = \sum_u W(u)\ln^{-2}\left(\frac{z_b - d(u)}{z_o(u)}\right) \tag{9}$$

where z_0 is the area-average or path-average roughness length, z_b the blending height estimated as described by Wood and Mason (1991) and can be approximated as a function of L_h the horizontal length scale of heterogeneity, u_*, and U the spatially average wind speed as $z_b \cong 2(u_*/U)^2 L_h$. An iterative approach was followed by first assuming an initial value for z_0, based on h_c as described in Brutsaert (1982) and then solve for u_* and z_b.

Moreover, in cases where the surface exhibits some variability in topography, canopy height, or both in all directions of the LAS path especially in the upwind direction areas, these variables (i.e. *d* and z_0) need to be evaluated by considering the effects of the LAS footprint as recommended by Hartogensis et al. (2003). Herein we also considered representing these variables using a 3D footprints model as discussed in section 2c.

3.2.3 Footprint model

The turbulence fluxes obtained for example by Bowen ratio and eddy covariance flux towers represent the weighted integral contribution from the upwind area of the measured fluxes that is called as the source area or the footprints. In the case of LAS measurements a 3D footprint can be utilized to determine the weighted contribution surface features or topography in the upwind direction. Specifically, in areas that exhibits surface heterogeneity and topographic variability the use of 3D LAS footprint is the recommended approach to better represent these features (Hoedjes et al. 2002; Meijninger et al. 2002a; Hartogensis et al. 2003). To obtain the weighted contribution of the footprint different models have been suggested in the literature. We opted to use the model described by Horst and Weil (1992, 1994) that is based on the analytical solution of the advective-diffusion equation.

Horst and Weil (1992) described that the footprint *f* relates the vertical turbulence flux measurements $F(x,y,z_m)$ at height z_m to the spatial distribution of the surface fluxes $F_0(x', y', z'=0)$ as

$$F(x, y, z_m) = \int_{-\infty}^{\infty}\int_{-\infty}^{x} F_0(x', y', z'=0) f(x-x', y-y', z_m) dx' dy' \tag{10}$$

with *x* and *y* represent the upwind and the crosswind distances, respectively, from the point of measurement. The footprint $\bar{f}^y$ function can be approximated by (Horst and Weil 1994)

$$\bar{f}^y(x, z_m) \cong \frac{d\bar{z}}{dx}\frac{z_m}{\bar{z}^2}\frac{\bar{u}(z_m)}{\bar{u}(c\bar{z})} A \exp\left[-z_m / b\bar{z}\right]^r \tag{11}$$

where z_m is the measurement height, $\bar{z}$ the mean plume height for diffusion from a surface source, and $\bar{u}(z)$ the mean wind speed. Coefficients *A*, *b*, and *c* are functions of the gamma function,Γ, and *r* the Gaussian plume model shape parameter (see Horst and Weil (1992)).

To estimate the 3D footprint for the LAS, the footprint function $\bar{f}^{y}$ is combined with the LAS spatial weighting *W*(*u*) as suggested in Hoedjes et al. (2002) and Meijninger et al. (2002a, 2006).

3.2.4 Correction for saturation effects

LAS measurements in some cases can be affected by saturation of C_n^2 signal at longer path lengths and at high values of *H* (Kohsiek et al. 2006). The limits for which saturation occurs can be estimated by methods described for example by Kohsiek et al. (2006). Inspection of the *H* estimated by LAS versus the Bowen ratio method over the study area indicated that the saturation limit falls between *H* values of 200–300 W m^{-2} which typically matched the maximum limits of the LAS measurements while the Bowen ratio showed about 400–500 Wm^{-2} in some cases with 100–200 W m^{-2} higher indicating possible saturation effects.

We corrected for saturation effects following the procedure recommended by Kohsiek et al. (2006) in which they described how to obtain saturation correction parameter for the specified LAS setting based on the path length, *L*, aperture diameter, *D*, and operating wavelength,λ, (for details refer to Kohsiek et al. 2006). Note that we experienced saturation effects on two different LAS locations out of three at the study area as described in the results and discussion section.

3.2.5 The BR method

Sensible and latent heat fluxes, *H* and *LE,* were measured based on the standard Bowen ratio method of Bowen (1926) modified later by Monteith and Unsworth (2008). The BR method assumes that the sources and sinks for heat and water vapor are the same. In other words the exchange coefficients for heat and water vapor are equal i.e. $K_h=K_e$ (see e.g. De Bruin et al. 1993, 1999), which is not necessarily always valid and applicable over tall heterogeneous vegetation. The validity of this assumption and its effect on the BR measurements will be discussed in more detail in section 4.

The BR method is not the preferred method of measuring *H* and *LE* especially over heterogeneous surfaces covered with relatively tall vegetation (De Bruin et al. 1993, 1999) such as the case in certain areas within CNWR. This is due to the assumptions of the BR method that $K_h=K_e$ may not be valid because sources and sinks of *H* and *LE* are different. This leads to differences in the zero plane displacement height, *d*, for heat, vapor, and momentum fluxes as the surface becomes more heterogeneous. In addition, BR systems are known to have a problem in accurately estimating relatively small gradients of *T* and *q* that generally occur over forests either due to mixing or because of low evaporation rates (Baldocchi et al. 1988). However, tamarisk trees are phreatophytes and have relatively high evaporation rates which enhance the gradient of humidity. In addition, the vegetation at CNWR was relatively dense with average *LAI* ranging between 2.5 at Swamp to 4.0 at Slitherin. Hence assuming that the value of *d* is similar for heat and momentum flux transfers might not result in significant error. Therefore we used the BR measurements for comparison purposes. Another factor to point out is that most scintillometer based studies referenced earlier, used eddy covariance measurements

for verification purposes. These systems measure H and LE independently and typically result in an energy balance closure of about 85% (Massman and Lee 2002) with currently no standard procedure of establishing energy closure. The BR method forces energy balance closure using the Bowen ratio.

3.3 Study area and data collection

3.3.1 The study area

The study was conducted in riparian forest at the Cibola National Wildlife Refuge (CNWR), southern California. The data were collected during the summer of 2008 over an area of approximately 5 km by 4 km centered at 114° 41' W 33° 16' N. The region is considered arid to semi-arid with annual rainfall of less than 100 mm. The study area is surrounded from the north, east and south sides by an agricultural drain, running from north to south, for the excess water from the Palo Verde Irrigation District (PVID) and next to it the Colorado River. The west side consists of highlands and hills with sparse desert vegetation (Fig. 3.1). The area is mainly covered (90 %) with a dense tamarisk (Tamarix ramosissima) with the remainder a mixture of native trees and shrubs including arrowweed, mesquite, and cottonwood interspersed with bare soils (Fig. 3.2). The data were acquired as part of a large study funded by the US Bureau of Reclamation, with the purpose of water resource management in the PVID.

3.3.2 The LAS data

Two LAS instruments were installed within the area under three different layout configurations to capture the variable vegetation density. The LAS layout consisted of 3 paths (Fig. 3.2): Path 1 with a length of 1832 m extended over high density and relatively

tall tamarisk stands between the Mulligan tower with the transmitter at a height of 5.84 m above ground and Sara Hill where the receiver was at a higher elevation positioned on a tripod at 1.53 m above ground; Path 2 with a length of 1052 m between Mulligan tower (transmitter) and Diablo tower with the receiver at a height of 6.16 extending over a medium density and height tamarisk canopy; Path 3 with a length of 1621 m between Swamp tower with the transmitter at a height of 5.19 m and Diablo tower (receiver) extended over low density shorter canopy with mixed tamarisk and arrowweed (Fig. 3.4).

The LAS system was a Boundary Layer Scintillometer BLS900 from Scintec AG Rottenburg, Germany with aperture diameter D =0.15 m operating at a wavelength of 880 nm. The measurements were taken at 1- Hz over 1-minute averaging time periods to provide C_n^2 , C_T^2 , T_a, P, and H. LAS measurements for Path 1 were taken during May 12th –18th providing a total of 7 days of data; for Path 2 a total of 6 days during September; for Path 3 between April 14th –May 31st, and 7 days in June providing a total of 51 days.

3.3.3 The BR data

Bowen Ratio (BR) systems developed by Radiation and Energy Balance Inc. Seattle, USA (REBS) were used to provide the energy balance fluxes including the net radiation (Rn), the latent heat (LE), soil heat (G) and sensible heat (H) fluxes. The BR has an automatic exchange mechanism (AEM) which reduces the measurements biases in the temperature and humidity gradients by switching the positions of the upper and the lower sensors every 15 minutes. Soil heat flux plates combined with a soil moisture and temperature sensors provide measurements of G. A REBS Q7.1 net radiometer and a pyranometer were used to measure net and incoming radiation. There were also wind speed and direction sensors; a set of two temperature and humidity sensors installed on

the two arms of the AEM, 1 m apart; a barometric pressure sensor; and a Campbell Scientific Inc. CR10X data logger. Measurements were taken at 30-second intervals and the fluxes were estimated at 30-minute moving averages. Three BRs were deployed in the CNWR; the first BR deployed on the Slytherin tower at a height of 7.32 m above the ground surface near the center of Path 1 in an area characterized by dense tall tamarisk trees with average height of about 5.5 m; the second BR deployed at Diablo tower at a height of 6.8 m in an area characterized by medium density trees with average height of 4.0 m; the third BR deployed at the Swamp tower at a height of 5.5 m in an area characterized by a mixture of tamarisk and arrowweed shrubs with average height of 2 m interspersed with bare soil. The final BR measurements of *H* were cleaned from spikes that occur during transition from stable to unstable conditions or at sunrise and sunset when the Bowen ratio approaches negative 1 (for detailed description of the data see Chatterjee 2010).

3.3.4 The LiDAR data

LiDAR data were collected with the Utah State University (USU) Lidar-Assisted Stereo Imager (LASSI) system from an altitude of approximately 600 m above ground level at an average point density of over 2 points per square meter. The LASSI system mounted in the USU CESSNA TP206 remote sensing aircraft consists of a full-waveform Riegl Q560 LiDAR transceiver, a Novatel SPAN LN-200 GPS/IMU Navigation System. The absolute point accuracy is approximately 7 cm and relative accuracy is approximately 2 cm. The point cloud data were processed and classified to separate ground returns from canopy returns and obtain 1-m digital elevation models and vegetation height. The resulting topography and vegetation maps are shown in Fig. 3.3.

To evaluate the performance of LAS without the use of LiDAR data, we used traditional topographic maps for the region to estimate $z(u)$. A digital scan topographic map was obtained from the U.S. Geological Survey (USGS) at scale 1:24,000 (USGS 2010) to compare with our LiDAR-derived topographic map.

3.4 Results and discussion

Three different estimates of H were made, H_{LAS}, H_{LiD_PA}, and H_{Ftp} based on the surface roughness representation. H_{LAS} were estimates based on using topographic maps for determining $z(u)$ and on using an average h_c estimated based on vegetation survey in areas around the center of the LAS path because of the considerable weighted contribution to LAS measurements as described in sections 2. H_{LiD_PA} were those based on using LiDAR-derived measurements of $z(u)$ and h_c along the LAS path. H_{Ftp} refers to estimates of H based on $z(u)$ and h_c from the LiDAR-derived measurements weighted with the LAS 3D footprints oriented with the wind direction. These estimates of H_{LAS}, H_{LiD_PA}, and H_{Ftp} were compared to measured H_{BR} and the performance statistics presented in terms of the root mean square error (RMSE), mean absolute error (MAE) and the bias (BIAS).

Note that De Bruin et al. (1993) reported a value of 9.0 for the constant 6.1 in Eq. (4), which was used in this analysis (Wyngaard et al. 1971). Their value was based on data from the plains of La Crau, France, while Wyngaard et al. (1971) was based on data from Kansas. Note that both values were based on studies conducted over areas which we believe have a different type of heterogeneity than CNWR. We compared the effect of using both coefficients with data from Path 1 and 2 to show the relative effects on

estimates of *H*. We also tested the use of the free convection formula in providing estimates of *H* over Path 1 and 2.

3.4.1 Path 1

Over Path 1, both H_{LAS} and H_{LiD_PA} systematically overestimated H_{BR} (Fig. 3.5) with a BIAS of 56 and 15 W m^{-2}, respectively (Table 3.1), though H_{LiD_PA} performed better. We did not consider the effect of the humidity correction represented by β in the term $(1+0.03/\beta)$ (Eq. 2). Generally, for $\beta > 1$ the effect of humidity correction is negligible and for $\beta > \sim 0.6$ it is less than 10% (Hartogensis et al. 2003) and it can safely be neglected (De Wekker 1996). Over Path 1, β values were typically between 0.60–1.0 with only few instances where it was less than 0.60. Moreover, Eq. 2 (Wesely 1976) resulted from the assumption that the correlation coefficient, R_{Tq}, between the temperature *T* and the specific humidity *q*, is $|R_{Tq}| = 1$ as described by Moene (2003). De Bruin et al. (1999) showed that the BR method is based on the assumption that $|R_{Tq}| = 1$. But findings from other studies as Hoedjes et al. (2007) and De Bruin et al. (2005b) carried over areas with similar surface settings with data obtained from eddy covariance systems suggested that $|R_{Tq}|$ may deviate from 1. Also De Bruin et al. (1999) showed that *T* and *q* behave similarly when $|R_{Tq}| = 1$ and differently with $|R_{Tq}| < 1$ based on theoretical review and data collected by eddy covariance and BR systems over different types of surfaces and climatic regions. In our case, if $|R_{Tq}|$ was known and < 1 a correction would ultimately result in increased values of C_T^2 leading to an overestimation of the sensible heat flux, a condition similar to the findings of Moene (2003), Hoedjes et al. (2007), and Chehbouni et al. (2000).

H_{LiD_PA} resulted in lower RMSE and MAE of 37 and 30 W m^{-2} compared to 50 and 39 W m^{-2}, respectively, for H_{LAS} (Table 3.1). Also H_{LiD_PA} resulted in reduced scattering around the 1:1 line compared to H_{LAS} as shown in Fig. 3.5. This indicates the improvements in estimates of H_{LiD_PA} as compared to H_{LAS}. We looked into the values used to represent the surface roughness and the LAS beam height (i.e. h_c, d, z_0, and $z(u)$) as well as the weighted average of the LAS beam height (z_{wt_ave}) in both estimates of H_{LAS} and H_{LiD_PA}. It appears that there were no differences between both values of h_c (3.2 m) and z_0 (0.26 m) used to estimate H_{LiD_PA} and those for H_{LAS}. on other words there were basically less or no differences in surface roughness due to vegetation when using data either from LiDAR or traditional vegetation survey. On the other hand the value of z_{wt_ave} used to estimates H_{LiD_PA} showed a difference of about 2.0 m lower than those used to estimate H_{LAS}. This supports the evidence that using the LiDAR-derived topography has improved the LAS estimates of H.

We looked into the effect of using the value of 9.0 (De Bruin et al. 1993) instead of the constant 6.1 (Wyngaard et al. 1971; Andreas 1989) in Eq. (4). Estimates of H_{LAS} resulted in higher values of RMSE of 61 W m^{-2}, MAE of 51 W m^{-2}, and BIAS of 46 W m^{-2} compared to those obtained using a constant of 6.1 shown in Table 3.1. Improvements from the use of LiDAR-derived canopy heights were also observed for H_{LiD_PA} with RMSE of 44 W m^{-2}, MAE of 34 W m^{-2}, and BIAS of 26 W m^{-2} but are still worse than using a value of 6.1. It appears that the values suggested by Wayngaard et al. (1971) worked better for this data set.

The free convection formula was tested for providing estimates of H under all unstable atmospheric conditions and with the constants of 6.1 (Eq. 4) and b= 0.47 (see

section 2a). The estimated H_{LAS}^{FC} resulted in RMSE of 70 W m^{-2}, MAE of 55 W m^{-2}, and BIAS of -9 W m^{-2} while $H_{LiD\_PA}^{FC}$ resulted in RMSE of 72 W m^{-2}, MAE of 57 W m^{-2}, and BIAS of -29 W m^{-2}. Thus the free convection formula resulted in underestimation of both H_{LAS}^{FC} and $H_{LiD\_PA}^{FC}$. It also provided considerably higher RMSE values compared to those obtained from correcting for atmospheric stability (Table 3.1). On the other hand this showed that the use of LiDAR data did not have effects on the LAS results when comparing the RMSE for H_{LAS}^{FC} and $H_{LiD\_PA}^{FC}$.

3.4.2 Path 2

Both estimates of H_{LAS} and H_{LiD_PA} underestimated H_{BR} with a BIAS of -27 and -6 W m^{-2} (Table 3.2). Note that, over Path 2 and Path 3 (see section 4c); the humidity correction effect (Eq. 2) has also been neglected since the estimated $\beta > 1$. The issue that arises over Path 2, as well as Path 3 (section 4c), is the saturation effects which were already checked and corrected for following the approach described by Kohsiek et al. (2006) (section 3d). Note that saturation correction over Path 2 on average was about 30%. The study by Kohsiek et al. (2006) showed that, in some cases, even when correcting for saturation, LAS would still result in underestimated sensible heat flux values and this, explains, in part, the related underestimation. H_{LiD_PA} showed a slightly better performance with about 3 W m^{-2} lower in RMSE compared to H_{LAS}. Similarly, as shown for Path 1, we looked into the values of z_{wt_ave}, h_c and z_0 used for both estimates of H_{LAS} and H_{LiD_PA} (Table 3.3). The values of z_{wt_ave} used in both estimates of H_{LAS} and H_{LiD_PA} did not show much difference while h_c had slightly lower values for those used with H_{LAS} compared to H_{LiD_PA}. Relating the value of h_c to the performance of LAS

estimates of H, it can be seen that lowering h_c hence z_0 have lead to improved estimates of H_{LiD_PA}.

The result of the effects of using a value of 9.0 instead of 6.1 for the constant in Eq.4 on data from Path 2 was similar to Path 1 resulting in higher RMSE, MAE and BIAS. Likewise the use of the free convection formula for estimating H resulted higher deviations from the measured H values like the results in Path 1.

3.4.3 Path 3

Over Path 3; H_{LiD_PA} overestimated H_{BR} with a BIAS of 12 W m^{-2} while H_{LAS} underestimated with a value of -20 W m^{-2} (Table 3.4). Note that over Path 3 we did not consider humidity correction (Eq. 2) as the resulted $\beta > 1$. However, corrections for saturation effects were implemeted. From Fig. 3.7 it can be seen that the resulting H_{LAS} underestimated for most H values of ≈250 W m^{-2} and higher, an expected behavior even when considering saturation correction and similar to the findings of Kohsiek et al. (2006). The saturation correction over Path 3 on average was about 45% which higher than that over Path 2. H_{LiD_PA} showed a better performance with a lower RMSE of 41 W m^{-2} compared to 52 W m^{-2} for H_{LAS}. The value of z_{wt_ave} used to estimate H_{LiD_PA} was about 1.3 m higher than those used to estimate H_{LAS} while the value of h_c about 1.0 m higher.

Note that over Path 3 we used the average of H_{BR} from the two towers in Diablo and Swamp as well as average wind speed in the analysis. When we compared our estimates with H_{BR} from only the Diablo tower using the corresponding wind speed, the results of the comparison, not shown here, provided generally similar results but with higher RMSE values.

Moderate wind speed conditions were observed over the study area with only few occasions with high values. For the three paths, the maximum wind speed reported during the analysis was about 7.0 m s^{-1}. If divided into 3 categories, about 20% of the wind speed values were above 5 m s^{-1}, 55% between 3–5 m s^{-1}, and 25% below 3 m s^{-1}. During the midday hours most of the wind speed values were above 3.0 m s^{-1}, which corresponds to typical values of $H \geq 250$ W m^{-2} as reported by the BR systems. Figs. 3.5- 3.7 show that most of the correction in estimates of H resulting from the use of LiDAR data clearly occurs for these higher H values.

These results shown for all three paths indicate that path-average estimates of H made by incorporating LiDAR-derived data (e.g. $z(u)$, h_c, and z_0) improves estimates of H. Differences in representative values of either $z(u)$, h_c, or both , depending on the path, affected the performance of the LAS in estimating H.

3.4.4 Footprint analysis

We further studied the effect of applying the 3D footprint of the LAS on its estimates of H. For this part of the analysis we considered Path 3 as there were enough data to use (about 45 days). Generally, even though saturation effects have been corrected for (section 3.1), we noticed that most of the error in Path 3 (Fig. 3.7) appears to occur at values of H higher than about 200 W m^{-2}. This basically represents all estimates made during the day between 8:00–9:00 AM to 4:00–5:00 PM under unstable atmospheric conditions. The wind direction over Path 3 was analyzed for the 51 days of the data. Five preferential wind directions were found (Table 3.4) and the corresponding analysis dates grouped accordingly. The data needed for estimating the 3D footprint of the LAS were analyzed (e.g. L_{MO}, u_*) for each group of the five major wind direction where we found

that one footprint can be used to represent all the days in each of the these directions. The footprints were estimated and geo-referenced according to the wind direction. Examples of the LAS 3D footprint are shown with wind directions 180° and 360° measured clockwise from North (Fig. 3.8a–b).

It is clear that, based on the LAS 3D footprint and wind direction; the roughness parameters (e.g. h_c, d, and z_0) have different values (Table 3.4). Using these values we estimated the sensible heat flux, H_{Ftp}, for the selected days and provided the corresponding H_{LAS} and H_{LiD_PA}. An example of the LAS 3D footprint effects on the sensible heat flux estimates is shown for the two days in Fig. 3.8c–d that corresponds to the footprint and wind direction in Fig. 3.8a–b. It can clearly be seen the improvement in H_{Ftp} compared to both H_{LAS} and H_{LiD_PA}. During both dates, April 17th and April 20th, H_{LAS} considerably underestimated H_{BR} while both H_{LiD_PA} and H_{Ftp} showed good agreement with H_{BR}. For all 51 days, estimates of H_{LAS}, H_{LiD_PA}, and H_{Ftp} compared to H_{BR} are shown in Fig. 3.9. It indicates, on overall, better performance, by LAS estimates of H_{Ftp} when considering its footprints as supported by the statistics in Table 3.5. H_{Ftp} showed the lowest RMSE of 37 W m^{-2} compared to 54 and 42 W m^{-2} for H_{LAS} and H_{LiD_PA}, respectively. It also resulted in the lowest MAE of 29 W m^{-2}compared to 42 and 35 W m^{-2} for H_{LAS} and H_{LiD_PA}, respectively. Also H_{Ftp} provided less scattering around the 1:1 line compared to H_{LiD_PA} (Fig. 3.9).

The point we would like to raise from this exercise is that, generally, the scintillometer measures the intensity fluctuations due to turbulent eddies along its path without knowledge of its source or direction. The turbulence that passes through, and eventually measured by, the LAS path basically has the combined signature, depending

on the blending height, from the individual patches in the upwind footprint direction. It is therefore necessary to properly define the corresponding surface roughness parameters (i.e. h_c, d, and z_0). Also using the LAS weighting function to estimate the corresponding effective height z_{eff} is legitimized by the notion that it describes the weight of contribution of the scintillation measured by the propagating wave along its path (Andreas 1990). Using $W(u)$ to obtain a weighted average estimate for the corresponding roughness parameters could be a reasonable approximation in conditions with similar type of heterogeneity along and around the LAS path as in the case of Paths 1 and 2. This also suggests that a pre-analysis of wind direction, selection of the path, and investigation of the surface heterogeneity are important tasks to perform before setting up the scintillometer as it will define the need of using the LAS footprint approach in estimating the sensible heat flux.

3.5 Conclusions

In this study we investigated the effects of incorporating LiDAR-derived topography and surface roughness on the scintillometer-based estimates of sensible heat flux (H). The study was conducted over the Cibola National Wildlife Refuge in southern California. The region is characterized by arid to semi-arid conditions and considerable surface heterogeneity imposed by riparian vegetation which consists mostly of tamarisk trees and shrubs interspersed with bare soil. This setting provided interesting conditions to test the application of the scintillometer and its performance at. Two LASs were set in the area according to the variability of the surface roughness with Path 1, 2, and 3 having low, medium, high surface heterogeneity, respectively.

Large aperture scintillometer (LAS) measurements, specifically C_n^2, was used to estimate C_T^2 and ultimately H. The effect of using different representations of surface roughness and heterogeneity was investigated. First, H_{LAS} was estimated using topographic maps and vegetation survey to estimate LAS beam height $z(u)$ as well as and an average canopy height (h_c) around the center of the LAS path; secondly, H_{LiD_PA} estimated based on LiDAR-derived topographic and canopy height maps to estimate $z(u)$, h_c, d, z_0, along the LAS path. Estimates of H_{LAS} and H_{LiD_PA} were made over the three LASs settings Path 1, 2, and 3. The results indicated that incorporating LiDAR data into LAS-based estimates of H improved its performance. This improvement can be explained by the fact that either increased variability in topography and/or surface roughness that could be present along and around the LAS path, as in the case of Path 1 and 3, were well represented by the LiDAR data. On the other hand, if less variability exists in both topography and surface roughness, as in the case of Path 2, obviously less improvement results.

We also investigated the effects of representing surface roughness using the LAS 3D footprint on the estimates of H. Estimates of H_{Ftp} were provided using roughness parameter values (i.e. h_c, d, and z_0) determined from combining the LAS 3D footprint and LiDAR-derived canopy height maps as we considered only the case of Path 3. The results showed a considerable improvement in the sensible heat flux estimates as we compared H_{LAS}, H_{LiD_PA}, and H_{Ftp} with H_{BR}. These findings showed the importance of considering the 3D footprint of scintillometer analysis as well as using detailed surface roughness (e.g. LiDAR-derived surface features) over heterogeneous areas.

References

Andreas, E. L., 1988: Atmospheric stability from scintillation measurements. *Appl. Optics*, **27,** 2241–2246.

Andreas, E. L., 1989: Two-wavelength method of measuring path averaged turbulent surface heat fluxes. *J. Atmos. Oceanic Technol.* **6,** 280–292.

Andreas, E. L., 1990: Selected papers on turbulence in a refractive medium, SPIE Milestone Series 25, SPIE-The International Society for Optical Engineering, Bellingham, 693 pp.

Andreas, E. L., 1991: Using scintillation at two wavelengths to measure path averaged heat fluxes in free convection. *Bound.-Layer Meteor.* **54,** 167–182.

Baldocchi, D. D., B. B. Hicks, and T. P. Meyers, 1988: Measuring biosphere-atmosphere exchange of biologically related gases with micrometeorological methods. *Ecology,* **69(5),** 1331–1340.

Bowen, I. S., 1926: The ratio of heat losses by conduction and by evaporation from any water surface. *Phys. Rev.,* **27,** 779-787.

Brutsaert, W., 1982: *Evaporation into the Atmosphere: Theory, History, and Applications.* Springer, 299 pp.

Chatterjee, S., 2010: Estimating evapotranspiration using remote sensing: A hybrid approach between Modis derived enhancement vegetation index, Bowen ratio systems, and ground based micro-meteorological data. PhD thesis, Wright State University, 175 pp.

Chehbouni, A., C. Watts, J.-P. Lagouarde, Y. H. Kerr, J.-C. Rodriguez, J.-M. Bonnefond, F. Santiago, G. Dedieu, D. C. Goodrich, and C. Unkrich, 2000: Estimation of heat and momentum fluxes over complex terrain using a large aperture scintillometer. *Agric. Forest Meteor.*, **105,** 215–226.

Chehbouni, A., Y. H. Kerr, C. Watts, O. Hartogensis, D.C. Goodrich, R. Scott, J. Schieldge, K. Lee, W. J. Shuttleworth, G. Dedieu, and H.A.R. De Bruin, 1999: Estimation of area-average sensible heat flux using a large-aperture scintillometer during the Semi-Arid Land-Surface-Atmosphere (SALSA) experiment. *Water Resour. Res.*, **35**, 2505–2511.

De Bruin, H. A. R., 2002: Introduction: Renaissance of scintillometry. *Bound.-Layer Meteor.*, **105**, 1-4.

De Bruin, H. A. R., and O. K. Hartogensis, 2005a: Monin-Obukhov similarity functions of the structure parameter of temperature and turbulent kinetic energy dissipation rate in the stable boundary layer. *Bound.-Layer Meteor.*, **116,** 253–276.

De Bruin, H. A. R., B. J. J. M. van den Hurk, and W. Kohsiek, 1995: The scintillation method tested over a dry vineyard area. *Bound.-Layer Meteor.,* **76**, 25–40.

De Bruin, H. A. R., B. J. J. M. van den Hurk, and L. J. M. Kroon, 1999: On the Temperature-humidity correlation and similarity. *Bound.-Layer Meteor.,* **93**, 453–468.

De Bruin, H. A. R., O. K. Hartogensis, R. G. Allen, and J. W. J. L. Kramer, 2005b: Regional advection perturbations in an irrigated desert (RAPID) experiment. *Theor. Appl. Climatol.*, **80,** 143–152.

De Bruin, H. A. R., W. Kohsiek, and B. J. J. M. van den Hurk, 1993: A verification of some methods to determine the fluxes of momentum, sensible heat and water vapour using standard deviation and structure parameter of scalar meteorological quantities. *Bound.-Layer Meteor.*, **63**, 231–257.

De Wekker, S. F. J., 1996: The estimation of areally-averaged sensible heat flux over complex terrain with a large-aperture scintillometer. M.S. Thesis, Department of Meteorology, Wageningen Agricultural University, 42 pp.

Hartogensis, O. K., and H. A. R. De Bruin, 2005: Monin-Obukhov Similarity functions of the structure parameter of temperature and turbulent kinetic energy dissipation rate in the stable boundary layer, *Bound.-Layer Meteor*. **116,** 253–276.

Hartogensis, O. K., C. J. Watts, J. -C. Rodriguez, and H. A. R. De Bruin, 2003: Derivation of an effective height for scintillometers: La Poza experiment in northwest Mexico, *J. Hydrometeor*. **4,** 915–928.

Hill, R. J., and S. F. Clifford, 1978: Modified spectrum of atmospheric temperature flucuations and its applications to optical propagation. *J. Opt. Soc. Am.*, **68,** 892–899.

Hill, R. J., S. F. Clifford, and R. S. Lawrence, 1980: Refractive-index and absorption fluctuations in the infrared caused by temperature, humidity and pressure fluctuations, *J. Opt. Soc. Amer.*,**70,** 1192–1205.

Hoedjes, J. C. B., A. Chehbouni, J. Ezzahar, R. Escadafal, and H. A. R. De Bruin, 2007: Comparison of large aperture scintillometer and eddy covariance measurements: Can thermal infrared data be used to capture footprint-induced differences? *J. Hydrometeor*. **8,** 144–159.

Hoedjes, J. C. B., R. M. Zuurbier, and C. J. Watts, 2002: Large aperture scintillometer used over a homogeneous irrigated area, partly affected by regional advection. *Bound.-Layer Meteor.*, **105**, 99–117.

Horst, T. W., and J. C. Weil, 1992: Footprint estimation for scalar flux measurements in the atmospheric surface layer. *Bound.-Layer Meteor.*, **59,** 279–296.

Horst, T. W. and J. C. Weil, 1994: How far is far enough?: The fetch requirements for micrometeorological measurement of surface fluxes. *J. Atmos. Oceanic Technol.*, **11,** 1018–1025.

Kohsiek, W., W. M. Meijninger, H. A. R. De Bruin, and F. Beyrich, 2006: Saturation of the large aperture scintillometer. *Bound.-Layer Meteor.*, **121,** 111–126.

Massman, W. J., and X. Lee, 2002: Eddy covariance flux corrections and uncertainties in long term studies of carbon and energy exchanges. *Agric. Forest Meteor.,* **113,** 121–144.

Meijninger, W. M. L., F. Beyrich, A. Lüdi, W. Kohsiek, and H. A. R. De Bruin, 2006: Scintillometer-based turbulent fluxes of sensible and latent heat over a hetergenous land surface- a contribution to Liftass-2003., *Bound.-Layer Meteor.*, **121,** 89–110.

Meijninger, W. M. L., O. K. Hartogensis, W. Kohsiek, J. C. B. Hoedjes, R. M. Zuurbier, and H. A. R. De Bruin, 2002a: Determination of area-averaged sensible heat fluxes with a large aperture scintillometer over a heterogeneous surface—Flevoland field experiment. *Bound.-Layer Meteor.* **105,** 37–62.

Meijninger, W. M. L., O. K. Hartogensis, W. Kohsiek, J. C. B. Hoedjes, R. M. Zuurbier, and H. A. R. De Bruin, 2002b: Determination of area-averaged water vapor fluxes with a large aperture and radio wave scintillometer over a heterogeneous surface—Flevoland field experiment. *Bound.-Layer Meteor.* **105,** 63–82.

Moene, A. F., 2003: Effects of water vapour on the structure parameter of the refractive index for near-infrared radiation. *Bound.-Layer Meteor.*, **107,** 635–653.

Monteith, J. L. and M. H. Unsworth, 2008: *Principles of Environmental Physics*. Academic Press, 418 pp.

Panofsky, H. A., and J. A. Dutton, 1984: *Atmospheric Turbulence: Models and Methods for Engineering Applications.* John Wiley and Sons, 397 pp.

Schmid, K., K. Waters, L. Dingerson, B. Hadley, R. Mataosky, J. Carter, and J. Dare, 2008: Lidar 101: An Introduction Lidar Technology, Data, and Applications. National Oceanic and Atmospheric Administration (NOAA) Coastal Services Center, Charleston, SC, 68 pp.

Shuttleworth, W. J., Z.-L. Yang, M. A. Arain, 1997: Aggregation rules for surface parameters in global models. *Hydrol. Earth Syst. Sci.*, **1,** 217–226.

Tatarskii, V. I., 1961: *Wave Propagation in a Turbulent Medium*, translated from Russian by R. S. Siverman, McGraw-Hill, 285 pp.

USGS, 2010: United States Geological Survey, site visited December 2010, http:\\seamless.usgs.gov.

Wang, T. I., G. R. Ochs, and S. F. Clifford, 1978: A saturation resistant optical scintillometer to measure C^2_n. *J. Opt. Soc. Amer.,* **69,**334–338.

Wesely, M. L. 1976: The combined effect of temperature and humidity on the refractive index. *J. Appl. Meteor.*, **15,** 43–49.

Wood, N., and J.P. Mason, 1991: The influence of static stability on the effective roughness length for momentum and heat transfer, *Quart. J. Roy. Meteor. Soc.*, **117,** 1025–1056.

Wyngaard, J. C., Y. Izumi, and S. A. Collins Jr., 1971: Behavior of the refractive index structure parameter near the ground. *J. Opt. Soc. Amer.*, **15,** 1177–1188.

TABLE 3.1. Summary of performance statistics showing the different estimates of H compared with measurements for Path 1 with L_P = 1.8 km.

	RMSE ($W\ m^{-2}$)	MAE ($W\ m^{-2}$)	BIAS ($W\ m^{-2}$)	h_c (m)	z_0 (m)	z_{wt_ave} (m)
H_{LAS}	44	35	28	3.24	0.27	12.57
H_{LiD_PA}	34	27	11	3.19	0.26	10.97

TABLE 3.2. Summary of performance statistics showing the different estimates of H compared with measurements for Path 2 with L_P =1.0 km.

	RMSE ($W\ m^{-2}$)	MAE ($W\ m^{-2}$)	BIAS ($W\ m^{-2}$)	h_c (m)	z_0 (m)	z_{wt_ave} (m)
H_{LAS}	50	39	-27	3.95	0.32	6.44
H_{LiD_PA}	47	35	-6	3.35	0.27	6.46

TABLE 3.3. Summary of performance statistics showing the different estimates of H compared with measurements for Path 3 with L_P =1.6 km.

	RMSE ($W\ m^{-2}$)	MAE ($W\ m^{-2}$)	BIAS ($W\ m^{-2}$)	h_c (m)	z_0 (m)	z_{wt_ave} (m)
H_{LAS}	52	39	-20	1.27	0.10	5.11
H_{LiD_PA}	41	32	12	2.18	0.18	6.31

TABLE 3.4. Summary of performance statistics showing the different estimates of H compared with measurements for Path 3 with L_P =1.6 km.

	WD[1]	RMSE	MAE	BIAS	h_c	z_0	z_{wt_ave}
	(°)	(W m^{-2})	(W m^{-2})	(W m^{-2})	(m)	(m)	(m)
H_{LAS}	–	54	42	-37	1.27	0.10	5.11
H_{LiD_PA}	–	42	35	17	2.18	0.18	6.31
H_{FP}	120	37	29	2	1.57	0.13	6.31
	180				1.73	0.14	
	225				1.69	0.14	
	345				1.84	0.15	
	360				1.48	0.12	

[1]WD wind direction measured clockwise from the north direction.

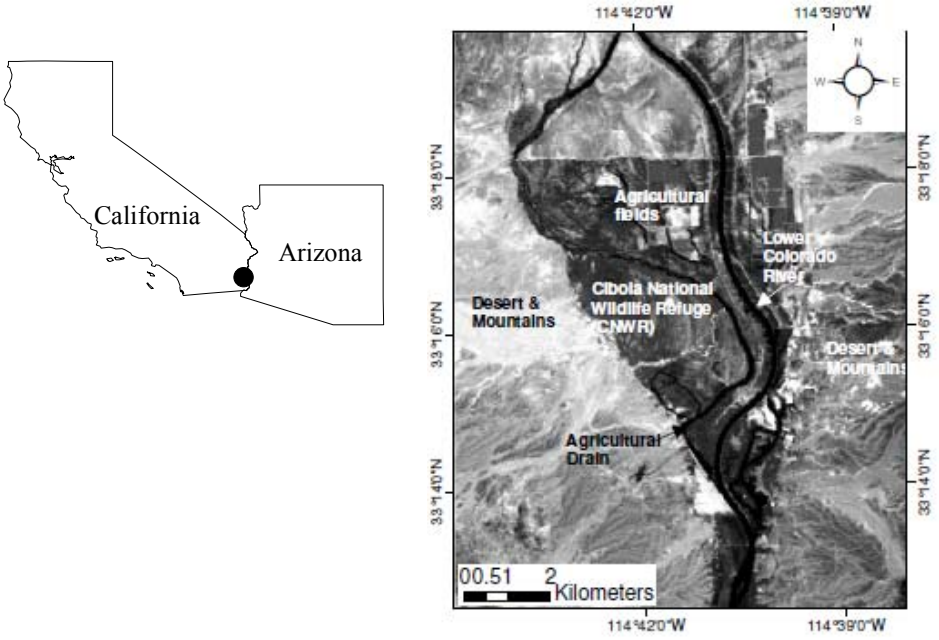

Fig. 3.1. Location map showing the study area, the Cibola National Wildlife Refuge (CNWR), surrounded by deserts and mountains, agricultural drain and the Lower Colorado River.

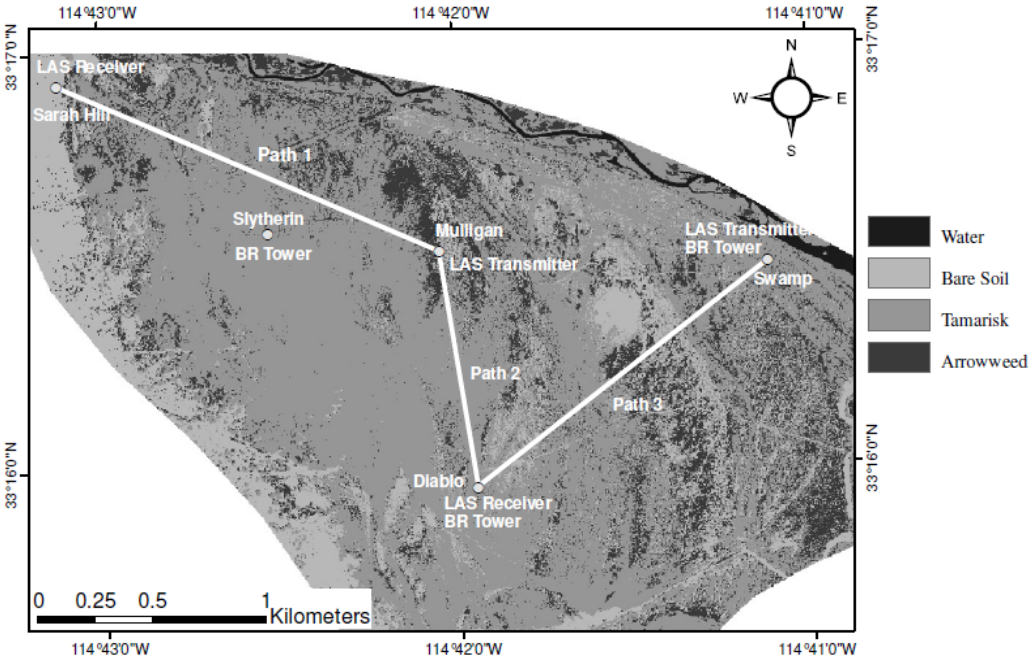

Fig. 3.2. Map showing the land cover in CNWR derived from 1-m spatial resolution airborne multispectral band imagery taken May 18th 2008.

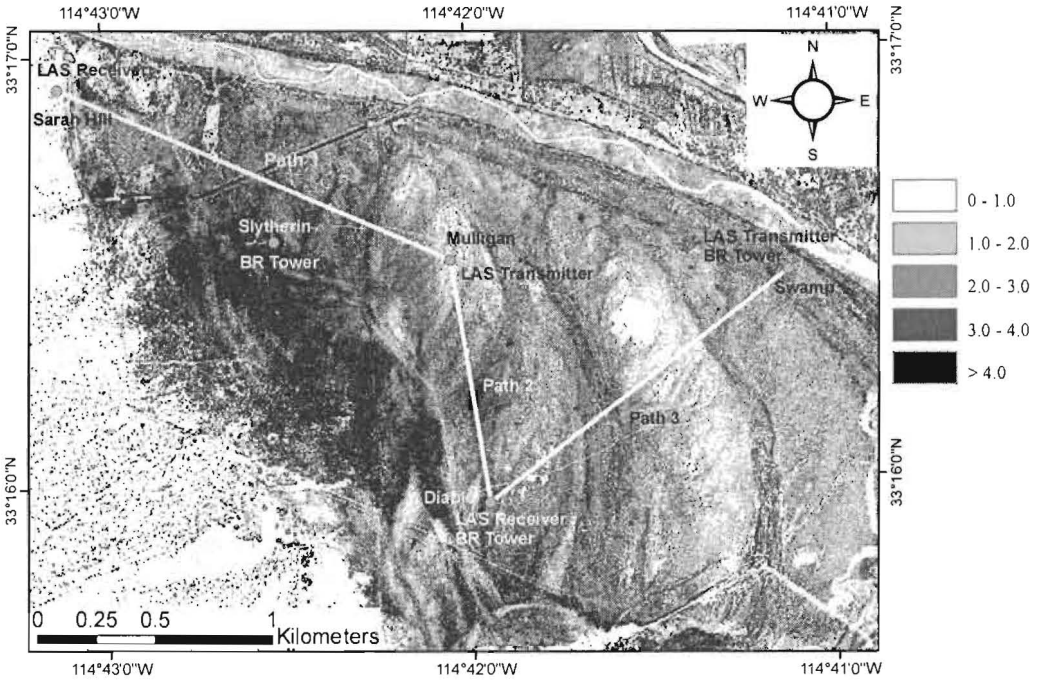

Fig. 3.3. Map of the LiDAR-derived canopy height (h_c) at 1-m spatial resolution acquired September 4th 2008.

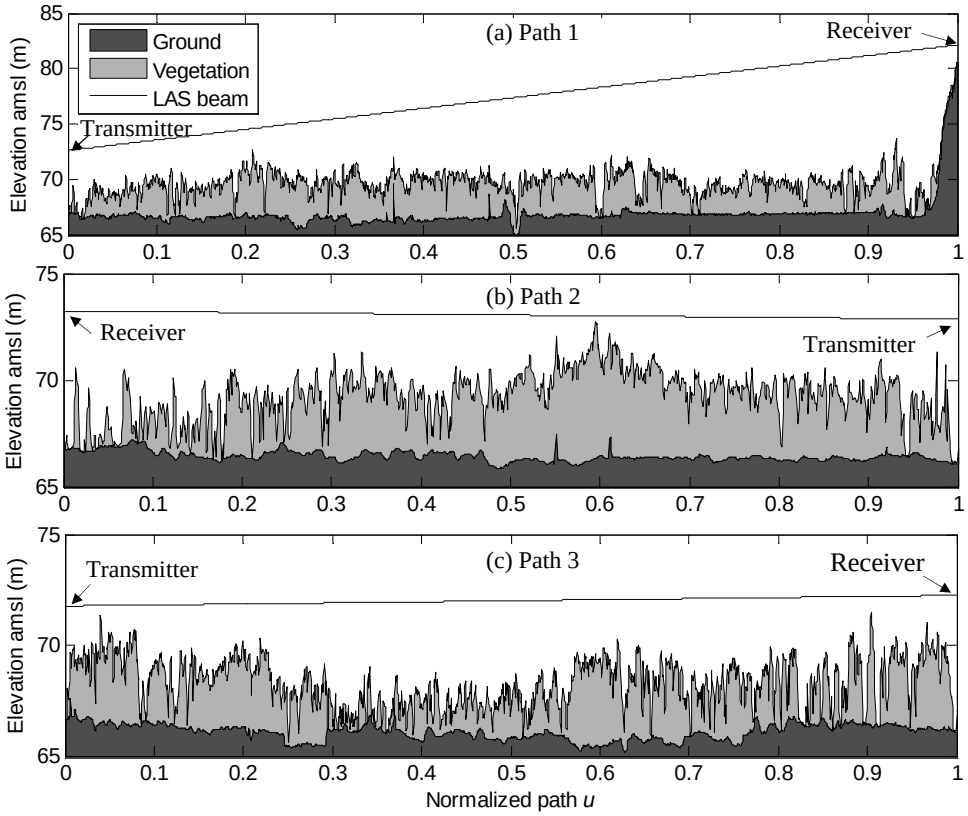

Fig. 3.4. LiDAR-derived canopy height (h_c) (light gray shade), ground surface (dark gray shade), and LAS beam (line) profiles above mean sea level (amsl) for a) Path 1, b) Path 2, and c) Path 3.

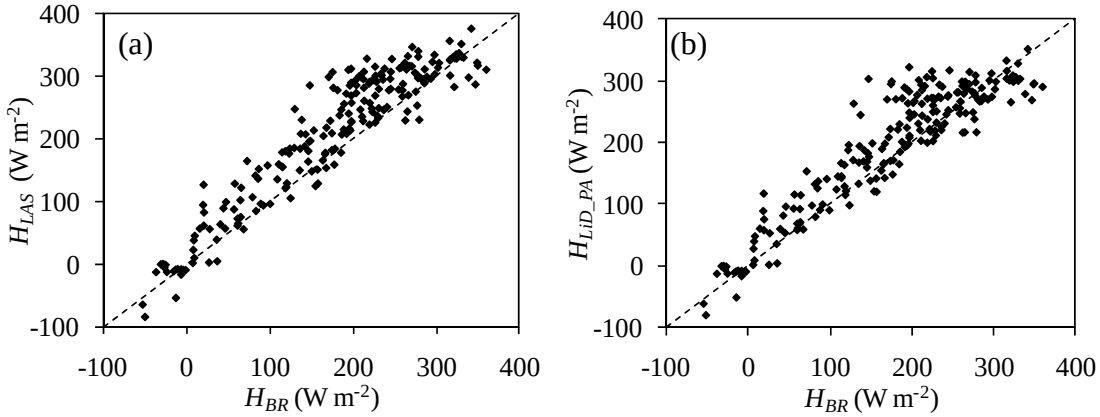

Fig. 3.5. Estimated a) H_{LAS} and b) H_{LiD_PA} based on surface roughness from traditional and LiDAR methods, respectively, compared with measured H_{BR} from Bowen ratio systems over Path 1.

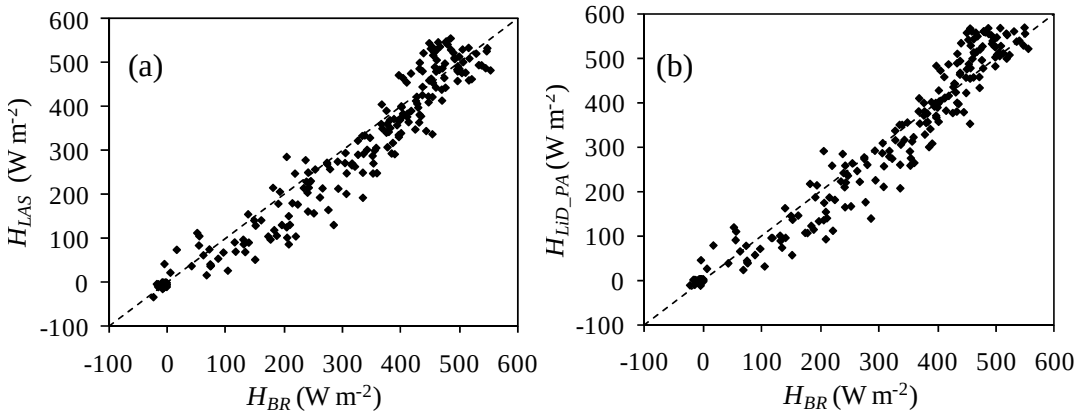

Fig. 3.6. Estimated a) H_{LAS} and b) H_{LiD_PA} based on surface roughness from traditional and LiDAR methods, respectively, compared with measured H_{BR} from Bowen ratio systems over Path 2.

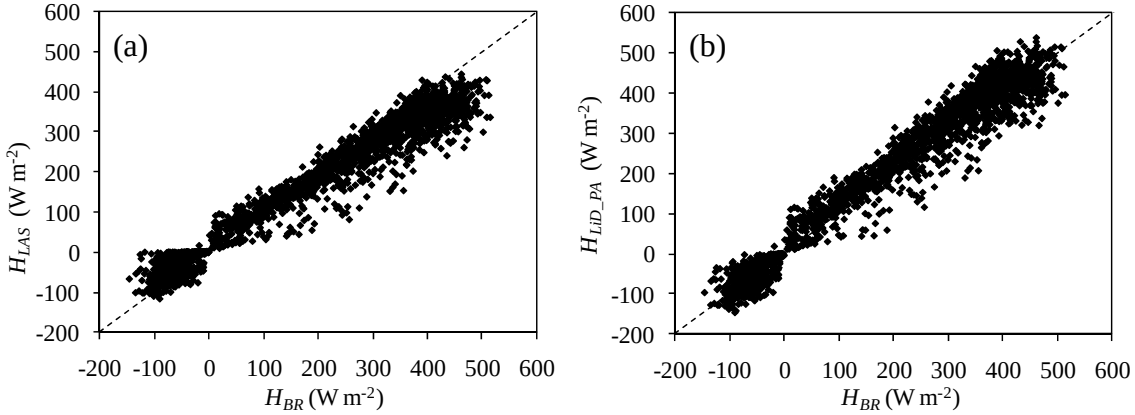

Fig. 3.7. Estimated a) H_{LAS} and b) H_{LiD_PA} based on surface roughness from traditional and LiDAR methods, respectively, compared with measured H_{BR} from Bowen ratio systems over Path 3.

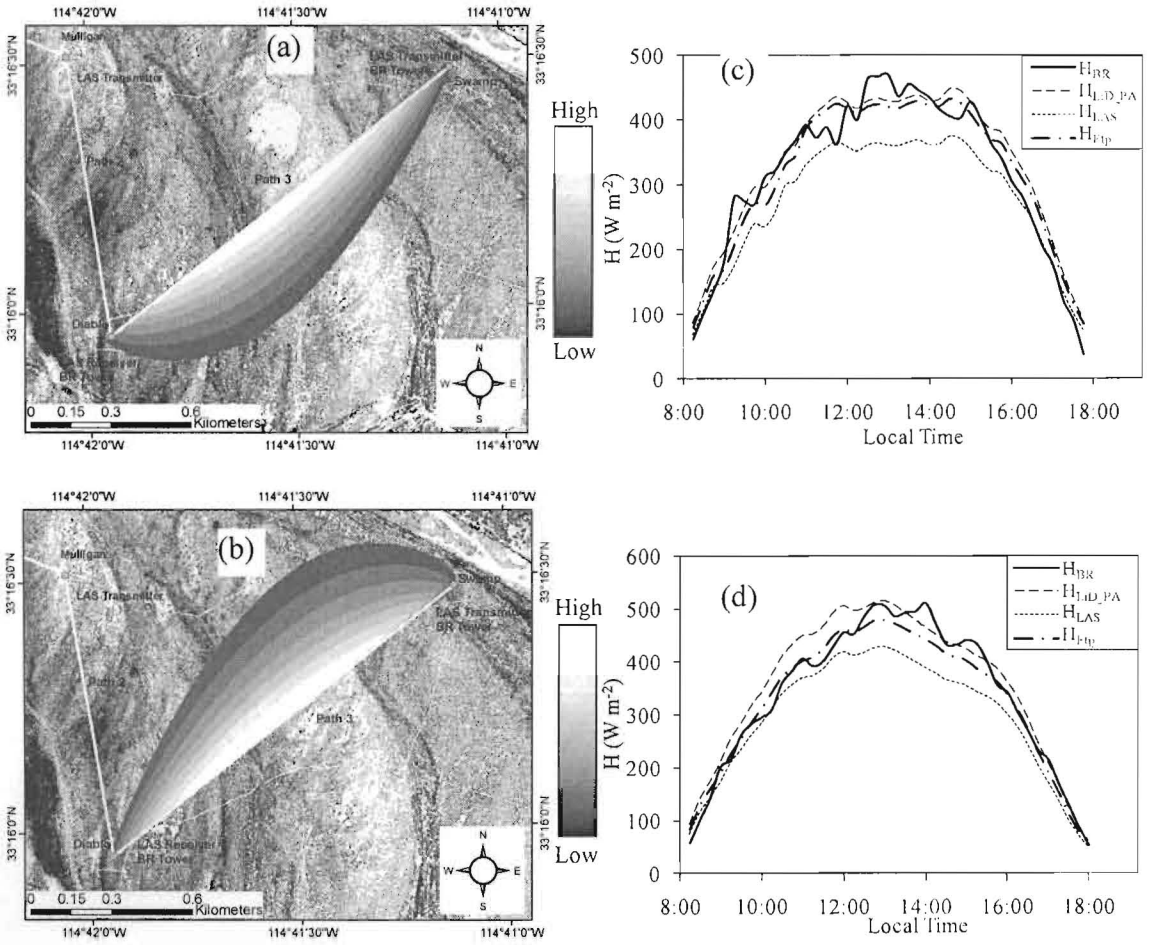

Fig. 3.8. LAS 3D footprint during a) April 20th and b) April 17th, 2008 geo-referenced according to wind direction, with gray scale from high (White) to low (Black) contribution, are overlaid with the LiDAR-derived canopy height (h_c). The corresponding timeseries plots of the estimated and measured H during c) April 20th and d) April 17th are shown over Path 3.

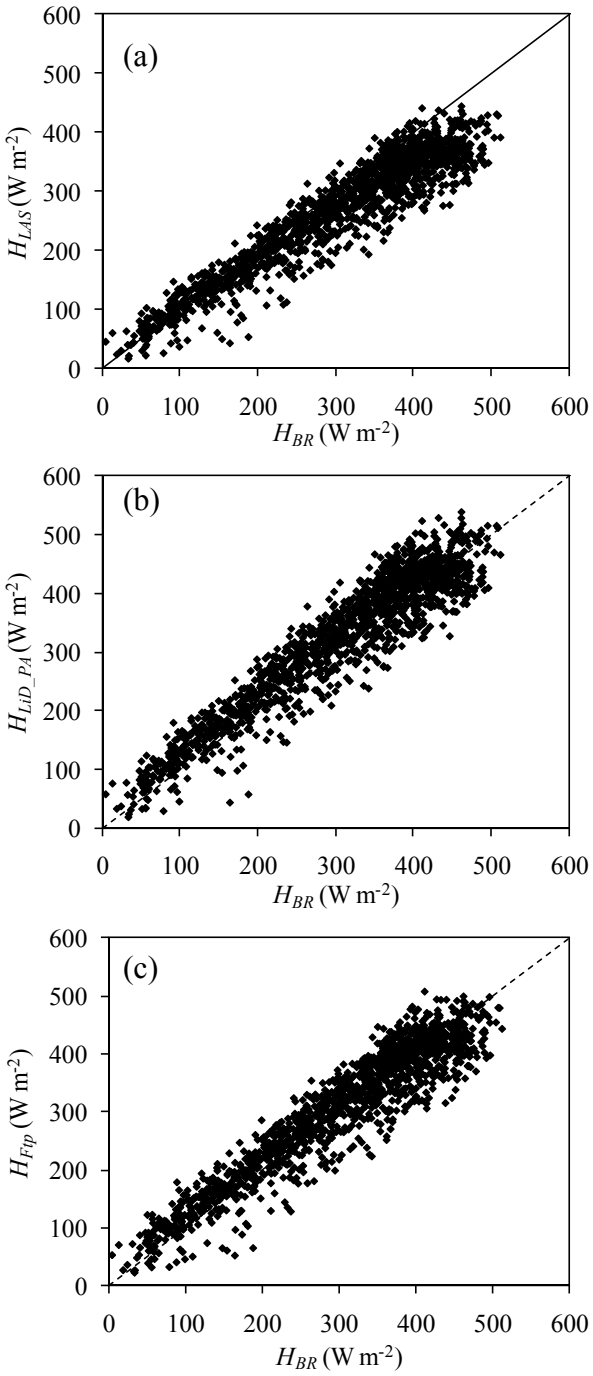

Fig. 3.9. Estimated a) H_{LAS} and b) H_{LiD_PA} , and c) H_{Ftp} based on surface roughness from traditional, LiDAR, and LiDAR with LAS 3d footprint methods, respectively, compared with measured H_{BR} from Bowen ratio systems over Path 3.

CHAPTER 4

EFFECTS OF SPATIAL HETEROGENEITY REPRESENTATION ON MODELING SURFACE ENERGY FLUXES AND EVAPOTRANSPIRATION[3]

Abstract

The effect of using different remote sensing representations of heterogeneous surface features on estimating surface energy balance fluxes (SEBF) and evapotranspiration (*ET*) was investigated. Airborne data provided surface features representation at spatial pixel resolution of 1-4 m and the Landsat 5 provided 30-60 m in the visible and thermal infrared electromagnetic multispectral wavebands. A vegetation height (h_c) map was obtained using Light Detection and Range (LiDAR) techniques. These data were collected over the Cibola National Wildlife Refuge (CNWR) southern California, during the summer of 2007-2008. The area is a riparian zone dominated with Tamarisk (Tamarix ramosissima) trees, Arrowweed (Pulchea sericea), Mesquite (Prosopis glandolusa) and other desert shrubs interspersed with bare soil which in turn provided unique, rather extreme, surface heterogeneity conditions.

Estimates of SEBF/*ET* were obtained using two theoretically different approaches; a thermal remote sensing based technique namely the two-source energy balance (TSEB) model and the traditional Matt-Shuttleworth (M-S) model–a reviewed version of the FAO-56 approach. Estimates of SEBF/*ET* from both models were compared with ground based measurements from Bowen ratio and large aperture scintillometers. Models performances as well as the associated model/measurements differences with respect to sub-pixel heterogeneity, canopy height, leaf area index, wind

[3] Co-authored by Hatim M. E. Geli, Christopher M. U. Neale, Lawrence E. Hipps, and Luis A. Bastidas

speed, and soil moisture conditions were discussed. Reasonable results were obtained at the airborne dataset pixel resolution indicating the appropriateness of using such scale in capturing extreme surface heterogeneity condition and in providing better representation of surface features.

4.1 Introduction

Spatial estimates of surface energy balance fluxes (SEBF) and evapotranspiration (*ET*) at different scales, with a reasonable accuracy, are increasingly valuable operational tools as they provide essential information for a wide range of applications and purposes such as characterizing land surface processes in climate, hydrometeorologic, and atmospheric modeling (Sellers et al. 1986; Humes et al. 2003); drought monitoring (Anderson et al. 2007a, 2007b); hydrological modeling (Houser et al. 1998; Meijerink et al. 2005); in agricultural studies for crop monitoring, water requirements and productivity (Moran et al. 1995; Kustas and Anderson 2009); monitoring ecosystem functioning over naturally vegetated (Moran 2004); and estimating water consumption by native and invasive plant species (Chavez 2005).

A suite of models exist in the literature that use remote sensing data at different spatial and temporal scales as input to provide estimates of SEBF/*ET*. However this wide range of spatial scales results in considerably different representations of the Earth's surface features due to either different sensor pixel resolution or bandwidth configurations. For example, Landsat Thematic Mapper 5/7 provide imagery at 30-m pixel resolution in the visible bands (VIS) and 60-m or 120-m in the Thermal Infrared (TIR) bands, while airborne systems can provide 1-m or less pixel resolution in all bands depending on the acquisition altitude. Over heterogeneous areas a Landsat pixel would

comprise multiple land cover/land use types that can be reduced individual vegetation types at the subpixel level using high spatial resolution such as those provided by airborne systems (Kustas et al. 2004). Consequently this would have effects on estimating some plant biophysical properties, such as the leaf area index (*LAI*) and the fraction of vegetation cover (f_c) (Moran et al. 1997), that are required in many applications and would eventually affect estimates of spatial SEBF/*ET* (Kustas and Norman 2000b; Li et al. 2008). Another biophysical parameter required for many applications including estimates of SEBF/*ET* is the canopy height h_c (see e.g. Chapter 3). This important surface feature can be obtained at highly accurate spatial and vertical resolution up to few centimeters using the technology known as Light Detection and Ranging (LiDAR). LiDAR systems consist of a sensor that emits a laser beam at high frequency– up to 150 kHz–and receives the reflected light estimating the range and position of the return providing a highly accurate representation of the Earth's surface and its features. It has been used here to provide enhanced h_c maps at 1-m pixel resolution. Moreover, radiometric surface temperatures (T_R), an important parameter used in remote sensing based energy balance models, is highly affected by the sensor spatial resolution especially over extremely heterogeneous surfaces, that could result in contrasting temperature values in some cases up to ~30° K such as with heterogenous surfaces in our study area.

4.1.1 Thermal remote sensing-based models

Numerous remote sensing-based models connected to soil-vegetation atmosphere transfer (SVAT) schemes can be used to provide estimates of spatial SEBF/*ET* (Crow et al. 2005; Kalma et al. 2008). Most of the remote sensing SVAT schemes, basically,

model surface energy exchange in the soil-vegetation atmosphere interface using thermal-infrared remote sensing, represented by the radiometric surface temperature (T_R), as the key boundary condition (Kustas and Anderson 2009) to estimate SEBF/*ET* in a diagnostic manner. These models provide instantaneous spatial estimates of SEBF including the latent heat flux (λE) which can be converted to equivalent values of *ET*.

Generally, there are two main schools that adopt remote sensing SVAT schemes; a one-source modeling approach assumes the surface as one homogenous entity to model and estimate SEBF/*ET* , with examples including the Surface Energy Balance Index (SEBI) by Menenti and Choudhury (1993), the Surface Energy Balance (SEBAL) developed by Bastiaanssen et al. (1998), and the Mapping EvapoTranspiration with Internalized Calibration (METRIC) described by Allen et al. (2007). The other school uses a two-source modeling approach that takes into account surface heterogeneity by modeling vegetation and bare soil components separately. Examples of such approach include the two-source energy balance (TSEB) model developed by Norman et al. (1995) and the Atmosphere-Land Exchange Inverse (ALEXI) (Anderson et al. 1997, 2007a). Because of the advantages and superior performance of the two-source approach over the one-source in heterogeneous areas, that has been enumerated and described in many studies including the work by Kustas and Anderson (2009), we opted to use the TSEB model of Norman et al. (1995), with its recent modifications Kustas and Norman (1999, 2000b), to perform the required analysis.

There have been some studies that have focused on the effect of surface heterogeneity on the modeled SEBF/*ET* (e.g. Norman et al. 2003; Kustas et al. 2003, 2004; Kustas and Anderson 2009) but from a different perspective than this study. Here

we present the associated effects of using different representations of surface features as directly obtained from remote sensing, with no aggregation or disaggregation schemes performed either for SEBF or T_R, in the modeling process. For example; Norman et al. (2003) provided estimates of spatial SEBF/*ET* at 24-m resolution disaggregated from 5-km SEBF estimates. They followed what's called as ALEXI/DisALEXI approach, where high temporal resolution data from GOES satellite at scale of 5-km to estimate SEBF/*ET* then disaggregated to 24-m estimates using data from airborne system. Their study was conducted using the Southern Great Plain 1997 dataset from Oklahoma over agricultural cropland (pasture, grassland, winter wheat, rangeland with average height of 0.25- 0.5 m). Note that ALEXI is originally based on the TSEB model of Norman et al. (1995). Their resulted disaggregated fluxes showed reasonable agreement compared to ground-based eddy covariance measurements. In another study Kustas et al. (2004) investigated on the effect of pixel resolution on modeled SEBF. They used imagery from Landsat 7 and 5 TIR band at pixel resolutions of 60-m and 120-m degraded to 240-m to represent a thermally sharpened MODIS imagery and to 960-m to represent nominal MODIS and AVHRR image resolution. More details on the thermal sharpening methodology can be found in Kustas et al. (2003). Their research was applied over agricultural fields in Iowa covered with soybeans and corn crops using data from the SMACEX project (Kustas et al. 2004). They found that at coarse resolution of 960-m there was a dramatic loss of information making it very difficult to discriminate λE over corn soybean fields, the main purpose of their study, but it was possible to obtain such information at 240-m resolution using the thermal sharpening approach of Kustas et al. (2003) for MODIS data. In a different study by Chavez et al. (2009) the TSEB model was applied over a fairly

homogeneous agricultural area covered mostly cotton crop in central Texas using airborne imagery at spatial resolutions of about 0.5-m in the visible and NIR and 1-m in the thermal band.

4.1.2 Traditional *ET* methods

Traditional methods can also be used to provide estimates of spatial *ET* if the necessary spatial input data are available. Herein estimates of *ET* based on these traditional methods will be referred to as crop evapotranspiration (ET_c). Examples of such methods may include, but are not limited to, (1) the Food and Agriculture Organization Paper 56 (herein referred to as FAO-56) approach described in Allen et al. (1998) which utilizes the crop coefficient (*Kc*), modified for the specific crop and local climatic conditions, as a multiplicative factor of a predefined reference crop evapotranspiration (ET_0), either grass or alfalfa, to estimate ET_c; (2) the recently developed Matt-Shuttleworth (M-S) method described by Shuttleworth (2006). Both methods base their theoretical background on the original Penman-Montieth (P-M) equation (see e.g. Shuttleworth 2006). However the M-S approach utilizes the P-M by incorporating surface and aerodynamic resistances $(r_s)_c$ and $(r_a)_c$, respectively, to directly estimate ET_c of the vegetated surface. Shuttleworth (2006) examined the FAO-56 approach for estimating ET_c and described in detail the inherent theoretical inconsistencies which can be summarized in: (1) the application requires weather data that are usually obtained at a standard height of 2 m agl while some crops have greater canopy heights; and (2) the improper representation of crop-to-crop differences by K_c which are not strictly dependent only on crop biophysical properties but also on ambient climate. Finally, the implicit assumption by the FAO-56 approach, when using P-M equation to estimate ET_0,

of using "preferred" crop resistance values that are generally valid for short averaging periods of 20 to 60 min but not for daily averaged values. Allen et al. (2006) tried to address some of these inconsistencies as they suggested reconciling the ET_0 estimate in FAO-56 to overcome the issue of the averaging period but it still leaves some of the associated inconsistencies. Shuttleworth (2006) revised the FAO-56 approach and introduced the blending height concept at which estimates of the aerodynamic resistance $(r_a)_c$ and the vapor pressure deficit (D) are required, estimated from surface canopy height (h_c). They also described an alternative method for estimating surface resistance $(r_s)_c$ for each canopy type emulating the values of K_c in Allen et al. (1998). Shuttleworth and Wallace (2009) tested this approach over homogenous irrigated cropland areas in Australia with reasonable results.

Considering these recent revisions to the FAO-56 approach by Shuttleworth (2006) and its dependency on h_c we opted to apply the M-S approach, in addition to the TSEB model, to estimate *ET*, taking advantage of the LiDAR-based spatially distributed h_c values to estimate $(r_s)_c$ and $(r_a)_c$. This is different from the work by Mu et al. (2007) in which the original P-M equation was used and supported with remote sensing data, basically MODIS products, to provide spatial estimates of *ET* globally. In their study, surface and aerodynamic resistances were derived using remote sensing-based empirical models.

4.1.3 Objectives

The focus of this paper is to study the effects of representing the spatial variability of surface features heterogeneity on modeling SEBF/*ET* within the soil-vegetation-atmosphere interface. Two different modeling approaches namely the TSEB and the M-S

were compared by estimating spatial SEBF/*ET* using data and imagery obtained from different sensors including Landsat 5, the USU airborne multispectral digital system, and LiDAR-derived enhanced h_c maps. The analysis was carried out over a mixed riparian forest dominated by Tamarisk (Tamarix ramosissima) next to the Colorado River at the Cibola National Wildlife Refuge. The high spatial resolution of the airborne imagery should allow the characterization of sub-pixel heterogeneity in the radiometric surface temperature, T_R. This has been an issue that led to significant error in model estimates of SEBF as indicated in Kustas and Norman (2000a). The differences between the TSEB model estimates and flux measurements were analyzed under varying h_c, *LAI*, and wind speed, u. These findings will hopefully improve estimates of water consumption by this invasive species while conducting estimates of SEBF from multiple sensors such as the experiment by Anderson et al. (2011) on data fusion.

4.2 Methods

4.2.1 The two-source energy balance model (TSEB)

The TSEB model of Norman et al. (1995) with the series resistance formulation, originally based on the resistance formulation described by Shuttleworth and Wallace (1985), was used to provide estimate of spatial SEBF/*ET*. This model has been extensively reviewed in different aspects, as shown later, to improve its performance over wide range of climatic regions and surface heterogeneity conditions.

The TSEB model treats surface features; bare soil and vegetation canopy components, separately and applies the corresponding energy balance equation for each. An “air-canopy” interface is then introduced at some level above the ground, to achieve

the soil-vegetation interaction. At this level the associated SEBF from each component are combined in a series resistance form to represent the total of these fluxes.

The model uses the radiometric surface temperature, T_R, as the main boundary condition. It decomposes T_R by applying Eq. (1) into soil and canopy surface temperatures components, T_s and T_c, respectively (Norman et al. 1995) as

$$T_R(\phi) \approx \left[f_c(\phi) T_c^4 + (1 - f_c(\phi)) T_s^4 \right]^{1/4} \tag{1}$$

where $f_c(\phi)$ is the fraction of vegetation cover at the radiometer view angle, ϕ, and can be estimated as

$$f_c(\phi) = 1 - \exp\left(\frac{-0.5 \Omega LAI}{\cos(\phi)} \right) \tag{2}$$

where Ω is the clumping factor estimated as a function of ϕ, and LAI the leaf area index. For detailed description on estimating Ω refer to Kustas and Norman (2000b).

Norman et al. (1995) initially used an empirical exponential model to estimate the net radiation (Rn) for the soil and canopy components (Rn_s) and (Rn_c), respectively. A recently revised version of the TSEB (Kustas and Norman 2000b; Li et al. 2005) introduced the use of a physically based model developed by Campbell and Norman (1998) for better estimation of Rn_s and Rn_c as

$$Rn_c = Ln_c + (1 - \tau_s)(1 - \alpha_c) S \tag{3}$$

$$Rn_s = Ln_s + \tau_s (1 - \alpha_s) S \tag{4}$$

where Ln_c and Ln_s are the longwave radiation of the canopy and soil components, respectively, estimated using Eqs. (5)–(6), α_s the soil albedo, α_c the canopy albedo, τ_s the solar transmittance in the canopy, and S the incoming solar radiation.

$$Ln_c = \left[1 - \exp(-k_L \Omega LAI) \right] \left[L_{sky} + L_c + L_s \right] \tag{5}$$

$$Ln_s = \exp(-k_L \Omega LAI) L_{sky} + [1 - \exp(-k_L \Omega LAI)] L_c + L_s \quad (6)$$

where k_L is extinction coefficient, L_{sky}, L_c, and L_s the longwave radiation from the sky, canopy, and soil, calculated based on air, canopy, and soil temperatures, respectively, and Ω here estimated as a function of the sun zenith angle.

The effect of vegetation clumping is also considered when estimating the soil and canopy resistances, R_s and R_x appears in Eqs. (9) and (10), respectively. This specifically appears in the estimation of the extinction coefficients, a_s and a_x of the corresponding wind speeds for R_s and R_x as they can be estimated using Eqs. (7a) and (7b), respectively (Kustas and Norman 2000b).

$$a_s = 0.28(\Omega(\phi) LAI)^{2/3} h_c^{1/3} w_c^{-1/3} \quad (7a)$$

$$a_x = 0.28(\Omega(\phi) LAI_L)^{2/3} h_c^{1/3} w_c^{-1/3} \quad (7b)$$

where w_c the mean canopy leaf width, and LAI_L the local leaf area index.

The sensible heat flux, H, is estimated as $H = H_c + H_s$ with H_c and H_s the canopy and soil components of H, respectively, as

$$H = \rho C_p \frac{T_{ac} - T_a}{R_a} \quad (8)$$

$$H_s = \rho C_p \frac{T_s - T_a}{R_s} \quad (9)$$

$$H_c = \rho C_p \frac{T_c - T_{ac}}{R_x} \quad (10)$$

where T_{ac} is the air temperature at the air-canopy interface, ρ the air density taken as 1.24 (kg m^{-3}), C_p the specific heat of air taken as 1005 (J kg^{-1} K^{-1}), and R_a the aerodynamic resistance to heat transfer estimated as

$$R_a = \frac{\left[\ln\left(\frac{z_t - d_o}{z_{om}}\right) - \psi_H\right]}{ku^*} \quad (11)$$

where z_t is the measurement height for wind speed and air temperature, respectively, d_o the displacement height estimated as d_o = (2/3) h_c , z_{om} the roughness length for momentum taken as z_{om} = (1/8) h_c, ψ_H and the stability correction factor for atmospheric heat (Brutsaert 1982), R_x the total boundary layer resistance of the complete canopy leaves estimated using the formulation described by Norman et al. (1995), and R_s the resistance to heat flow in the boundary layer immediately above the soil surface estimated using Eq. 17 (Norman et al. 1995).

$$R_s = \frac{1}{a + bu_s} \quad (12)$$

where a and b are constants equals to 0.004 and 0.012, respectively, and u_s the wind speed at height above the soil surface where the effect of soil surface roughness is minimal and can be estimated using following Norman et al. (1995). Kustas and Norman (1999, 2000b) revised Eq. (12) by updating R_s through the knowledge of T_s and T_c in which a=0.004 replaced by c $(T_s\text{-}T_c)^{(1/3)}$, where c = 0.0025,

The latent heat flux, λE, is estimated as $\lambda E = \lambda E_c + \lambda E_s$, where λE_c and λE_s are the corresponding canopy and soil components, respectively. The model started with an initial estimate of λE_c using Priestly-Taylor formulation (Norman et al. 1995) as $\lambda E_c = \alpha_{PT} f_G [\Delta/(\Delta+\gamma)] Rn_c$,where α_{PT} is the Priestly-Taylor constant taken as 1.26, f_G the fraction of LAI that is green (f_G =1), Δ the slope of the saturation vapor pressure versus temperature curve, and γ the psychrometric constant. For stressed vegetation condition an iterative process typically results where the Priestly-Taylor (PT) constant =

1.26 produces a non-physical solution (such as λE_s <0, condensation on soil surface during daytime convective conditions) which then forces the PT to be reduced until a physical solution is obtained.

The soil heat flux, *G*, is estimated as $G = C_g Rn_s$, where C_g diurnally changes throughout the day and an average value of 0.30 can be used during the day time hours (Kustas et al. 1998b).

4.2.2 Matt-Shuttleworth Method

The Matt-Shuttleworth (M-S) method was used in this study to provide estimates of *ET* spatially. The M-S method is a one-step approach developed by Shuttleworth (2006) after reviewing the associated inconsistency in using the P-M equation (Monthieth 1965) in the FAO-56 approach of Allen et al. (1998). It is based on the P-M equation (Eq. 13) as the underlying model for estimating crop *ET* (ET_c) fortified with two main ideas. First it introduced the use of a blending height at some level above the ground within the atmospheric boundary layer. At this blending height the corresponding aerodynamic resistance $(r_a)_c$ need to be estimated considering the fact that meteorological variables such as wind speed (*U*) and vapor pressure deficit *D* are the same regardless of the underlying type of vegetation (Shuttleworth 2006). In addition, Shuttleworth (2006) provided a methodology to estimate crop-specific $(r_s)_c$ bending on the use of the available crop coefficient K_c^{FAO} tabulated values by Allen et al. (1998) since there is no equivalent $(r_s)_c$ values available as they called for the need for field studies.

The P-M equation can be described as

$$ET_c = \frac{\Delta(Rn - G) + (\rho c_P D_2 / (r_a)_c)}{\Delta + \gamma(1 + (r_s)_c / (r_a)_c)} \tag{13}$$

where D_2 is the vapor pressure deficit at 2 m agl. By introducing the blending height concept, the aerodynamic resistance $(r_s)_c$ at some height Z can be estimated as

$$(ra)_c^Z = \frac{R_c^Z}{u_2} \tag{14}$$

where R_c^Z is a parameter which can be estimated as

$$R_c^Z = \frac{1}{(0.41)^2}\ln\left[\frac{(Z-0.67h_c)}{(0.123h_c)}\right]\times\ln\left[\frac{(Z-0.67h_c)}{(0.123h_c)}\right]\frac{\ln\left[\frac{(2-0.08)}{0.0148}\right]}{\ln\left[\frac{(Z-0.08)}{0.0148}\right]} \tag{15}$$

Combining Eqs. (13-15) and assuming a blending height Z= 50 m ET_c can be estimated as

$$ET_c = \frac{\Delta(R_n - G) + \left(\frac{\rho c_P D_2}{R_c^{50}}\right)\left(\frac{D_{50}}{D_2}\right)}{\Delta + \gamma\left(1 + \frac{(r_s)_c u_2}{R_c^{50}}\right)} \tag{16}$$

where D_{50} is the vapor pressure deficit at 50 m agl and the ratio (D_{50}/D_2) can be estimated as

$$\left(\frac{D_{50}}{D_2}\right) = \left[\frac{(\Delta+\gamma)302 + 70\gamma u_2}{(\Delta+\gamma)208 + 70\gamma u_2}\right] + \left[\frac{\Delta(R_n - G)_c}{f_c \rho c_P D_2}\right]\times$$

$$\left[\left(\frac{(\Delta+\gamma)302 + 70\gamma u_2}{(\Delta+\gamma)208 + 70\gamma u_2}\right)\left(\frac{208}{u_2}\right) - \frac{302}{u_2}\right] \tag{17}$$

where f_c represents the ratio of radiant energy between the crop and the reference crop as $f_c = (R_n - G)_c / (R_n - G)_0$.

The surface resistance, $(r_s)_c$, can be estimated as a function of K_c^{FAO} as

$$(r_s)_c = \frac{r_s^1}{K_c^{FAO}} - r_s^2 \tag{18}$$

where

$$r_s^1 = \left(\frac{\frac{R_c^{50}}{u_2} + \left(\frac{D_{50}}{D_2}\right)^{pref} (r_{c\lim})^{pref}}{\frac{302}{u_2} + \left(\frac{D_{50}}{D_2}\right)^{pref} (r_{c\lim})^{pref}} \right) \times \left(\frac{\left(\Delta^{pref} + \gamma\right)\frac{302}{u_2} + 70\gamma}{\gamma} \right) \quad (19)$$

and

$$r_s^2 = \frac{\left(\Delta^{pref} + \gamma\right)}{\gamma} \frac{R_c^{50}}{u_2} \quad (20)$$

4.2.3 Leaf area index, canopy height, and fraction of cover

The *LAI* was estimated using Eq. (21) developed by Chavez (2005) based on data acquired in a riparian Tamarisk forest at the Bosque del Apache in the middle Rio Grande River. The fraction of cover (f_c) was estimated based on an empirical equation (Eq. 22) described by Nagler et al. (2003) developed based on data from the same study area CNWR.

$$LAI = 0.5781 \exp(2.9455 NDVI) \quad (21)$$

$$f_c = 1.72 NDVI - 0.15 \quad (22)$$

4.2.4 Flux footprints

Energy balance flux measurements obtained, for example, by Bowen ratio or eddy covariance towers represent a weighted integral contribution from the upwind direction area called the source area (SA) or footprint. Different footprint models have been suggested in literature such as those described by Schmid (1995) and by Horst and Weil (1992). They provide estimates of weights of the flux contribution within the upwind SA from which flux measurements are integrated. Most of these models provide

approximately 90 % of the total SA that contributes to the measured fluxes. In the current study, flux footprints were utilized to integrate estimates of spatial SEBF/*ET* to be compared with eddy covariance flux tower measurements for evaluation. Here we opted to use the model described by Horst and Weil (1992, 1994) that is based on the analytical solution of the advective-diffusion equation.

Horst and Weil (1992) described that the footprint function *f* relates the vertical turbulence flux measurements $F(x,y,z_m)$ at height z_m to the spatial distribution of the surface fluxes $F_0(x', y', z' = 0)$ as

$$F(x, y, z_m) = \int_{-\infty}^{\infty} \int_{-\infty}^{x} F_0(x', y', z' = 0) f(x - x', y - y', z_m) dx' dy' \tag{23}$$

with *x* and *y* represent the upwind the crosswind distance from the point of measurement. The footprint $\bar{f}^y$ function can be approximated by (Horst and Weil 1994)

$$\bar{f}^y(x, z_m) \cong \frac{d\bar{z}}{dx} \frac{z_m}{\bar{z}^2} \frac{\bar{u}(z_m)}{\bar{u}(c\bar{z})} A \exp[-z_m / b\bar{z}]^r \tag{24}$$

where z_m is the measurement height, $\bar{z}$ the mean plume height for diffusion from a surface source, and $\bar{u}(z)$ the mean wind speed. Coefficients *A*, *b*, and *c* are functions of the gamma function,Γ, and *r* the Gaussian plume model shape parameter (see Horst and Weil 1992).

4.2.5 Evaluation approach

The TSEB model was applied using both airborne and Landsat 5 multispectral imagery to provide instantaneous estimates of SEBF/*ET*. The airborne images were used along with the LiDAR-derived h_c map at 1-m horizontal spatial resolution and approximately 0.3 m vertical resolution. The Landsat images were used along with the

LiDAR-derived h_c map that was aggregated to 30-m spatial resolution using a simple averaging method, to match the spatial resolution of the Landsat TM imagery. The M-S model was applied to directly provide estimates of spatial daily *ET* using the LiDAR-derived h_c map at 1-m and the aggregated 30-m resolution map. This provided a way to study the effect of using different spatial resolution on remotely sensed estimated SEBF/*ET* as well as using a traditional method for estimating *ET*.

The spatial estimates of SEBF/*ET* from the TSEB and M-S models were compared with ground-based Bowen ratio (BR) measured fluxes over the appropriate footprints. The size and shape of the flux footprints were identified using Horst and Weil (1992, 1994) and geo-referenced to the specified BR tower location (see section 2d). Comparison of estimates with measurements was then performed by integrating the spatially estimated fluxes from the remotely sensed imagery using the footprint weights. We also took advantage of the available scintillometer data which had provided area-average measurements of *H* as to be compared with the spatial estimates of *H* from the TSEB.

The estimated instantaneous *ET* from the TSEB model was extrapolated to equivalent daily values using the evaporative fraction (*EF*) method described in Chavez et al. (2008). *EF*, which represents the ratio between instantaneous values of λE_i to the available energy $(Rn\text{-}G)_i$, is assumed to be constant throughout the day. The corresponding *EF* is multiplied by the daily available energy $(Rn\text{-}G)_d$ to provide daily *ET* estimates.

Model performance was evaluated using the root mean square error (RMSE), the mean absolute error (MAE), and the mean error (ME).

4.3 Data

4.3.1 Study area

The study was conducted at the Cibola National Wildlife Refuge (CNWR) in southern California during the summer of 2007-2008 in an arid to semi-arid climatic region with annual rainfall of less than 100 mm. The area, ≈ 5×4 km^2 centered at 114° 41' W 33° 16' N, is the floodplain of the Colorado river, surrounded by desert and bordered from the north by the main outflow drain from the Palo Verde Irrigation District (PVID), and the Colorado River to the east and south sides (Fig. 4.1). This riparian zone is approximately 90% covered with with a Saltcedar (Tamarix ramosissima) forest with varying density and a mixture of native trees and shrubs including Arrowweed, and Mesquite interspersed with bare soil (Fig. 4.2). Because of the need to improve water allocation and management of the Colorado River, the PVID area a long term study was initiated and funded by the US Bureau of Reclamation during the period 2006-2011. The data used herein were acquired during the study. The phenology of tamarisk at the CNWR, initiates with greenup in early march reaching full cover in late May-early June, with senescence beginning late September and total leaf loss by early December. Hence our measurements occurred during the full cover period of the tamarisk and will be described later in more details and supported by leaf area index estimates.

4.3.2 Micrometeorological measurements

Three Bowen Ratio (BR) systems were deployed in the area to provide basic micrometeorological observations along with the SEBF including net radiation (*Rn*), latent heat flux (*LE*), soil heat flux (*G*), and sensible heat flux (*H*). The BR system

developed by Radiation and Energy Balance Inc. (REBS) Seattle, USA, includes an automatic exchange mechanism (AEM). This mechanism basically reduces the measurement biases in the temperature and relative humidity gradients by switching the positions of the upper and the lower sensors every 15 minutes. Chapter 3 provided a detailed description of the BR instrumentation and data processing. The three BR towers were distributed within the CNWR taking into account spatial heterogeneity and density of the vegetation. The Slytherin BR tower was located within the highest density of Tamarisk with canopy heights of up to 5.5 m and instruments at 7.3 m above the ground surface. The Diablo BR tower instrumentation was at a height of 6.8 m within medium density trees with average heights of ≈ 4.0 m. The Swamp BR tower had the instrumentation at 5.5 above ground level downwind from a mixture of tamarisk trees and arroweed shrubs with average height of ~ 2 m interspersed with bare soil (Chapter 3). One of the issues with the use of the BR method is that it assumes that the sources of *LE* and *H* are the same which means that the exchange coefficients for heat and water vapor are equal i.e. K_h=K_e (see e.g. Baldocchi et al. 1988). This assumption is not always valid and applicable such as over tall heterogeneous vegetation. The validity of this assumption and its effect on the BR measurements will be discussed in more detail in the results and discussion section.

Two large aperture scintillometers (LAS) were used to provide area-averaged measurements of *H*. The LASs were Boundary Layer Scintillometer BLS900 from Scintec AG Rottenburg, Germany, with aperture diameter D =0.15 m operating at a wavelength of 880 nm. These measurements were processed and improvements made to consider the effect of surface heterogeneity and roughness as described by Geli et al.

(2011). These area-averaged measurements of *H* were available only for the summer of 2008. Similarly to the distribution of the BRs, the LASs were deployed and distributed in the area based on the spatial heterogeneity (Fig. 4.3). These measurements provided another way of verifying our model spatial estimates, similar to the approach used in other studies (Kleissl et al. 2009).

4.3.3 Remote sensing data

Airborne imagery was acquired using the USU airborne multispectral digital system operated by the Remote Sensing Services Laboratory (RSSL) at Utah State University (USU). The system consists of Kodak Megaplus 4.2i cameras filtered to form spectral bands in the green, red and near-infrared, similar to the Landsat Thematic Mapper bands TM2, TM3 and TM4, respectively (Neale and Crowther 1994; Chavez 2005). An Inframetrics 760 camera provided thermal infrared radiance imagery used to obtain radiometric surface temperature. The airborne system is mounted in a Cessna TP206 aircraft dedicated to remote sensing.

All, airborne and Landsat 5 images were atmospherically corrected using an atmospheric radiative transfer model called MODTRAN (Berk et al. 1989) resulting in surface reflectance and radiometric temperature images including the surface emissivity effects following the approach described by Li et al. (2004).

A set of 4 airborne image mosaics were processed that coincided with Landsat 5 Thematic Mapper overpass dates namely June 9th and 16th in 2007 (DOY 160 and 167 respectively) and May 10th and 17th in 2008 (DOY 131 and 138, respectively). Detailed information about the images, time of acquisition, and spatial resolution is shown in Table 4.1 and 4.2. The Landsat TM images were provided by the U.S. Geological Survey

EROS datacenter at 30-m for shortwave bands and 60-m pixel resolution for the TIR band. The TIR band was originally at 120 m resolution and was bi-linearly processed based on the associated visible bands to provide the higher resolution versions (see e.g. Li et al. 2008).

Airborne LiDAR data were collected on September 4th, 2008 using the Lidar-Assisted Stereo Imager (LASSI) developed at USU. This system, which consists of a full-waveform Riegl Q560 lidar transceiver, a Novatel SPAN LN-200 GPS/IMU Navigation System, was also mounted in the Cessna aircraft. The LiDAR was flown at ≈ 600 m agl and provided geo-referenced point cloud data at an average point density of over 2 points per square meter. The absolute point accuracy was approximately 7 cm and relative accuracy was approximately 2 cm. The point cloud data were classified into ground and vegetation returns and processed to obtain 1-m digital elevation models and vegetation height map as shown in Fig. 4.3.

4.4 Results and discussion

Before presenting the results it is appropriate to address issues related to the use of BR measurements over extremely heterogeneous surfaces such as the CNWR. Note that several studies by Kohseik et al. (2007) , Kustas et al. (1998a) and others indicated that the Q7 net radiometer used here generally tends to underestimate *Rn*. Kohseik et al. (2007) showed it underestimated *Rn* by ~ 5% while Kustas et al. (1998a) found it > 5%. Unfortunately, we didn't have data from a cross-calibration experiment to ascertain any potential errors in our experiment. An underestimation of *Rn* by any amount, if considered, would ultimately result in underestimation of λE and overestimation of H measurements with the error distributed between H and λE based on the value of the

Bowen ratio ($H/\lambda E$). Also the main underlying assumption of the Bowen ratio method is that the sources of the H and λE are the same meaning that $K_h=K_e$, with K_h and K_e representing the exchange coefficients for heat and water vapor, respectively. This assumption leads us to conclude that the BR is not the preferred method for providing flux measurements over heterogeneous areas that could have variations in sources and sinks for heat, vapor, and momentum. In addition, BR systems can have problems in measuring small values of gradient of temperature (T) and specific humidity (q), which generally occur in semi-arid environments over tall forests similar to CNWR. However, Tamarisk is a phreatophyte tree and has high evaporation rates as supported by sap flow measurements conducted at CNWR and other areas in the US (Nagler et al. 2003). This would enhance gradients of both T and q hence reducing the possible error in the ET estimates due to this issue. Moreover, the average LAI at the CNWR riparian forest ranged between 2.0 at Swamp to 4.0 at Slytherin, indicating relatively dense vegetation conditions. Therefore, assuming a similar value of d for heat and momentum flux transfers for these BR measurements might not result in significant error allowing the results to be used for model verification.

4.4.1 TSEB model results

Estimates of SEBF using the TSEB were compared to BR measurements shown in Fig. 4.4 with corresponding performance statistics presented in Table 4.3. The results for DOY 160,167 and 138 were presented in one group separate from those for DOY 131 as the estimates were based on 60-m resolution thermal band imagery which, as expected, affected the model performance for this day as discussed later. A lower RMSE of 63 W m^{-2} was obtained for the airborne results compared to 83 W m^{-2} for the Landsat dataset.

Underestimation of SEBF was evident for both datasets for all days as indicated by the BIAS of -27 W m^{-2} and -26 W m^{-2} for Landsat and airborne, respectively. A narrower scatter around the 1:1 line occurred for the airborne dataset compared with those for the Landsat dataset (Fig. 4.4). The results for DOY 131 showed a lower RMSE of 62 W m^{-2} compared to123 W m^{-2} for airborne and Landsat datasets, respectively, (Table 4.4) with considerable scatter around the 1:1 line (Fig. 4.4) shown for the Landsat dataset. Previous studies by Kustas and Norman (2000a), Kustas et al. (2004), and others, indicated that a value of RMSE ~50 w m-2, and in some cases ~60 W m^{-2}, is reasonable for discrepancies in SEBF between model and measurements. However, these findings were based on analysis carried out over homogenous areas such as the Monsoon '90 and FIFE datasets (Norman et al. 1995), Cupid-simulated (plant-environment model) dataset (Kustas and Norman 2000a), and cropland in Iowa (Kustas et al. 2004). As Kustas and Norman (2000a) defined areas as extreme condition, based on Cupid simulation, to test the TSEB at, values of RMSE > 100 W m^{-2} were obtained. These extreme cases were generally riparian vegetation characterized by stressed and unstressed conditions, dry soil surface, and medium to tall canopy heights (Kustas and Norman 2000a). Note that all these studies, above, applied the TSEB. In a study carried out, in particularly, over dense tall, relatively homogenous, tamarisk forest in the riparian corridor of Rio Grande in the Bosque del Apache Wildlife Refuge located in south-central New Mexico, Kustas et al. (2002) applied a one-layer energy balance model using ground-based infrared thermometer data, even more accurate than remotely sensed TIR from airborne or Landsat sensors, and found values of RMSE of 111 W m^{-2} at max with average of 65 W

m^{-2}. This suggests that the obtained results over CNWR are comparable and can be considered reasonable.

Note that generally, most remote sensing based models provide relatively reasonable estimates of *Rn* and *G* with lower RMSE of ~< 40 W m^{-2} while most of the discrepancies appear on estimates of heat fluxes (i.e. λE and *H*) with higher RMSE of ~ > 40 W m^{-2}. This is because the relationship between heat fluxes and radiometric surface temperature is nonlinear as indicated by Kustas and Norman (2000a). In particular, for these datasets it is clear that most of the scatter around the 1:1 line (Fig. 4.4) appears clearly for estimates of heat fluxes λE and *H* for both airborne and Landsat datasets. However the airborne data showed less scatter around the 1:1 line compared to the Landsat data. The RMSE values for *H* and λE were 88 W m^{-2} and 74 W m^{-2} for airborne compared to 104 W m^{-2} and 101 W m^{-2} for Landsat imagery, respectively, for DOYs 161, 167, and 138. Notice that for the Landsat dataset the TSEB underestimated most values of H_{BR}~>250 W m^{-2} while the airborne dataset provided reasonable agreement with underestimation of H_{BR}~>350 W m^{-2}. This is likely related to the fact that the radiometric surface temperature, T_R, obtained with airborne sensor at much higher spatial resolutions managed to better capture the contrast of surface temperatures associated with heterogeneity. Examples of the T_R images obtained from both sensors are shown in Fig. 4.5 and support this fact.

Since the CNWR presented discontinuities in surface conditions that were rather extreme which may have been reflected in the measurements of heat fluxes, H_{BR} and λE_{BR} from the BR systems we further looked into the issue regarding the appropriateness and representativeness of these systems. For example for DOY 138 the BR reported values of

λE_{BR} as high as 450 W m^{-2} at Slytherin and as low as 100 W m^{-2} at Diablo with values of H_{BR} of 150 W m^{-2} and 400 W m^{-2}, respectively. Hence the issue that might arise here is to what extent the BR systems capture the corresponding heterogeneity of such surfaces? Because the size of the upwind footprint of the BR tower measurements covers only few hundred meters in the upwind direction, it could represent a localized effect considering the increased spatial heterogeneity. On the other hand the footprint of the LAS, covered several hundred meters capturing larger areas as well as the associated spatial heterogeneity. The footprint sizes of the Diablo BR tower and the LAS for Path 3 on DOY 138 are shown in Fig. 4.6. Note that as described in Geli et al. (2011), the LAS-based measurements of H_{LAS} for Path 3 were compared with the average of the measurements of H_{BR} from Diablo and Swamp towers and for Path 1 H_{LAS} were compared with H_{BR} from the Slytherin tower. A comparison between measured H_{LAS} and H_{BR} were made with estimates of H_{TSEB} (Fig. 4.7). The results showed that for the airborne dataset comparing estimates of H_{TSEB} with the H_{BR} resulted in a lower model performance than when comparing H_{TSEB} with H_{LAS} with values of RMSE of 86 and 33 W m^{-2}, respectively. For the Landsat dataset the comparison resulted in a RMSE of 149 and 89 W m^{-2} when comparing H_{TSEB} with H_{BR} and H_{LAS}, respectively. As the LAS only provides measurements of sensible heat flux H_{LAS}, the corresponding λE_{LAS} were estimated as a residual of the energy balance as $\lambda E_{LAS} = Rn_{BR} - G_{BR} - H_{LAS}$ with Rn_{BR} and G_{BR} obtained from the BR measurements. The corresponding λE_{TSEB} was obtained by integrating the spatial fluxes from the TSEB model using the LAS footprint weights. A similar approach for estimating λE_{LAS} based on LAS measurements was followed by Ezzahar et al. (2009) in which spatial Rn and G estimates from a one layer model were used but direct

measurements of H_{LAS} used instead. The results (Table 4.4) showed that comparing estimates of λE_{TSEB} with λE_{LAS} for the airborne dataset resulted in a better model performance than when comparing λE_{TSEB} with H_{BR} with RMSE values of 36 W m^{-2} and to 86 W m^{-2}, respectively. These results favor the use of LAS for assessing spatial heat fluxes especially over heterogeneous surfaces with extreme surface temperature conditions such as the CNWR. The work by Kleissl et al. (2009) and others, also suggested such methodology to validate spatial model estimates of fluxes using LAS measurements.

The CNWR study area provided a unique situation for testing the performance of the TSEB model with a wide range of surface conditions such as dense to sparse and tall to short vegetation with under stressed and unstressed growing conditions mostly with dry soil surface conditions. These scenarios were considered extreme as described in Kustas and Norman (2000a). As the BR systems were distributed over the area in a way that allowed the capture of fluxes representative of these conditions, we looked into the discrepancies in the estimates of heat fluxes and its association with the corresponding canopy height, h_c, leaf area index, *LAI*, wind speed, *u*, and stress conditions (Fig. 4.8). We obtained the corresponding h_c and *LAI*, based on the footprint of the BR towers. These variables were compared with the error in estimates of *H* (i.e. H_{TSEB}- H_{BR}) and λE (i.e. λE_{TSEB}-λE_{BR}). It appears that higher discrepancies are evident at u ~< 2 m s^{-1}, with underestimation of *H*, especially with the Landsat dataset estimates while lower differences resulted when using the airborne dataset. Short vegetation with h_c < =2 m resulted in significant error with the underestimation of *H* and values reaching approximately 150 W m^{-2}. Also at *LAI*<= 2.3 an increased error in the estimates

appeared. For all these plots (Fig. 4.8) it is clear that error in estimated heat fluxes based on the airborne dataset is fairly distributed around the zero-line while estimates based on the Landsat dataset showed increased scatter. On the other hand, the only source of water for the vegetation is from groundwater as its being recharged from the agricultural drain and the lower Colorado River. A detailed description of the water sources and soil moisture condition is presented by Nagler et al. (2008). Note that Diablo had the lowest moisture content and deepest groundwater table of ~3.5 m while Swamp has the highest soil moisture and shallowest groundwater table of ~ 2.0 m (Nagler et al. 2008).

Generally, the possible sources of error or uncertainty in model estimates would come from, as indicated from previous studies a) image registration b) footprint analysis c) sub-pixel heterogeneity Norman et al. (2003) d) Averaging period of heat flux measurements (Kustas et al. 2002) e) lack of energy balance closure of certain systems such as the eddy covariance (EC) (see e.g. Li et al. 2005) which makes the model fulfill energy closure but not the measurements, and we would like to add to that f) the representativeness and appropriateness of local scale based flux measurements such as BR and EC systems. Quantifying the possible contributions from each of these error sources is difficult; however, we can provide some indications. Image registration would be an issue especially for the airborne systems that provide 1-m and ~3-m pixel resolution in visible and TIR bands, respectively. The recent integration of the USU multispectral airborne system with the LASSI LiDAR will reduce this type of error while work to include the new FLIR thermal infrared camera as well will further improve the accuracy.. Footprint analysis could be an issue for the Landsat pixel resolutions and is reduced by using high enough resolution to capture sub-pixel heterogeneity (Li et al.

2008). It is clear that airborne imagery managed to capture the surface heterogeneity. Kustas et al. (2002) indicated that flux measurement averaging periods of 1-minute and 30-minutes resulted in increased error while a 10-min averaging period provided a better agreement when comparing a one-layer model with EC data. Note that in our study the BR data processed were based on a 15-min averaging period. With respect to local scale based measurements from flux towers being used for model verification, it appear that using LAS measurements provided better estimates in the heterogeneous conditions encountered resulting in a better agreement.

These results indicated that, for this type of surfaces with increased heterogeneity and extreme vegetation canopy conditions as the CNWR, using high spatial resolution data can improve the TSEB model performance considerably as the thermal infrared spatial resolution varied from 60, 30, and 3 m.

4.4.2 M-S model results

Herein, ET_{M-S}^{high} and ET_{M-S}^{low} represent estimates of daily *ET* based on the M-S method using LiDAR-derived h_c at 1-m and 30-m spatial resolution, respectively. As described in section 2b, the M-S method requires knowledge of K_c^{FAO} value for the specific type of vegetation to estimate the corresponding surface resistance, $(r_s)_c$, and hence ET_c or generally *ET*. Note that there were no values reported in Allen et al. (1998) or any other K_c values similar to those reported by Allen et al. (1998) for Tamarisk or Arrowweed. We directly used values of $(r_s)_c$ based on measurements obtained at CNWR by Nagler et al. (2003) who showed that Tamarisk has an average $(r_s)_c$ of 600 s m^{-1} considering its diurnal variation as it closes its stomata during late afternoon hours. Arroweed had an average $(r_s)_c$ of 4 s cm^{-1} as reported in Nagler et al. (2003). As the

application of the M-S method requires the stomatal surface resistance of the canopy $(r_s)_c$ equivalently it uses the surface resistance of the bare soil $(r_s)_s$. At CNWR the only source of water for plants to grow is groundwater which is about 3.0 m below ground surface during the summer months while the rainfall is less than 80 mm per year (Nagler et al. 2008). This leaves the top 40 cm layer nearly completely dry or at residual moisture content levels as indicated by Nagler et al. (2008) with soil moisture values considerably less that 0.1 cm^3 cm^{-3}. For bare soil the surface resistance, $(r_s)_s$, is strongly correlated to the soil moisture content of the top layer and could range between 500 - 6000 s m^{-1} for wet-dry bare soils (Daamen and Simmond 1996; Soegaard 1999; Boegh et al. 2002). Surface resistance for dry soil can range between 2000 to 6000 s m^{-1} as indicated by Soegaard (1999) and Boegh et al. (2002). We used an average value of 4000 s m^{-1} (4000 s m^{-1}).

ET_{M-S}^{high} resulted in a lower RMSE of 1.42 mm day^{-1} as compared to 1.59 mm day^{-1} for ET_{M-S}^{low} (Table 4.5) and both underestimated ET_{BR} with biases of -0.61 and -0.78 mm day^{-1} respectively. A similar distribution around the 1:1 line is shown by both estimates (Fig. 4.9). Despite the fact that different spatial aggregation methods could be used- exploring those effects on estimates of *ET* is an issue that's beyond our objectives. For this research we used a simple averaging approach to derive h_c map at 30-m spatial resolution from the 1-meter Lidar dataset. Considering the aforementioned point, the results indicated that using high spatial resolution h_c maps provided improved estimates of *ET*.

4.4.3 Comparing estimates of *ET* obtained from TSEB and M-S models

Instantaneous estimates of λE_{TSEB} from the TSEB were extrapolated to the daily values using the *EF* method described in section e. This method generally underestimates daily *ET* as indicated by Chavez et al. (2008). In addition Norman et al. (2003) indicated, based on studying the diurnal variation of the *EF*, that assuming constant *EF* for morning hours is reasonable while for the afternoon hours this might be an issue (in advective conditions?). Hence in some cases this assumption could lead to significant error. We noticed that for DOY 167 over Slytherin the BR showed a total *ET* of ~7.4 mm/day which was underestimated by both airborne and Landsat TSEB estimates as shown in Fig. 4.9. After extrapolating the instantaneous LE_{BR} of 469 W m^{-2} using the available energy (*Rn*-*G*) from the BR, the daily *ET* was about 20% lower. Note that the model provided instantaneous LE_{TSEB} of about 402 W m^{-2} for that day at Slytherin. Hence this might have some effect on the model performance indications as the M-S directly provides daily estimates of *ET* with no need for extrapolation.

It appears that the TSEB model or generally the thermal remote sensing approach provides estimates of *ET* that better represent the spatial heterogeneity of the surface features compared to M-S model (Fig. 4.10). One of the reasons is the fact that the value of the available daily energy (*Rn*-*G*) used in M-S method is a single average value of the entire area which should vary based on the surface type and growing conditions in case of vegetated surfaces. This can be improved by using remote sensing approaches to estimate *Rn* and *G* such as the TSEB model. Also, the *Rn*-*G* used were the BR measured values which might raise a question on the comparison of the S-M estimates with those from the TSEB where we did not use any of the measured fluxes in the model rather all were

estimated. The TSEB model provided the lowest RMSE of 1.23 mm day^{-1} of $ET_{TSEB}^{airborne}$ using the airborne data while the highest RMSE was around 1.6 mm day^{-1} for the ET_{M-S}^{low} obtained with the M-S based on 30-m h_c map. A reasonable scatter around the 1:1 line was shown by the TSEB estimates of ET_{TSEB} for both datasets with a reasonable variability in covering wide range of *ET* values between 2–6 mm day^{-1}. The M-S estimates of *ET* showed a bias toward overestimating low *ET* values and providing a narrow range of prediction between 4–6 mm day^{-1}. The M-S model didn't show much dependency on a changing canopy height as its estimates based on both the 1-m and the 30-m h_c map showed relatively similar scattering pattern around the 1:1 line. Note that the pixel-average values of h_c at the 30-m pixel resolution were generally lower than those as the 1-m resolution. This might indicate that the M-S more suitable to surfaces with crop vegetation with high *ET* and relatively homogenous vegetation height.

4.5 Conclusions

The effect of surface feature heterogeneity on modeling SEBF/*ET* was investigated. SEBF were estimated using the TSEB model based on Landsat 5 thematic mapper and airborne imagery that provided 30-60 m and 1-4 m pixel resolutions over a heterogeneous area dominated by tamarisk trees in the CNWR, California. The airborne-based SEBF were significantly better than those based on the Landsat as they resulted in a value of RMSE ~25 W m^{-2} lower. Most of the discrepancies in the estimated SEBF appeared in the heat fluxes *H* and λE. Using the Landsat dataset, the TSEB model showed an inability to properly estimate values of *H*~>250 W m^{-2} in some cases when the BR towers reported values of *H* between 300–500 W m^{-2}. On the other hand, the airborne

dataset manage to represents the associated surface heterogeneity especially the radiometric surface temperature, T_R, and hence provided better estimates of H with values up to ~350 W m^{-2}. This wide range of values of H estimated and measured at the CNWR provided extreme surface conditions. Note that lower H values of 100-200 W m-2 resulted over the tall dense and unstressed stands of tamarisk with dry soil surface and relatively shallower water table and better water quality. Medium to high values of H of 200-300 W m^{-2} resulted over the medium height relatively sparse unstressed stands of tamarisk and arroweed growing adjacent to sources of water, an agricultural drain and river, hence the shallowest water table in the area. High values of H of 300-500 W m-2 were estimated over the shortest canopy height, sparse and deepest water table conditions. So applying the TSEB using the Landsat data over the second and third surface conditions resulted in lower quality estimates of SEBF. This was presented here by showing the associated difference of model estimates according to varying wind speed, u, canopy height, h_c, leaf area index, LAI, soil moisture conditions, and depth to water table.

The use of local scale based measurements, such as the BR and EC methods, over such types of surfaces and environment might not be representative of larger heterogeneous spatial scales and can lead to misleading indications of model performance. However other footprint models should be considered and a method of taking into consideration the changes of atmospheric stability throughout the day should be further examined.

Comparing the airborne-based TSEB model estimates of H and λE with the BR data resulted in combined RMSE values of ~86 W m^{-2} while comparisons with LAS

based estimates of the fluxes resulted in a RMSE of ~33 W m^{-2}. As discussed earlier, there are different possible sources of uncertainty; however this improvement in modeling SEBF shown by using the airborne dataset can mostly be explained by the ability of high resolution data in capturing the surface heterogeneity especially of the radiometric surface temperature.

The extrapolated daily *ET* based on the TSEB model using the airborne dataset resulted in the lowest RMSE of 1.23 mm day^{-1} as it managed to capture the wide range of *ET* values varying from 2-6 mm day^{-1}. The M-S model provided reasonable estimates of the higher values of *ET* but over a narrower range of 4-6 mm day^{-1}. This suggests that the M-S method might have a lower performance over such heterogonous surfaces. In addition, the dependency of the M-S method on canopy height data to estimate *ET* might hinder its application over naturally vegetated areas. Canopy height data over agricultural areas are readily available in literature and makes it relatively easier to apply.

The findings of this research can be used for future applications of using fused data from multiple sensors to bridge the gap of the associated low frequency overpasses. This is similar to an on going effort by Anderson et al. (2011) on data fusion of *ET* using multiple sensors and thermal sharpening.

References

Allen, R. G., L. S. Pereira, D. Raes, and M. Smith, 1998: *Crop evapotranspiration: Guidelines for computing crop water requirements.* Paper No. 56. Food and Agricultural Organization of the UN, 328 pp.

Allen, R. G., W. O. Pruitt, J. L. Wright, T. A. Howell, F. Ventura, R. Snyder, D. Itenfisu, P. Steduto, J. Berengena, J. Baselga, M. Smith, L. S. Pereira, D. Raes, A. Perrier, I. Alves, I. Walter, and R. Elliott, 2006: A recommendation on standardized surface resistance for hourly calculation of reference ET_0 by the FAO56 Penman-Monteith method. *Agric. Water Manage.*, **81,** 1-22.

Allen, R. G., M. Tasumi, and R. Trezza, 2007: Satellite-based energy balance for mapping evapotranspiration with internalized calibration (METRIC)-Model. *J. Irrig. Drain. Syst.*, **133(4),** 380–394.

Anderson, M. C., J. M. Norman, G. R. Diak, W. P. Kustas, and J. R. Mecikalski, 1997: A two-source time integrated model for estimating surface fluxes using thermal infrared remote sensing. *Remote Sens. Environ.*, **60,** 195–216.

Anderson, M. C., J. M. Norman, J. R. Mecikalski, J. P. Otkin, and W. P. Kustas, 2007a: A climatological study of evapotranspiration and moisture stress across the continental U.S. based on thermal remote sensing: I. Model formulation. *J. Geophys. Res.*, 112, D10117, doi:10.1029/2006JD007506.

Anderson, M. C., J. M. Norman, J. R. Mecikalski, J. P. Otkin, and W. P. Kustas, 2007b: A climatological study of evapotranspiration and moisture stress across the continental U.S. based on thermal remote sensing: II. Surface moisture climatology. *J. Geophys. Res.* 112, D11112, doi:10.1029/2006JD007507.

Anderson, M. C., W. P. Kustas, J. M. Norman, C. R. Hain, J. R. Mecikalski, L. Schultz, M. P. Gonz´alez-Dugo, C. Cammalleri, G. d'Urso, A. Pimstein, and F. Gao, 2011: Mapping daily evapotranspiration at field to continental scales using geostationary and polar orbiting satellite imagery. *Hydrol. Earth Syst. Sci.*, **15,** 223–239.

Baldocchi, D. D., B. B. Hicks, and T. P. Meyers, 1988: Measuring biosphere-atmosphere exchange of biologically related gases with micrometeorological methods. *Ecology,* **69(5),** 1331–1340.

Bastiaanssen, W., M. Menenti, R. Feddes, and A. Holtslag, 1998: A remote sensing surface energy balance algorithm for land (SEBAL) 1. Formulation. *J. Hydrol.*, 212–213, 198–212, doi:10.1016/S0022-1694(98)00253-4.

Berk, A., L. S. Bernstein, and D. C. Robertson, 1989: MODTRAN: A moderate resolution model for LOWTRAN 7. Geophysics Laboratory, Bedford, Maryland, Rep. GL-TR-89-0122, 37 pp.

Boegh, E., H. Soegaard, and A. Thomsen, 2002: Evaluating evapotranspiration rates and surface conditions using Landsat TM to estimate atmospheric resistance and surface resistance. *Remote Sens. Environ.,* **79,** 329–343.

Brutsaert, W. (1982). *Evaporation into the Atmosphere: Theory, History, and Applications.* Springer, 299 pp.

Campbell, G. S., and J. M. Norman, 1998: *An Introduction to Environmental Biophysics*. 2nd ed. Springer, 286 pp.

Chavez, J. L., 2005: Validating surface energy balance fluxes derived from airborne remote sensing, PhD thesis, Utah State University, Utah, USA, 260 pp.

Chavez, J. L., P. H. Gowda, T. A. Howell, C. M. U. Neale, and K. S. Copeland, 2009: Estimating hourly crop ET using a two-source energy balance model and multispectral airborne imagery, *Irrig. Sci.*, doi:10.1007/s00271-009-0177-9.

Chavez, J. L., C. M. U. Neale, J. H. Prueger, and W. P. Kustas, 2008: Daily evapotranspiration estimates from extrapolating instantaneous airborne remote sensing ET values. *Irrig. Sci.*, **27,** 67–81.

Crow, W. T., F. Li, and W. P. Kustas, 2005: Intercomparison of spatially explicit models for predicting surface energy flux patterns during the 2002 SMACEX field experiment. *J. Hydrometeor.*, **6,** 941–953.

Daamen, C. C., and L. P. Simmonds, 1996: Measurement of evaporation from bare soil and its estimation using surface resistance. *Water Resour. Res.*, 32, 1392–1402.

Ezzahar, J., A. Chehbouni, J. Hoedjes, D. Ramier, N. Boulain, S. Boubkraoui, B. Cappelaere, L. Descroix, B. Mougenot, and F. Timouk, 2009: Combining scintillometer measurements and an aggregation scheme to estimate area-averaged latent heat flux during the AMMA experiment. *J. Hydrol.*, doi:10.1016/j.jhydrol.2009.01.010.

Horst, T. W., and J. C. Weil, 1994: How far is far enough?: The fetch requirements for micrometeorological measurement of surface fluxes. *J. Atmos. Oceanic Technol.*, **11,** 1018–1025.

Horst, T. W., and J. C. Weil, 1992: Footprint estimation for scalar flux measurements in the atmospheric surface layer. *Bound.-Layer Meteor.*, **59,** 279–296.

Houser, P. R., W. J. Shuttleworth, J. S. Famiglietti, H. V. Gupta, K. H. Syed, and D. C. Goodrich, 1998: Integration of soil moisture remote sensing and hydrologic modeling using data assimilation. *Water Resour. Res.,* **34,** 3405–3420.

Humes, K., R. Hardy, W. P. Kustas, J. Prueger, and P. Starks, 2003: High spatial resolution mapping of surface energy balance components with remotely sensed data. (Chapter 3) In: D. A. Quattrochi & J. C. Luvall (Eds.), *Thermal Remote Sensing in Land Surface Processes* (pp. 110-132). Boca Raton, FL: CRC Press.

Kalma, J. D., T. R. McVicar, and M. F. McCabe, 2008: Estimating land surface evaporation: a review of methods using remotely sensing surface temperature data. *Surv. Geophys.*, **29,** 421-429.

Kleissl, J., S.-h. Hong, and J. M. H. Hendrickx, 2009: New Mexico scintillometer network in support of remote sensing, and hydrologic and meteorological models. *Bull. Amer. Meteor. Soc.*, **90,** 207-218, DOI:10.1175/2008BAMS2480.1.

Kohsiek, W., C. Liebethal, T. Foken, R. Vogt, S. P. Oncley, , Ch. Bernhofer, H. A. R. De Bruin, 2007: The Energy Balance Experiment EBEX-2000. Part III: behaviour and quality of the radiation measurements. *Bound.-Layer Meteor.*, **123,** 55–75.

Kustas, W. P., and M. C. Anderson 2009: Advances in thermal infrared remote sensing for land surface modeling. *Agric. Forest Meteor.*, **149,** 2071-2081.

Kustas, W. P., and J. M. Norman, 2000a: Evaluating the effects of subpixel heterogeneity on pixel average fluxes. *Remote Sens. Environ.*, **74,** 327– 342.

Kustas W. P. and J. M. Norman, 2000b: A two-source energy balance approach using directional radiometric temperature observations for sparse canopy covered surface. *Agronomy J.*, 92, 847–854.

Kustas, W. P., and J. M. Norman, 1999: Evaluation of soil and vegetation heat flux predictions using a simple two-source model with radiometric temperatures for partial canopy cover. *Agric. Forest Meteor.*, **94,** 13–29.

Kustas, W. P., F. Li, T. J. Jackson, J. H. Prueger, J. I. MacPherson, and M. Wolde 2004: Effect of remote sensing pixel resolution on modeled energy flux variability of cropland in Iowa. *Remote Sens. Environ.*, **92,** 545-547.

Kustas, W. P., J. H. Prueger, and L. E. Hipps, 2002: Impact of Using Different Time-Averaged Inputs for Estimating Sensible Heat Flux of Riparian Vegetation Using Radiometric Surface Temperature. *J. Appl. Meteor.*, 41, 319–332.

Kustas, W. P., J. H. Prueger, L. E. Hipps, J. H. Hatfield, and D. Meek, 1998a: Inconsistencies in net radiation estimates from use of several models of instruments in a desert environment. *Agric. Forest Meteor.*, **90,** 257–268.

Kustas, W. P., X., Zhan, and T. J. Schmugge, 1998b: Combining optical and microwave remote sensing for mapping energy fluxes in a semiarid watershed. *Remote Sens. Environ.*, **64,** 116–131.

Kustas, W. P., J. M. Norman, M. C. Anderson, and A. N. French, 2003: Estimating subpixel surface temperatures and energy fluxes from the vegetation index – radiometric temperature relationship. *Remote Sens. Environ.*, **85,** 429– 440.

Li, F, W. P. Kustas, J. H. Prueger, C. M. U. Neale, and T. J. Jackson, 2005: Utility of remote sensing based two-source energy balance model under low and high vegetation cover conditions. *J. Hydrometeor.*, **6(6),** 878–891.

Li, F, T.J. Jackson, W. P. Kustas, T. J. Schmugge, A. N. French, M. H. Cosh, and R. Bindlish, 2004: Deriving land surface temperature from Landsat 5 and 7 during SMEX02/SMACEX. *Remote Sens. Environ.*, **92,** 521–534.

Li, F., W. P. Kustas, M. C. Anderson, J. H. Preuger, and R. L. Scott, 2008: Effect of remote sensing spatial resolution on interpreting tower-based flux observations. *Remote Sens. Environ.,* **112,** 337–349.

Meijerink, A. M. J., A. S. M. Gieske, and D. Vekerdy, 2005: Surface energy balance using satellite data for the water balance of a traditional irrigation wetland system in SW Iran. *Irrig. Drain. Syst.*, **19,** 89−105.

Menenti, M., and B. Choudhury, 1993: Parameterization of land surface evaporation by means of location dependent potential evaporation and surface temperature range. IAHS Publication no. **212,** 561–568.

Moran, M. S., 2004: Thermal infrared measurements as indicator of plant ecosystem health. (Chapter 8) In: D. A. Quattrochi & J. C. Luvall (Eds.), *Thermal Remote Sensing in Land Surface Processes* (pp. 257-282). Boca Raton, Floirda: CRC Press.

Moran, M. S., K. S. Humes, and P. J. Pinter Jr., 1997: The scaling characteristics of remotely-sensed variables for sparsely-vegetated heterogeneous landscapes. *J. Hydrol.*, **190,** 337– 362.

Moran, M. S., S. J. Maas, and P. J. Pinter Jr., 1995: Combining remote sensing and modeling for estimating surface evaporation and biomass production. *Remote Sens. Rev.*, **12,** 335–353.

Monteith, J. L. 1965: Evaporation and environment. *Symp. Soc. Exp. Biol.* **19,** 205-234.

Mu, Q., F. A. Heinsch, M. S. Zhao, and S. W. Running, 2007: Development of a global evapotranspiration algorithm based on MODIS and global meteorology data. *Remote Sens. Environ.*, **111,** 519–536.

Nagler, P. L., E. P. Glenn, and T. L. Thompson, 2003: Comparison of transpiration rates among saltcedar, cottonwood and willow trees by sap flow and canopy temperature methods. *Agric. Forest Meteor.*, **116,** 73–89.

Nagler, P. L., E. P. Glenn, K. Didan, J. Osterberg, F. Jordan, and J. Cunningham, 2008: Wide-area estimates of stand structure and water use of tamarix spp. on the Lower Colorado River: implications for restoration and water management projects. *Restor. Ecology*, **16,** 136–145, DOI: 10.1111/j.1526-100X.2008.00356.x.

Neale, C. M. U., and B. Crowther, 1994: An airborne multispectral video/radiometer remote sensing system: Development and calibration. *Remote Sens. Environ.,* **49,** 187–194.

Norman, J. M., W. P. Kustas, and K. S. Humes, 1995: A two-source approach for estimating soil and vegetation energy fluxes in observations of directional radiometric surface temperature. *Agric. Forest Meteor.,* **77,** 263–293.

Norman, J. M., M. C. Anderson, W. P. Kustas, A. N. French, J. Mecikalski, R. Torn, G. R. Diak, T. J. Schmugge, and B. C. W. Tanner, 2003: Remote sensing of surface energy fluxes at 10^1-m pixel resolutions. *Water Resour. Res.,* **39(8),** 1221, doi:10.1029/2002WR001775.

Schmid, H. P., 1995: Source area for scalars and scalar fluxes. *Bound.-Layer Meteor.*, **67,** 293–318.

Sellers, P. J., Y. Mintz, Y. C. Sud, and A. Dalcher, 1986: A simple biosphere model (SIB) for use within general circulation models. *J. Atmos. Sci.*, **43,** 505–531.

Shuttleworth, W. J., 2006: Towards one-step estimation of crop water requirement. *Trans. Amer. Soc. Agric. Biolog. Engin.*, **49(4),** 925-935.

Shuttleworth, W. J., and J. S. Wallace, 1985: Evaporation from sparse crops: An energy combination theory. *Quart. J. Roy. Meteor. Soc.*, **111(465),** 889-855.

Shuttleworth, W. J., and J. S. Wallace, 2009: Calculating the water requirements of irrigated crops in Australia using the Matt-Shuttleworth approach. *Trans.Amer. Soc. Agric. Biolog. Engin.*, **52(6),** 1895-1906.

Soegaard, H., 1999: Fluxes of carbon dioxide, water vapour and sensible heat in a boreal agricultural area of Sweden – scaled from canopy to landscape level. *Agric. Forest Meteor.*. **98-99,** 463-478.

TABLE 4.1. Description of the Landsat dataset used in the study.

Dates	DOY	Overpass (PST)	Pixel resolution (m)		Path	Row
			TIR band	Shortwave bands		
June 9th 2007	160	10:04	30	30	38	37
June 16th 2007	167	10:10	30	30	39	37
May 10th 2008	131	9:58	60	30	38	37
May 17th 2008	138	10:04	30	30	39	37

TABLE 4.2. Description of the airborne dataset used in the study.

Dates	DOY	Flight center time (PST)	Pixel resolution (m)	
			TIR band	Shortwave bands
June 9th 2007	160	10:12	4	1
June 16th 2007	167	1:12	3	1
May 10th 2008	131	11:10	3	2
May 17th 2008	138	10:00	3	1

TABLE 4.3. Summary of performance statistics of the TSEB model estimates of surface energy balance fluxes (SEBF) based on Landsat and airborne datasets.

		RMSE ($W\ m^{-2}$)	MAE ($W\ m^{-2}$)	BIAS ($W\ m^{-2}$)
DOY 160, 167, 138				
	Landsat	83	70	-34
	Airborne	63	47	-23
DOY 131				
	Landsat	123	98	-9
	Airborne	62	45	-24
Overall				
	Landsat	96	79	-27
	Airborne	63	48	-26

TABLE 4.4. Comparison of TSEB model performance statistics based on BR and LAS measurements of heat fluxes H and λE for DOYs 131 and 138. Estimates of H_{TSEB} and λE_{TSEB} were compared with H_{BR} and λE_{BR} as well as with the corresponding H_{LAS} and λE_{LAS} for Landsat and airborne datasets.

		RMSE ($W\ m^{-2}$)	MAE ($W\ m^{-2}$)	BIAS ($W\ m^{-2}$)
Landsat				
	H_{LAS}	89	76	-76
	H_{BR}	149	133	-129
	λE_{LAS}	62	52	42
	λE_{BR}	136	128	108
Airborne				
	H_{LAS}	33	28	3
	H_{BR}	86	70	-5
	λE_{LAS}	36	29	-29
	λE_{BR}	86	68	-34

TABLE 4.5. Summary of performance statistics for the TSEB and M-S models estimates of ET_{TSEB} and $ET_{M\text{-}S}$, respectively. ET_{TSEB} were based on the Landsat and airborne dataset while $ET_{M\text{-}S}$ based h_c maps at high (1-m) and low (30-m) pixel resolutions.

	ET_{TSEB}		$ET_{M\text{-}S}$	
	Landsat	Airborne	High	Low
RMSE (mm day^{-1})	1.49	1.23	1.38	1.6
MAE (mm day^{-1})	1.23	0.85	1.04	1.36
BIAS (mm day^{-1})	0.08	0.29	-0.53	-0.79

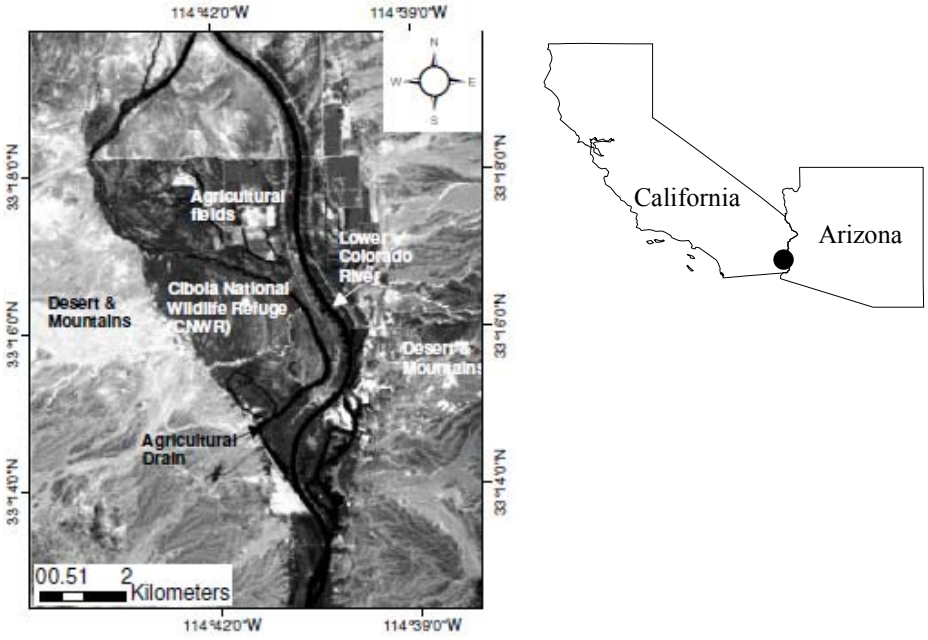

Fig. 4.1. Location of the study area Cibola National Wildlife Refuge (CNWR)

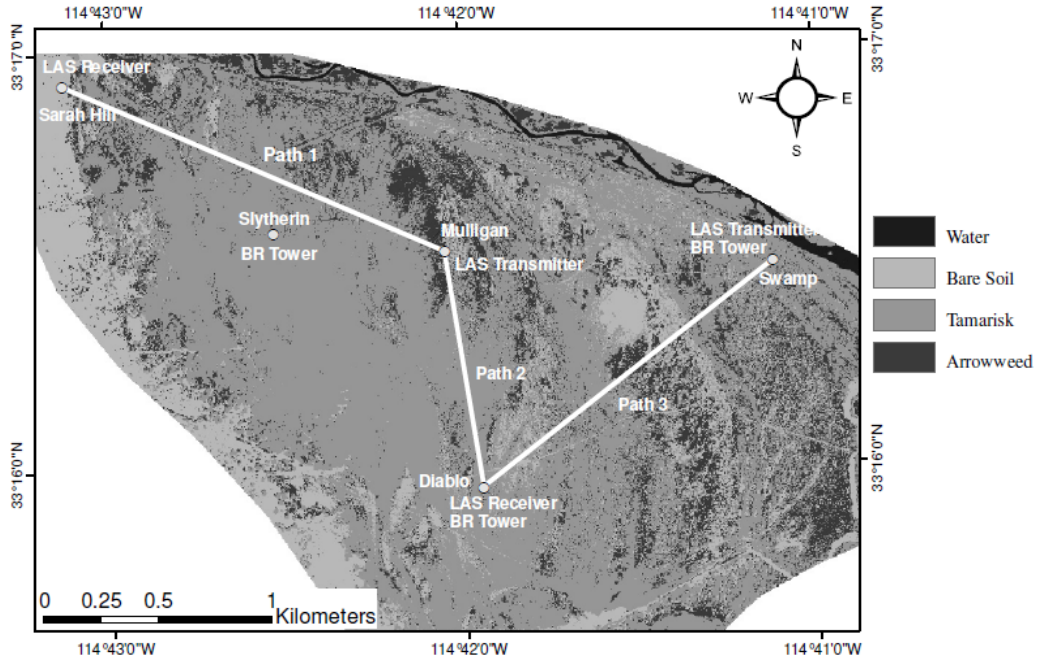

Fig. 4.2. The land cover classification map of CNWR shown at 1-m spatial resolution.

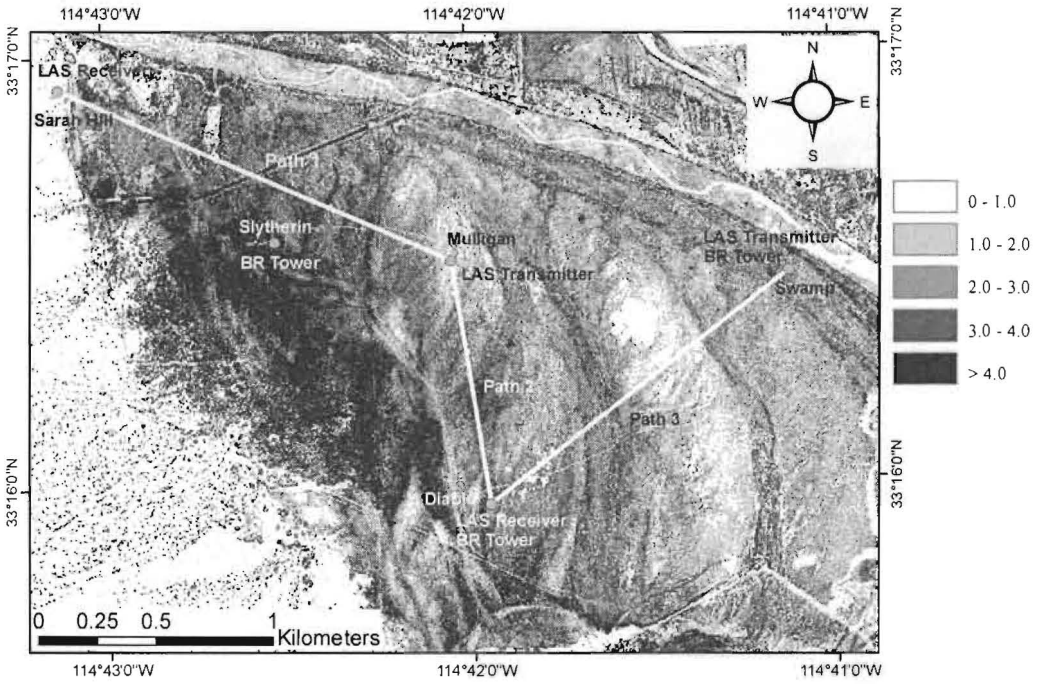

Fig. 4.3. Map showing the LiDAR-derived h_c at 1-m pixel resolution along with the BR tower locations and the LAS layout at the CNWR.

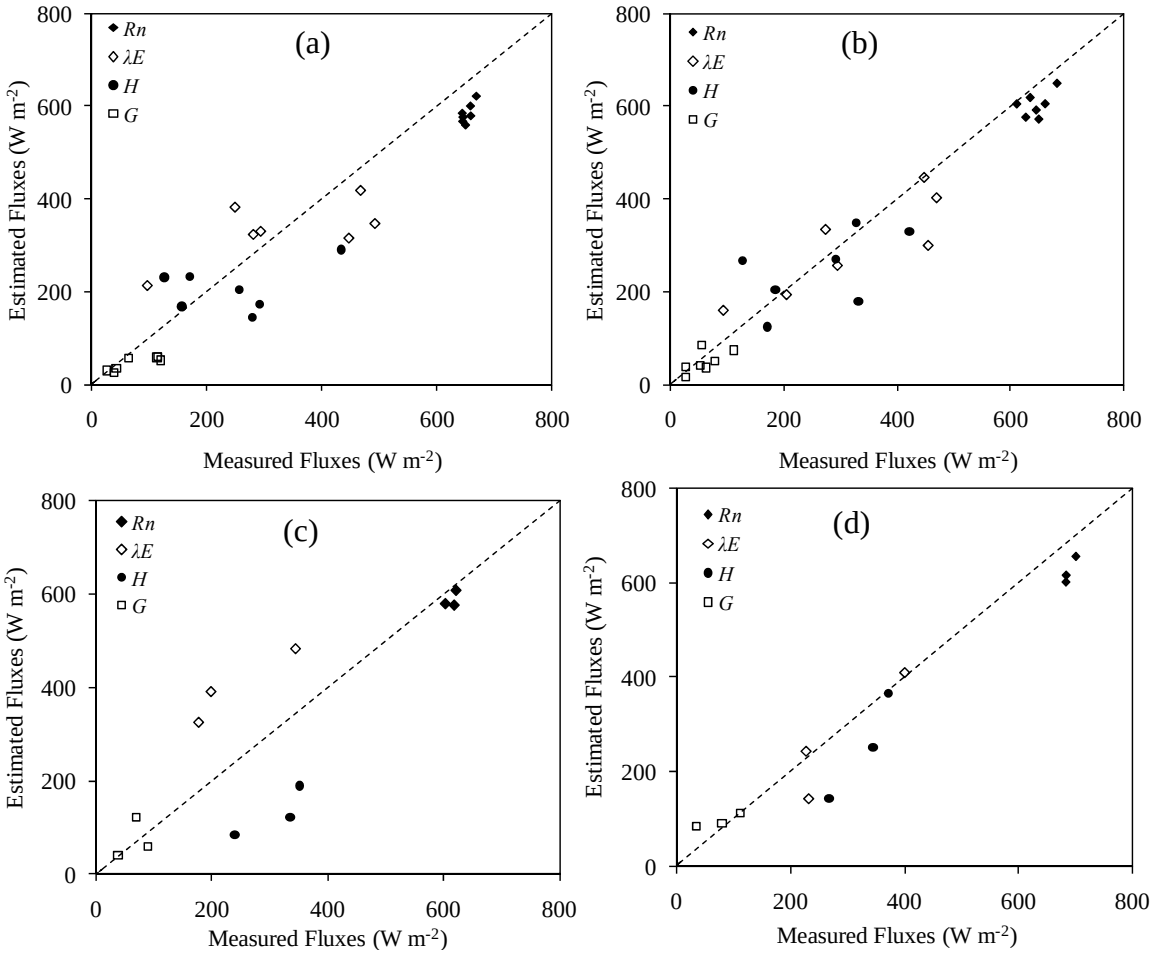

Fig. 4.4. Comparison of estimated surface energy fluxes based on TSEB with BR measurements for a) Landsat data DOYs 160, 167, and 138 b) Airborne data DOYs 160, 167, and 138 c) Landsat data DOY 131 and d) Airborne data DOY 131.

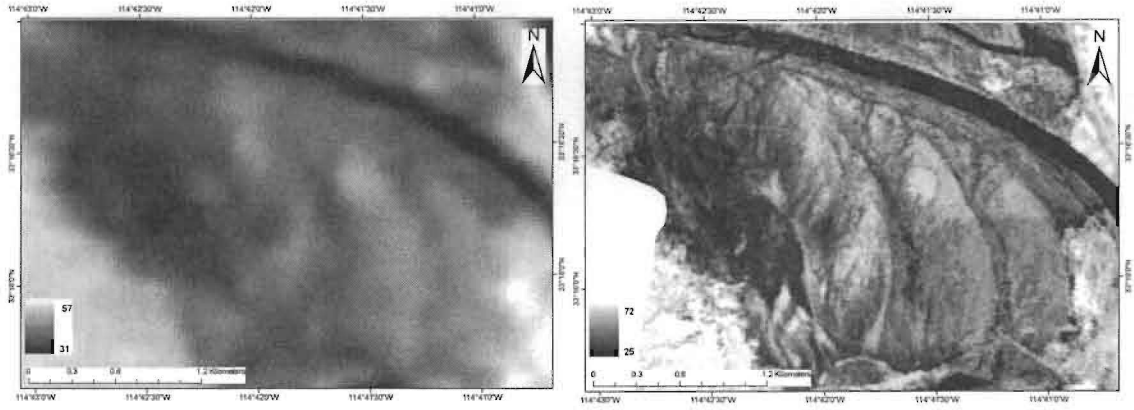

Fig. 4.5. Radiometric surface temperature T_R in (°C) for May 17th, 2008 DOY 138 from a) the Landsat 5 Thematic Mapper, and b) the USU Airborne Inframetric 760 sensor.

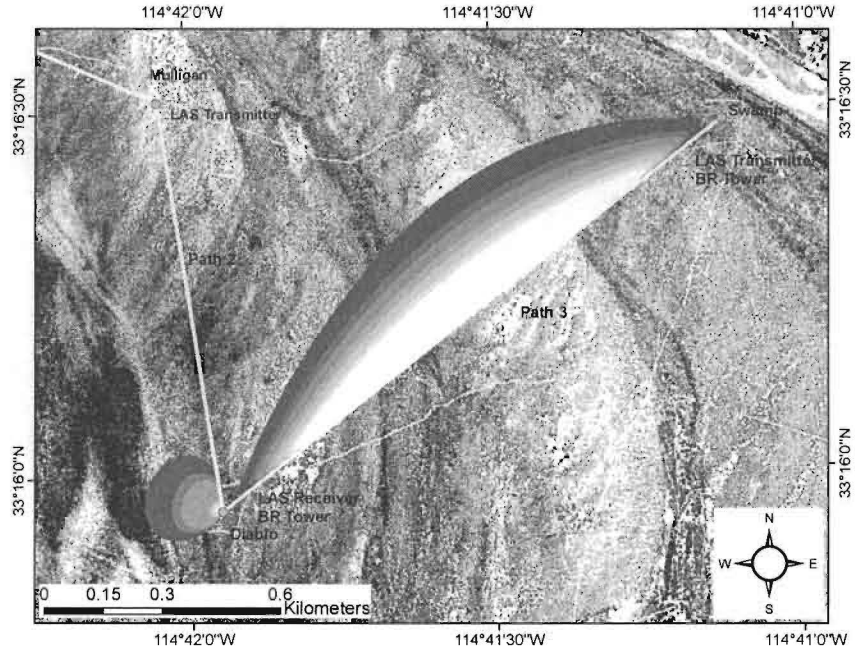

Fig. 4.6. Comparison of the footprint sizes for the BR system at the Diablo tower and LAS for Path 3 between Diablo and Swamp for DOY 138 overlaid with canopy height, h_c, map at 1-m pixel resolution.

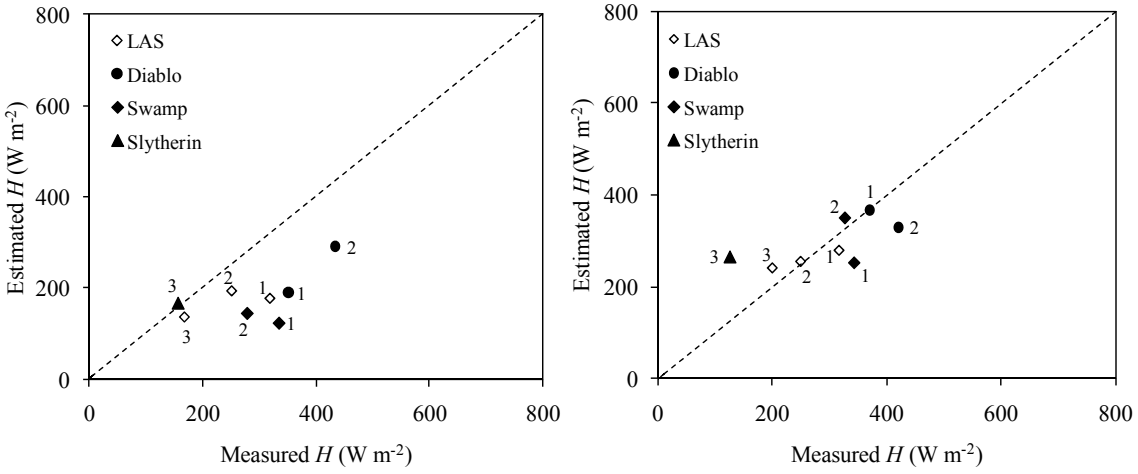

Fig. 4.7. Comparison between measured and estimated *H*. a) Measured H_{BR} from Diablo (dot), Swamp (filled diamond), Slytherin (filled triangle) towers compared with estimated (footprint integrated) H_{TSEB} and b) measured scintillometer-based H_{LAS} compared with H_{TSEB}. The numbers indicates a group of H_{BR} and the corresponding H_{LAS}, for example, 1 refers to comparison made with H_{BR} from Diablo and Swamp BR towers as well as with the corresponding H_{LAS} from scintillometer.

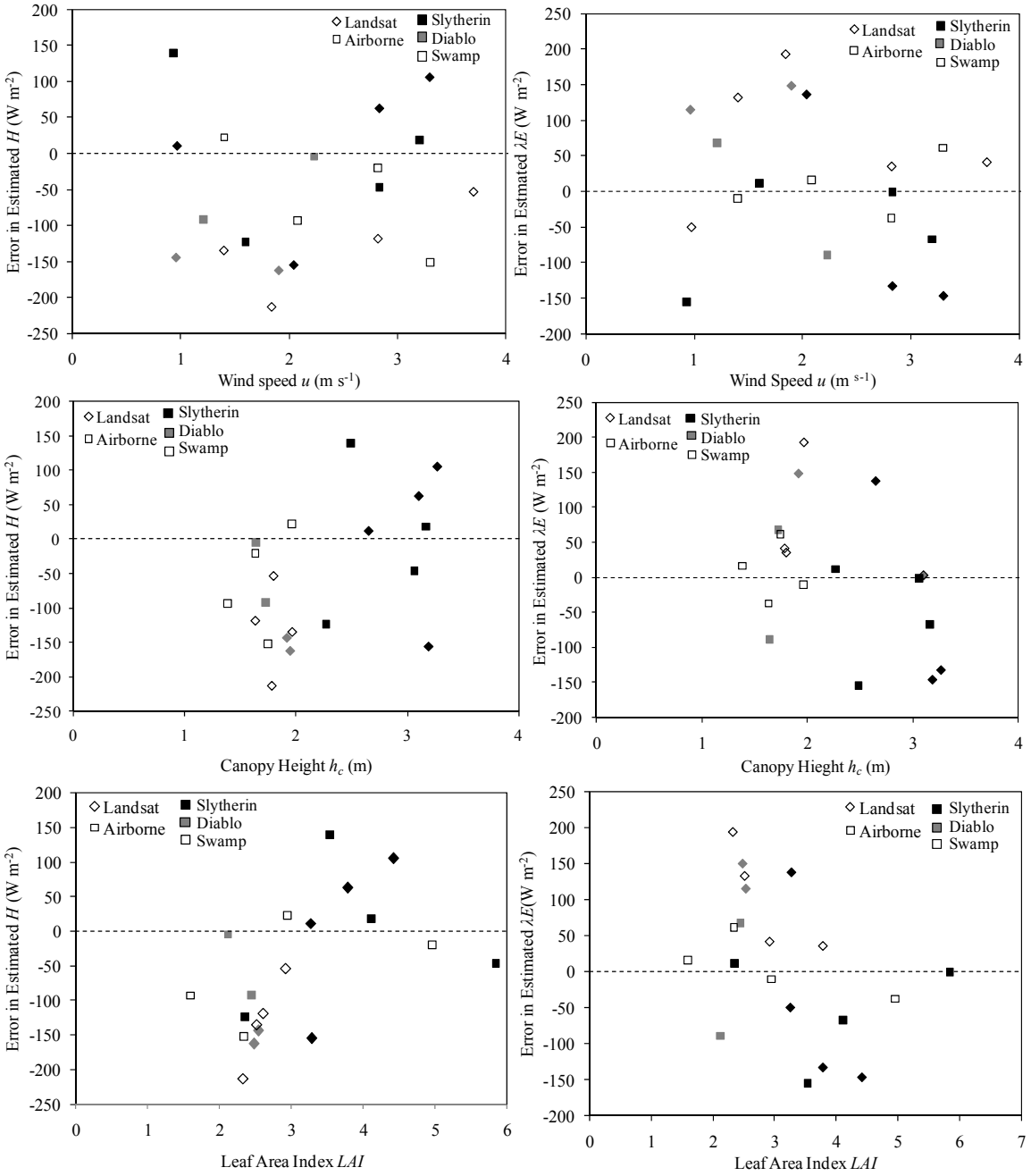

Fig. 4.8. Errors in the estimated H (i.e. H_{TSEB} - H_{BR}) and λE (i.e. λE_{TSEB} - λE_{BR}) with the corresponding measured wind speed u, and the BR footprint-based canopy height h_c and leaf area index LAI.

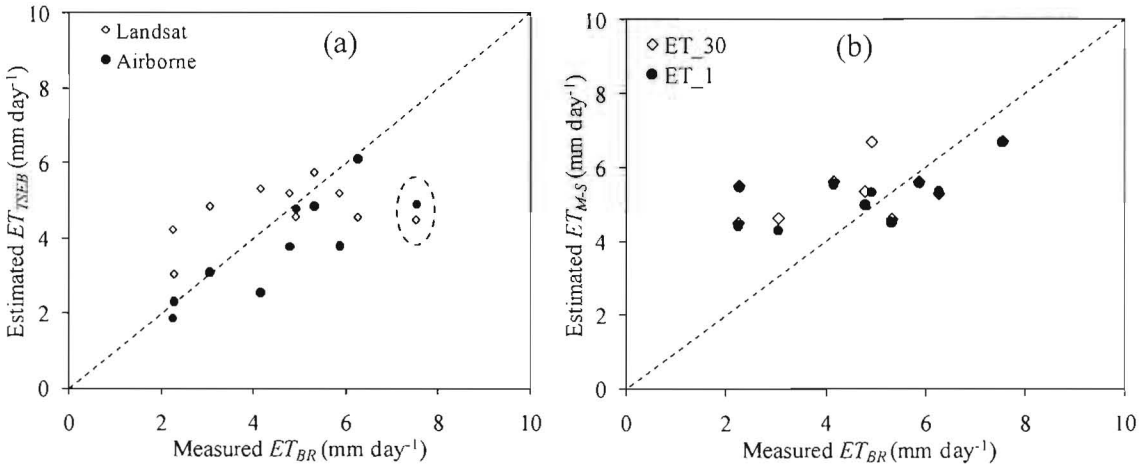

Fig. 4.9. Scatter plot of estimated *ET* based on a) the TSEB model using the Landsat and airborne datasets, and b) the M-S method for both ET_{M-S}^{high} and ET_{M-S}^{low} based on the 1-m and 30-m pixel resolution h_c map.

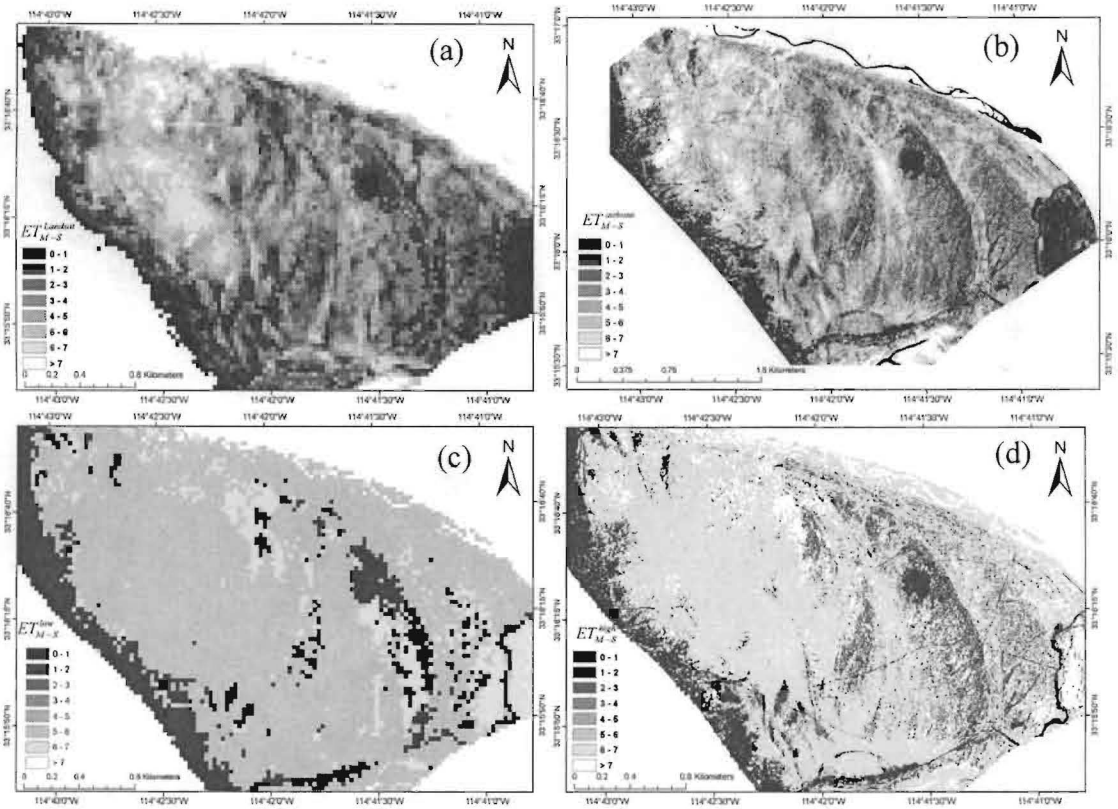

Fig. 4.10. Example of spatial daily estimates of *ET* for June 16th, 2007, DOY 167. The TSEB model estimates of a) $ET_{TSEB}^{Landsat}$ and b) $ET_{TSEB}^{airborne}$ using the airborne and Landsat datasets, respectively. The M-S model estimates of c) ET_{M-S}^{low} and b) ET_{M-S}^{high} using 1-m and 30-m pixel resolution canopy height, h_c, maps, respectively.

CHAPTER 5

SUMMARY, CONCLUSIONS, AND RECOMMENDATIONS

5.1 Summary and conclusions

Providing estimates of surface energy balance fluxes (SEBF) and evapotranspiration (*ET*) with a reasonable accuracy at different scales under heterogenous and non-ideal surface conditions were the main goals of the research. Modeling of SEBF/*ET* requires a) understanding land-atmosphere interactions over different surfaces and b) acknowledging and quantifying the representation of surface features when using remote sensing data. This dissertation was specifically aimed towards understanding the effect of surface feature representation on modeling SEBF especially over heterogeneously vegetated areas.

The research objectives were achieved by a) coupling a remote sensing based technique with a traditional water balance approach with the goal of properly capturing the associated temporal and spatial variability to provide estimates of *ET* over agricultural areas, and b) quantifying the effects of using different representations of surface features with regards to pixel resolution on both measured and modeling SEBF of riparian vegetation.

An overview of some issues that might arise during the modeling of energy exchange over different types of surfaces was provided in the introduction (Chapter 1) and the main research subject was detailed in Chapter 2 through 4. In this chapter we summarized the research findings made some recommendations.

In Chapter 2 we investigated the effects of temporal and spatial variability of surface features on estimates of *ET*. The main issue raised was that the recurrence of

remote sensing data of 16 days to a week, in case of Landsat, makes it difficult to monitor *ET* on daily basis. The gap in between satellite overpass dates requires filling with spatial estimates of *ET*. This was achieved, in this study, by coupling a remote sensing model with a traditional soil water balance method following a hybrid approach.

We used the thermal remote sensing based approach named the two source energy balance (TSEB) model of Norman et al. (1995) to estimate of SEBF and *ET* during satellite overpass dates. We also used the FAO-56 approach of Allen et al. (1998) to obtain direct daily estimates of *ET*. By coupling these two models we managed to overcome the lack of temporal coverage of the seasonal estimates of *ET*.

We introduced a modification to the FAO-56 by using remotely sensed/reflectance based K_{cb} (K_{cbrf}) instead of the tabulated values. K_{cbrf} is an improvement over the K_{cb} since it: a) provides the in-field spatial variability of the growing patterns, b) reflects the actual plant development progress (Neale et al. 1989; Bausch 1993), c) is independent of the water balance calculations of the root zone which are needed by the FAO-56 in order to update K_{cb} on daily basis. On the satellite overpass dates estimates of *ET* from the TSEB were compared to each other. Estimates of *ET* based on FAO-56 method were improved by assimilating those from the TSEB using statistical interpolation (Daley 1991). In between satellite overpass dates K_{cbrf} values were linearly interpolated to provide estimates of *ET*.

The hybrid *ET* approach was tested over rainfed corn and soybean fields in Ames, Iowa using data from the SMACEX project (Kustas et al. 2005). We used 5 scenes from Landsat 5/7 and airborne sensors. The results indicate that coupling the two models provided estimates of *ET* with a good agreement with measurements. Comparison of

estimates of *ET* before and after assimilation showed values of root mean square error (RMSE) of 1.26 and 0.67 mm day^{-1}, respectively. Its advantage was confirmed when using the K_{cbrf} instead of K_{cb} since it provided the actual crop conditions and its potential to evaporate. Note that the FAO-56 method provides estimates of *ET* based on soil moisture status in the root zone. Thus as the assimilation process updates the value of *ET* it consequently updated the soil moisture status in the root zone.

So the effect of updating estimates of *ET* using the hybrid *ET* approach on the soil moisture status in the root zone. We compared the updated soil moisture status in the top 0-10, 10-20, 20-30 cm layers as well as for the overall top-30 cm with measurements. A physically based soil moisture model (Sellers et al. 1986; Luo et al. 2003) was used to provide its estimate at multiple layers. The RMSEs of the soil moisture for the top-30 layer after assimilation were the lowest at the three measurements locations. Generally most of the variation in the soil moisture occurs at the top 0-80 cm (e.g. Suleiman 2008; Sheikh et al. 2009). Therefore our results from the top 30 cm can be considered an indication of the improvement in the soil moisture status of the entire root zone. It appears that the hybrid *ET* approach managed to a) reasonably capture the associated spatial and temporal surface variability as indicated by its estimates of *ET*, b) improve modeling of the soil moisture in the root zone.

We investigated the associated effects of surface features heterogeneity with regards to its representation using remote sensing data on both measurements and modeled SEBF described in Chapters 3 and 4, respectively. The accuracy of areal measurements of sensible heat flux (*H*) obtained using large aperture scintillometer (LAS) was discussed in Chapter 3. One of the reasons in the rising trend in the use of

scintillometry is because it can provide areal estimates of H at the several kilometer scale (Meijninger et al. 2002a, 2002b) compared to the local scale Bowen ratio (BR) and eddy covariance (EC) systems.

The main issue with LAS application is how to better incorporate surface feature variability in its estimates of H. The variable surface features considered in this study were canopy height (h_c), roughness length (d), zero-plane displacement height (z_0), and LAS beam height (z_u).

The application of scintillometry over a tamarisk dominated riparian floodplain at the Cibola National Wildlife Refuge (CNWR), California was examined. This area represented extreme heterogeneous type of surfaces described by vegetation interspersed with bare soil and considerable variability in canopy height, root zone soil moisture status, and depth to groundwater. The LAS layout, which consisted of three different paths were designed to capture variability in surface heterogeneity.

Surface roughness characteristics were incorporated in LAS measurements of H using three different scenarios. First (scenario a) we considered using an average h_c value around the center of the LASs' path as it would be obtained from vegetation survey methods- with the corresponding average z_u based on topographic map at the 1:24000 scale. In scenario b, we used path weighted h_c with the corresponding z_u based on LiDAR-derived topography and h_c maps. In scenario c, we used LAS 3D footprint based estimates of h_c and z_u.

The results showed that incorporating h_c and z_u using LAS 3D footprint approach (scenario c) resulted in considerably improved estimates of H when compared with BR. The RMSE was reduced by ~18 W m^{-2}, when comparing scenarios c and a, and ~ 11 W

m^{-2}, when comparing scenario b and a. This was particularly noticed for Path 3 that passed over areas with increased heterogeneity. The footprint areas for Path 3 showed short vegetation with areal average of $h_c \leq 2$ m covering ~70-80 % interspersed with bare soil ~ 20-30% providing LAI ≤ 2.5 but with less variability in topography. This wasn't the case over areas with relatively tall and dense vegetation which can be considered homogeneous conditions such as for Path 1. The RMSE was reduced ~5 W m^{-2} when comparing scenario b and a. Similarly for Path 1 the corresponding areal average of h_c was ~>= 5.5 m with vegetation covering ~ 95% with a LAI of ~4.

This improvement in LAS estimates of *H* could be related to a combination of two factors. First the method used to represent and incorporate surface roughness i.e. scenarios a-c, secondly the quality and richness of the data used. As both topography and surface roughness affect the quality of estimates of *H* it appears that topography had the least effect. Over Path 1, where topographic variability was the most and the roughness the least, the improvement in estimates of *H* was the smallest when comparing scenarios a and b. This suggests that the associated error would be less significant as long as information about topography, either from traditional maps or LiDAR, reasonably depicts it's general variability. On the other hand, Path 3 showed less/no variability in topography when comparing the three scenarios while the differences in roughness values appeared clearly. This supports the fact that LiDAR methods –in terms of topography and surface roughness- managed to capture and to represent well the heterogeneity of the surface. Thus more of the effects on LAS-based estimates of *H* were from surface roughness.

In the absence of LiDAR data one could use any other type of canopy height models, if available, to obtained spatial estimates of h_c such as those based on remotely sensed vegetation indices (VI). However, this will add to the uncertainty in estimates of H when considering that LiDAR has absolute point accuracy that could be up to ~7 cm and relative accuracy of ~ 2 cm. Considering the fact that LiDAR is the most accurate type of system available at present time to provide such high quality h_c maps other models will certainly have a lower accuracy. In this study we made no attempt to investigate the effect of using different canopy height models on LAS based measurements of H. This might be considered as a suggestion for future studies.

Another point worthy of mention is that we placed the LAS close to surface specifically below the blending height. This implies that its measurements were more affected and represent conditions from localized individual patches. So it is necessary at such LAS settings to incorporate detailed data about the surface (i.e. LiDAR) and use LAS 3D footprints. However, where LAS is installed at or above the blending height (Meijninger et al. 2002a, 2002b) this might not be required since the measurements are less sensitive to roughness parameters (De Bruin et al. 1995). In such cases the use of such detailed data about surface roughness and/or the LAS footprints still needs some investigation. This could be another area for future research where the proper height to mount LAS in heterogeneous areas could be examined.

This study has shown that the use of high accuracy surface feature data obtained from airborne LiDAR improved the performance of the scintillometer estimates dramatically. Field vegetation surveys and traditional topographic maps will not properly represent spatial heterogeneity in complex sparse semi-arid systems. Using a path

weighted average might be a good approximation, in some cases, for representing the spatial heterogeneity around the scintillometer. However, the use of LAS 3D footprint would be the most appropriate.

In paper 3 (Chapter 4), we investigated the effects of pixel resolution and surface characteristics representation derived from multiple sensors on modeled SEBF. The considered characteristics were *LAI*, h_c, and radiometric temperature (Tr). We specifically looked in to how these data can properly capture the associated surface heterogeneity.

To address the objectives we compared the application of the TSEB model of Norman et al. (1995), and the traditional Matt-Shuttleworth (M-S) method (Shuttleworth 2006). The TSEB model provided estimates of SEBF while the M-S method provided only estimates of *ET*. The analysis was carried out at the CNWR using datasets from Landsat 5 and the USU airborne digital system to obtain information about surface features including *LAI*, fraction of cover (f_c), and T_r in addition to the LiDAR-derived h_c map. The pixel resolution of the Landsat 5 dataset were at 30-m and 60-m. The airborne dataset were at 1-4 m pixel resolution. Note that airborne images were acquired at the same overpass dates, but not necessarily at same time as the Landsat 5 overpass, to assure the objectivity of our comparison. Model estimates were compared with BR measurements taken at three locations Slytherin, Diablo, and Swamp originally placed taking into consideration vegetation density and height.

The results indicated that estimates of SEBF using the airborne dataset provided good agreement when compared with the measurements. The RMSE for estimated SEBF based on the airborne dataset was lower by ~20 W m^{-2} compared to those based on the Landsat dataset. The error in modeled SEBF was examined versus LAI, hc, wind speed

(u), soil moisture content, and water table level. Modeling with the Landsat imagery, an increased error was noticed at lower values of LAI ~≤ 2.3 and at relatively short vegetation with $h_c \leq 2$ m conditions found over sparsely covered areas such as close to the Diablo tower. While with the airborne dataset estimates of SEBF were better under these conditions of *LAI* and h_c. Moreover, higher discrepancies appeared during relatively low values of $u \leq 2$ m s^{-1}. These values of u were associated with higher values of H of ≥ 350 W m^{-2}. We found that these higher discrepancies occurred in areas with low soil moisture, deepest groundwater table and higher salinity levels such as at the Diablo tower.

The uncertainties associated with spatial estimates of SEBF were reduced when using high resolution airborne images. This includes relative error due to sub-pixel heterogeneity. Norman et al. (2003) found similar results based on a 24-m resolution dataset. Moreover, we found that over such heterogeneous areas the representativeness and appropriateness of a local scale based measurement such as BR and EC systems should be investigated. In other words, to what extent that the BR systems can be representative and appropriate for capturing surface variability? Despite the fact that the three BR systems were distributed over the area to capture the surface variability, it appears that this was not sufficient. This was noticed when we compared the TSEB model estimates of H with the measurements from the BR and LAS as described in paper 2 (Chapter 3). The estimates of H based on airborne dataset provided the lowest RMSE when compared with the LAS measurements instead of those from the BR. This clearly supports the fact that over such surface conditions it is better to use LAS instead of BR systems.

Extrapolated estimates of *ET* obtained by using the TSEB model provided better results when compared to those based on the M-S method. The RMSE for *ET* estimates were 1.23 and 1.6 mm day^{-1} based on the TSEB model and the M-S method, receptively. Note that the M-S method considerably depends on, or basically formulated on, h_c. However, it appears that its estimates based on 30-m pixel resolution compared to those based on the 1-m were almost similar. Note that we used the simple average method to aggregate the 1-m to 30-m pixel resolution h_c map and the average values were generally much lower. The M-S provided estimates of *ET* with a narrower range between 4-6 mm day^{-1} without having the ability to well capture the spatial variability of *ET* with regard to those of the h_c maps. On the other hand estimates of *ET* obtained using the TSEB model manage to capture the wide range of the measured *ET* between 2-6 mm day^{-1} which an indication of its ability to well capture the associated surface variability. This finding may support the idea that the M-S method might be more suitable in its application to surfaces that exhibits some sort of homogeneity such as agricultural fields. We made no attempt to make such comparison, however, this can be considered for future research.

Implications of this research findings which may be considered for future studies include a) the hybrid *ET* approach may support and improve estimates of crop water requirements and generally the way we manage our water resources, b) indications from the application of scintillometry may improve how spatial model estimates of fluxes compare, or at least give indications of the related degree of uncertainty, c) support future applications of using scintillometer in validating spatial estimates of SEBF (e.g. Kleissl et al. 2009), d) provide indications of what would be the optimal pixel resolution to reasonably capture spatial variability over different types of surfaces, e) may help

scientists and decision makers to identify configuration of future satellite designs in terms of temporal and spatial resolutions. Note that these issues were the main objectives of the NASA/USDA workshop on *ET* held in Silver Spring, Maryland, USA in 5-7 April, 2011.

5.2 Recommendations

Remote sensing techniques could be the best way to improve estimates of seasonal *ET*. However, there is a need to explore methods to overcome the issue of temporal resolution that may arise when using data from Landsat 5/7. The Hybrid *ET* approach described can be considered on of these methods. However, information or estimates of K_{cbrf} are not yet available for different types of vegetation. This may be considered for future research to provide such important variable. It is also recommended to examine other assimilation methods such as those using by Crow et al. (2008) as it could provide different indications or possibly better results.

Understanding the scale of heterogeneity of the specific area and pre-analysis of the wind conditions are crucial steps in determining the proper LAS layout. Also the use of LiDAR data are very important over heterogeneous areas especially where random distribution of vegetation exists such as over riparian zones in arid and semi-arid regions. However, the use of LiDAR might not be necessary over agricultural areas even at low vegetation covers during early growing season. During the period of study h_c was constant and so *LAI*. The effect of a chancing h_c and *LAI* need to be considered in the future. The use of other method in obtained h_c maps need to be studied in case of unavailability of LiDAR data. In addition it will also be important to study the effect of LAS height on estimates of *H*.

It is clear that higher pixel resolutions of < 30-m are needed when using remote sensing to estimated SEBF especially over heterogeneous surfaces such as areas with riparian or, generally, natural vegetation. Using local scale type of ground based measurements as BR or EC methods may be reasonable for verification purposes, however, we recommend the use of areal based measurements like scintillometers as it provide better coverage. Extrapolation of instantaneous *LE* flux to daily *ET* estimates over natural vegetation surfaces needs more attention since violation of assumptions of some of the methods is possible. The application of the Matt-Shuttleworth methods over natural vegetation may need some improvements as it failed to fully capture surface spatial variability effects.

References

Allen, R. G., L. S. Pereira, D. Raes, and M. Smith, 1998: *Crop evapotranspiration: Guidelines for computing crop water requirements.* Paper No. 56. Food and Agricultural Organization of the UN, 328 pp.

Bausch, W. C., 1993: Soil background effects on reflectance-based crop coefficients for corn. *Remote Sens. Environ.,* 46, 213–222.

Crow, W. T., W. P. Kustas, and J. H. Prueger, 2008: Monitoring root-zone soil moisture through the assimilation of a thermal remote sensing-based soil moisture proxy into a water balance model, *Remote Sens. Environ.*, **112,** 1268–1281

Daley, R., 1991: *Atmospheric Data Analysis*. Cambridge University Press, 457 pp.

De Bruin, H. A. R., B. J. J. M. van den Hurk, and W. Kohsiek, 1995: The scintillation method tested over a dry vineyard area. *Bound.-Layer Meteor.,* **76,** 25-40.

Kleissl, J., S.-h. Hong, and J. M. H. Hendrickx, 2009: New Mexico scintillometer network in support of remote sensing, and hydrologic and meteorological models. *Bull. Amer. Meteor. Soc.*, **90,** 207-218, DOI:10.1175/2008BAMS2480.1

Kustas, W. P., J. L. Hatfield, and J. H. Prueger, 2005: The Soil Moisture–Atmosphere Coupling Experiment (SMACEX): Background, hydrometeorological conditions, and preliminary findings. *J. Hydrometeor.*, **6,** 791–804.

Luo, Y., Z. Ouyang, G. Yuan, D. Tang, and X. Xie, 2003: Evaluation of macroscopic root water uptake models using lysimeter data. *Trans. Amer. Soc. Agric. Engin.*, **46(3),** 625–634.

Meijninger, W. M. L., O. K. Hartogensis, W. Kohsiek, J. C. B. Hoedjes, R. M. Zuurbier, and H. A. R. De Bruin, 2002a: Determination of area-averaged sensible heat fluxes with a large aperture scintillometer over a heterogeneous surface—Flevoland field experiment. *Bound.-Layer Meteor.* **105,** 37–62.

Meijninger, W. M. L., O. K. Hartogensis, W. Kohsiek, J. C. B. Hoedjes, R. M. Zuurbier, and H. A. R. De Bruin, 2002b: Determination of area-averaged water vapor fluxes with a large aperture and radio wave scintillometer over a heterogeneous surface—Flevoland field experiment. *Bound.-Layer Meteor.,* **105,** 63–82.

Neale, C. M. U., W. C. Bausch, and D. F. Heermann, 1989: Development of reflectance-based crop coefficients for corn. *Trans. Amer. Soc. Agirc. Engin.*, **32(6),** 1891–1899.

Norman, J. M., M. C. Anderson, W. P. Kustas, A. N. French, J. Mecikalski, R. Torn, G. R. Diak, T. J. Schmugge, and B. C. W. Tanner., 2003: Remote sensing of surface energy fluxes at 10^1-m pixel resolutions. *Water Resourc. Res.,* **39(8),** 1221, doi:10.1029/2002WR001775.

Norman, J. M., W. P. Kustas, and K. S. Humes, 1995: A two-source approach for estimating soil and vegetation energy fluxes in observations of directional radiometric surface temperature. *Agric. Forest Meteor.,* **77,** 263–293.

Sellers, P. J., Y. Mintz, Y. C. Sud, and A. Dalcher, 1986: A simple biosphere model (SIB) for use within general circulation models. *J. Atmos. Sci.*, **43,** 505–531.

Sheikh, V., S. Visser, and L. Stroosnijder, 2009: A simple model to predict soil moisture: Bridging Event and Continuous Hydrological (BEACH) modeling. *Environ. Modeling Software*, **24,** 542-556.

Shuttleworth, W. J., 2006: Towards one-step estimation of crop water requirements, *Trans. Ameri. Soc. Agric. Biolog. Engin.*, **49,** 925-935.

Suleiman, A. A., 2008: Modeling daily soil water dynamics during vertical drainage using the incoming flow concept, *CATENA*, **73,** 312-320.

APPENDICES

Appendix A

Description of the Soil Moisture Dynamics Model

The soil moisture dynamics model as described in the main body of the paper 1 (Chapter 2) by Eq. (21) require the calculation of the infiltration, soil water uptake, leakage between layers and drainage from the bottom most layer.

The infiltration of water at the soil surface in to the soil profile is estimated using Eq. (A1) as described in the daily multi-layered water balance (DAMUWAB) by Verdoodt et al. (2005).

$$I = \min\left(P + SS_{ini}, D_1\left(\theta_{sat} - \theta_{fc}\right)\right) \tag{A1}$$

where P is the precipitation, SS_{ini} the initial water storage at the soil surface which represents the amount of water supply that exceeds the infiltration capacity with a maximum storage of SS_{max} and the excess water lost at the surface as runoff (Verdoodt et al. 2005).

$$SS_{\max} = 0.5r\left(\frac{\sin^2(\sigma - \phi)}{\sin\sigma}\right)\left(\frac{1/\tan(\sigma + \phi) + 1/\tan(\sigma - \phi)}{2(\cos\sigma)(\cos\phi)}\right) \tag{A2}$$

where r is the surface roughness which varies between 70 to 15 mm for light tilled and untilled land, respectively, σ the clod angle or furrow angle in radians which varies between 0.5 - 0.8 rad, and ϕ the field declination.

The soil evaporation estimates from the WB were used as an input to the dynamic soil moisture model.

Leakage of water between adjacent layers from layers i to layer i+1 is estimated using Eq. (A3) as described in the BUDGET model by Raes (2002).

$$Q_{i,i+1} = D_i * \tau_i * (\theta_{sat,i} - \theta_{fc,i}) \frac{e^{\theta_i - \theta_{fc,i}} - 1}{e^{\theta_{sat,i} - \theta_{fc,i}} - 1} \quad \text{(A3)}$$

$$\tau_i = 0.0866 * e^{0.8063 \log 10(K_{sat})} \quad \text{(A4)}$$

where θ_s is the soil moisture content at saturation, θ_{fc} the soil moisture content at field capacity, K_{sat} the saturated hydraulic conductivity, and τ the drainage characteristic.

The deep percolation or the drainage from the bottom-most layer is estimated using as $Q_n = K_n \sin x$, where K_n is the hydraulic conductivity of the bottom-most layer, and x the slope angle, taken as 3 degrees as described in the simple biosphere model SiB by Sellers et al. (1986) and Luo et al. (2003).

The water uptake by plants root is initially estimated using Eq. (A6) as described by Prasad (1988) and Verdoodt et al. (2005) assuming unstressed water conditions.

$$S_i = 2 * \left(1 - \frac{D_{ri,0.5}}{D_r}\right)\left(\frac{D_{ri}}{D_r}\right) * Tr \quad \text{(A6)}$$

where T_r is the total transpiration amount from the entire root zone, D_{ri} the extension of the root zone with in the soil layer i, $D_{ri,0.5}$ the soil depth in the middle of extension of root in the soil layer i, and D_r the rooting depth. The initial value of S_i is used to initialize soil moisture content all soil layers and the corresponding soil water potential ψ. Under water limited conditions, the water uptake by plant roots is then adjusted to account for water stress conditions using the approach described in the SWATRE model by Feddes et al. (1976, 1978), Li et al. (2001), and Luo et al. (2003) as

$$S_i = \frac{\alpha_i^2 F^{\lambda}(z)}{\int \alpha F^{\lambda}(z) dz} Tr \quad \text{(A7)}$$

where α is the dimensionless Feddes reduction function estimated based on ψ (Eq. A8), λ coefficient with suggested values > 1.1 by Passioura (1985) and 0.5 by Li et al. (2001), and *F(z)* the specific root fraction function with respect to the soil depth z estimated using Eq. (A9) (Li et al. 2006).

$$\alpha(\psi) = \begin{cases} 0 & \psi \geq \psi_1 \\ \dfrac{\psi_1 - \psi}{\psi_1 - \psi_2} & \psi_2 \leq \psi < \psi_1 \\ 1 & \psi_3 \leq \psi < \psi_2 \\ \dfrac{\psi - \psi_4}{\psi_3 - \psi_4} & \psi_4 \leq \psi < \psi_3 \\ 0 & \psi \geq \psi_4 \end{cases} \tag{A8}$$

$$F(z) = -\beta^z \ln(\beta) \tag{A9}$$

$$\beta = 0.01^{\left(1/d_r\right)} \tag{A10}$$

where β is an empirical fitting parameter that determines the root distribution with depth and can be estimated using Eq. (A10), d_r the rooting depth, ψ_1 oxygen deficiency point or soil water potential at saturation, ψ_4 soil water potential at wilting, ψ_2 and ψ_3 are maximum soil water potential head for which the crop is not water stressed with ψ_2 corresponds to soil moisture potential at field capacity and ψ_3 changes with the atmosphere evaporative demand as shown in Fig. A1. Different sets of values for the ψ limits are reported in the literature and the values used in the study based on Clemente et al. (1994) as Fields 15–24 corn, ψ_1 = -0.10 m, $\psi 2$ =-0.25 m, $\psi 3$ = -5 m, $\psi 3$= -8 m, and ψ_4 = -160 m with similar limits used for Fields 16–24 soybean except that $\psi 3$ =-21 m and $\psi 1$ = -80 m.

References

Clemente, R.S., R. De Jong, H. N. Hayhoe, W. D. Renolds, and M. Hares, 1994: Testing and comparing of three unsaturated soil water flow models. *Agric. Water Manage.*, **25,** 135–152.

Feddes, R. A., P. J. Kowalik, K. Kolinska–Malinka, and H. Zaradny, 1976: Simulation of field water uptake by plants using a soil water dependent root extraction function. *J. Hydrol.*, **31,** 13–26.

Feddes, R. A., P. J. Kowalik, and H. Zaradny, 1978: *Simulation of Field Water Use and Crop Yield*. Centre for Agricultural Publishing and Documentation, 188 pp.

Li, K. Y., R. De Jong, M. T. Coe, and N. Ramankutty, 2006: Root-water-uptake based upon a new water stress reduction and an asymptotic root distribution function. *Earth Interact.*, **10,** 1–22.

Li, K.Y., R. De Jong, and J. B. Boisvert, 2001a: An exponential root-water-uptake model with water stress compensation. *J. Hydrol.*, **252,** 189–204.

Luo, Y., Z. Ouyang, G. Yuan, D. Tang, and X. Xie, 2003: Evaluation of macroscopic root water uptake models using lysimeter data. *Trans. Amer. Soc. Agric. Engin.*, **46(3),** 625–634.

Passioura, J. B., 1985: Roots and water economy of wheat. *Wheat Growth and Modeling,* W. Day and P. R. Atkin, Eds., Plenum Press, 185–198.

Prasad, R., 1988: A linear root water uptake model. *J. Hydrol.*, **99,** 297–306.

Raes, D., 2002: BUDGET: *A Soil Water and Salt Balance Model Reference Manual Version 5.0*. Catholic University of Leuven, 79 pp.

Sellers, P. J., Y. Mintz, Y. C. Sud, and A. Dalcher, 1986: A simple biosphere model (SIB) for use within general circulation models. *J. Atmos. Sci.*, **43,** 505–531.

Verdoodt, A., E. van Ranst, L. Ye, and H. Verplancke, 2005: A daily multi-layered water balance model to predict water and oxygen availability in tropical cropping systems. *Soil Use Manage.*, **21(3),** 312–321.

Appendix B

Soil Water Characteristics

The saturated hydraulic conductivity (K_{sat}), θ_{fc}, and the permanent wilting point (θ_{PWP}) for each soil type were estimated using the soil water characteristic model developed by Saxton and Rawls (2006) based on the U.S. Department of Agriculture (USDA) soil database that covers most of the US soils, ψ and K were estimated following the formulation of Clapp and Hornberger (1978) as

$$\psi = \psi_s \left(\frac{\theta}{\theta_s} \right)^{-b} \tag{B1}$$

$$K = K_{sat} \left(\frac{\theta}{\theta_s} \right)^{2b+3} \tag{B2}$$

where ψ_s is the soil water potential at saturation, b empirical constant with different values tabulated for each soil type by Clapp and Hornberger (1978). The soil physical properties and water characteristics for each of the four analysis fields are shown in Table B1.

References

Clapp, R. B., and G. M. Hornberger, 1978: Empirical equations for some hydraulic properties. *Water Resour. Res.*, **14(4),** 601–604.

Saxton, K. E., and W. J. Rawls, 2006: Soil water characteristic estimates by texture and organic matter for hydrologic solutions. *Soil Sci. Soc. Amer. J.*, **70,** 1569–1578.

Table B1. Soil water characteristics used in the water balance analysis for each of the four fields.

Field ID	Crop type	Sand (%)	Clay (%)	OM[a] (%)	WHC[b] (m3 m^{-3})	θ_{FC}[c] (m^3 m^{-3})	θ_{PWP}[d] (m^3 m^{-3})	K_{sat}[e] (mm day^{-1})
Field 15	Corn	24	30	6.0	0.17	0.37	0.20	421.2
Field 16	Soybean	16	29	5.5	0.18	0.38	0.20	422.88
Field 23	Soybean	23	18	3.9	0.19	0.32	0.13	529.92
Field 24	Corn	23	18	3.9	0.19	0.32	0.13	529.92

[a] OM is the organic matter content in volumetric percentage.
[b] WHC is the water holding capacity.
[c] θ_{FC} is the soil moisture content at field capacity.
[d] θ_{PWP} is the soil moisture content at permanent wilting point
[e] K_{sat} is the saturated hydraulic conductivity.

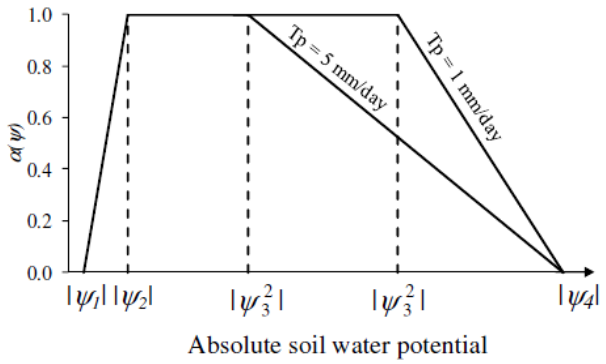

Fig. B1. Schematic showing the variation of Feddes reduction function $\alpha(\psi)$ with respect to soil water potential ψ and potential transpiration T_P.

Appendix C

Scintillometer Weighting Function

The scintillometer spatial weighting function $W(u)$ can be estimated as

$$W(u) = 16\pi^2 K^2 L \int_0^\infty k\phi_n(k)\sin^2\left[\frac{k^2 Lu(1-u)}{2k}\right]\left[\frac{2J_1(x_1)2J_1(x_2)}{x_1 x_2}\right]^2 dk \qquad \text{(C1)}$$

where $u = x/L$ is the dimensionless coordinate along the LAS path L, $K = 2\pi/\lambda$ the optical wavenumber, k the turbulent spatial wavenumber, $\phi_n(k) = 0.033k^{-11/3}$, $J_1(x_1)$ and $J_1(x_2)$ Bessel functions of the first kind with $x_1 = kDu/2$ and $x_2 = [kD(1-u)/2]$ where D is the aperture diameter. Example of $W(u)$ for the LAS used in this analysis is shown in Fig. C1.

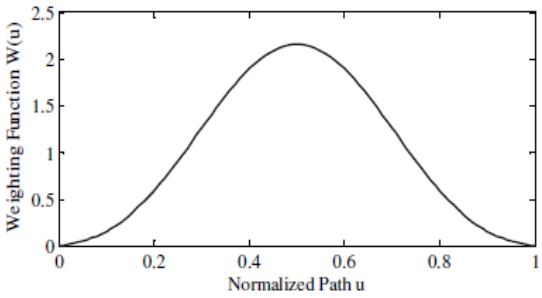

Fig. C1. The scintillometer weighing function $W(u)$.

Appendix D

Permissions

UtahState University
Department of Civil and Environmental Engineering
4110 Old Main Hill
Logan, UT 84322-4110
Telephone: (435) 797-2932
Fax: (435) 797-1185

1-15-2012

William P. Kustas
USDA-ARS Hydrology and Remote Sensing Laboratory
Bldg. 007, Rm. 104, BARC-West
Beltsville, MD 20705-2350

Dear William,

I am in the process of preparing my dissertation in the Civil and Environmental Engineering Department at Utah State University. I Hope to complete my degree in January of 2012.

I am requesting your permission to include the attached paper, of which you are a coauthor, as a chapter in my dissertation. I will include acknowledgments to your contribution as indicated. Please advise me of any changes you require.

Please indicate your approval of this request by signing in the space provided, attaching any other form or instruction necessary to confirm permission. If you have any questions, please contact me.

Thank you

H. M. E. Geli

Hatim M. E. Geli

I hereby give permission to Hatim M. E. Geli to use and reprint all of the material that I have contributed to Chapter 2 of his dissertation.

William P. Kustas

UtahState
University
Department of Civil and Environmental Engineering
4110 Old Main Hill
Logan, UT 84322-4110
Telephone: (435) 797-2932
Fax: (435) 797-1185

1-15-2012

Doyle Watts
Department of Earth & Environmental Sciences
267 Brehm Lab
Wright State University
3640 Colonel Glenn Highway
Dayton, OH 45435

Dear Doyle,

I am in the process of preparing my dissertation in the Civil and Environmental Engineering Department at Utah State University. I Hope to complete my degree in January of 2012.

I am requesting your permission to include the attached paper, of which you are a coauthor, as a chapter in my dissertation. I will include acknowledgments to your contribution as indicated. Please advise me of any changes you require.

Please indicate your approval of this request by signing in the space provided, attaching any other form or instruction necessary to confirm permission. If you have any questions, please contact me.

Thank you

H.M.E.G

Hatim M. E. Geli

I hereby give permission to Hatim M. E. Geli to use and reprint all of the material that I have contributed to Chapter 3 of his dissertation.

Doyle Watts

UtahState
University
Department of Civil and Environmental Engineering
4110 Old Main Hill
Logan, UT 84322-4110
Telephone: (435) 797-2932
Fax: (435) 797-1185

1-15-2012

John Osterberg
U.S. Bureau of Reclamation,
Denver, Colorado

Dear John,

I am in the process of preparing my dissertation in the Civil and Environmental Engineering Department at Utah State University. I Hope to complete my degree in January of 2012.

I am requesting your permission to include the attached paper, of which you are a coauthor, as a chapter in my dissertation. I will include acknowledgments to your contribution as indicated. Please advise me of any changes you require.

Please indicate your approval of this request by signing in the space provided, attaching any other form or instruction necessary to confirm permission. If you have any questions, please contact me.

Thank you

H.M.E.Ga

Hatim M. E. Geli

I hereby give permission to Hatim M. E. Geli to use and reprint all of the material that I have contributed to Chapter 3 of his dissertation.

John Osterberg

UtahState
University
Department of Civil and Environmental Engineering
4110 Old Main Hill
Logan, UT 84322-4110
Telephone: (435) 797-2932
Fax: (435) 797-1185

1-15-2012

Henk A. R. De Bruin
Freelance consultant
Bilthoven, The Netherlands

Dear Henk,

I am in the process of preparing my dissertation in the Civil and Environmental Engineering Department at Utah State University. I Hope to complete my degree in January of 2012.

I am requesting your permission to include the attached paper, of which you are a coauthor, as a chapter in my dissertation. I will include acknowledgments to your contribution as indicated. Please advise me of any changes you require.

Please indicate your approval of this request by signing in the space provided, attaching any other form or instruction necessary to confirm permission. If you have any questions, please contact me.

Thank you

H.M.E.G.

Hatim M. E. Geli

I hereby give permission to Hatim M. E. Geli to use and reprint all of the material that I have contributed to Chapter 3 of his dissertation.

Henk A. R. De Bruin

UtahState
University
Department of Civil and Environmental Engineering
4110 Old Main Hill
Logan, UT 84322-4110
Telephone: (435) 797-2932
Fax: (435) 797-1185

1-15-2012

Wim Kohsiek
Formerly Royal Netherlands Meteorological Institute (KNMI)
De Bilt, The Netherlands

Dear Wim,

I am in the process of preparing my dissertation in the Civil and Environmental Engineering Department at Utah State University. I Hope to complete my degree in January of 2012.

I am requesting your permission to include the attached paper, of which you are a coauthor, as a chapter in my dissertation. I will include acknowledgments to your contribution as indicated. Please advise me of any changes you require.

Please indicate your approval of this request by signing in the space provided, attaching any other form or instruction necessary to confirm permission. If you have any questions, please contact me.

Thank you

H.M.E-Sa

Hatim M. E. Geli

I hereby give permission to Hatim M. E. Geli to use and reprint all of the material that I have contributed to Chapter 3 of his dissertation.

Wohsiek

Wim Kohsiek

UtahState
University
Department of Civil and Environmental Engineering
4110 Old Main Hill
Logan, UT 84322-4110
Telephone: (435) 797-2932
Fax: (435) 797-1185

1-15-2012

Robert T. Pack
Department of Civil and Environmental Engineering
Utah State University,
Logan, Utah 84322

Dear Robert,

I am in the process of preparing my dissertation in the Civil and Environmental Engineering Department at Utah State University. I Hope to complete my degree in January of 2012.

I am requesting your permission to include the attached paper, of which you are a coauthor, as a chapter in my dissertation. I will include acknowledgments to your contribution as indicated. Please advise me of any changes you require.

Please indicate your approval of this request by signing in the space provided, attaching any other form or instruction necessary to confirm permission. If you have any questions, please contact me.

Thank you

H.M.E.G.

Hatim M. E. Geli

I hereby give permission to Hatim M. E. Geli to use and reprint all of the material that I have contributed to Chapter 3 of his dissertation.

Robert T. Pack

CURRICULUM VITAE

Hatim M. E. Geli
4110 Old Main Hill
Logan, UT 4322-4110
hatim.geli@aggiemail.usu.edu

Education

PhD, Water Engineering, (Exp. September 2011)
Utah State University, Utah, USA GPA 3.81/4.0
Advisor: Christopher M. U. Neale

M.Sc., Water Resources Engineering, (March 2004)
University of Khartoum, Khartoum, Sudan GPA 7.71/10 (top 2% of class)
Thesis: "*Streamflow Forecasting Using Artificial Neural Network*"
Advisor: B. I. Barsi

B.Sc., Civil Engineering, (July 1999)
University of Khartoum, Khartoum, Sudan GPA 6.71/10 (top 5% of class)
Thesis: *"Subsurface Water Problem in Omdurman Town"* (Second Class Div. 1 Honors)
Advisor: B. I. Barsi

Research Interests

Application of remote sensing techniques in estimating surface energy fluxes and evapotranspiration using soil-vegetation-atmosphere transfer models, land surface models, data assimilation of remote sensing, spatially distributed hydrological models, and water resources planning and management.

Research experience

Remote Sensing

- Researched on the application of different soil-vegetation atmosphere transfer models SVAT such as the one-layer, the two-source model, and SEBAL, gained knowledge on the application of METRIC, in addition to land surface models such as NOAH LSM to estimate surface energy fluxes
- Researched on the application of scintillometery with LiDAR and energy balance models over different areas
- Developed VB interface that works within the ArcGIS for the efficient and fast application of some different energy balance models and a water balance model.
- Atmospheric correction of Landsat images using MODTRAN to produce at surface reflectance and radiometric surface temperature
- Satellite and airborne image processing using ERDAS imagine and ArcGIS

Hydrology

- Acquired applied knowledge on some surface water hydrologic models including HEC-ResSim, HEC-RAS, HEC-1/HMS, DAMBRK, SWMM, and the Sacramento Soil Moisture Accounting SAC-SMA of the NWS
- Acquired applied knowledge on groundwater resources management and planning using ModFlow groundwater model
- Developed a VBA interface that works within the ArcGIS for the application of TopModel modeling approach

Programming

- Developed a VB interface that works within the ArcGIS environment for the application of some energy balance models, acquired knowledge on application and use of ERDAS imagine software in image processing and spatial analysis, and used different research analysis tools using .Net, FORTRAN, MATLAB, and MATLAB Simulink

Teaching Experience

Instructor

University of Khartoum -Civil Engineering Department, Khartoum, Sudan (2004-2006)
Developed all aspects of course material including instructions, grading, preparing tests (quizzes, midterms, and finals), holding office hours, and assigning final grades: Hydrology and Computer Applications in Hydrology and Water Resources

Tutor/Grader

Utah State University, Logan, UT, USA (2006-2008)
Graded Engineering Economics

University of Khartoum -Civil Engineering Department, Khartoum, Sudan (1999-2004)
Teaching Assistant, including tutoring, grading, and assigning final grades: Hydrology, Hydraulics in conjunction with lab experiments in open channel Hydraulics, Irrigation Engineering, and Computer applications in hydrology and water resources

Refereed Publications

Geli, Hatim M. E., C. M. U. Neale, and W. P. Kustas. (Submitted February 2011): A Hybrid Approach for Improved Estimates of Evapotranspiration and Soil Moisture of the Root Zone in Agricultural Areas Using Remote Sensing and Data Assimilation Techniques, *Journal of Hydrometeorology*.

Geli, Hatim M. E., C. M. U. Neale, D. Watts, J. Osterberg, H. A. R. De Bruin, W. Kohsiek, R. T. Pack, and L. E. Hipps. (Accepted 2011): Scintillometer-base estimates of sensible heat flux using LiDAR-derived surface roughness, *Journal of Hydrometeorology*.

Presentations, Posters, and abstracts

Jose González-Piqueras, Hatim M. E. Geli, Christopher M. U. Neale, Claudio Babontín1, Isidro Campos1, Alfonso Calera, 2011: Estimation of Sensible Heat Flux over Irrigated Vineyard Trees, 3rd Scintillometer Workshop, Wageningen, Netherland.

Geli, H. M. E., C. M. U. Neale, and J. Osterberg, 2011: Evatranspiration: An Essential Observation for Climate Understanding and Efficient Water Management, NASA/USDA Workshop on Evapotranspiration, Maryland, USA.

Geli, H. M. E., S. T. Taghvaeian, C. M. U. Neale, R. Pack, D. R. Watts, and J. Osterberg, 2010: Estimation of Evapotraspiration of Tamarisk using Energy Balance Models with High Resolution Airborne Imagery and LIDAR Data, AGU Fall 10 Meeting, San Francisco, California, USA

Piqueras, J. G., H. M. E. Geli, C. M. U. Neale, C. Balbontin, I. Campos, and A. Calera, 2010: Scintillometer-based estimates of sensible heat flux over row oriented vineyard trees, AGU Fall 10 Meeting, San Francisco, California, USA.

Geli, H. M. E., C. M.U. Neale, D. Watts, J. Osterberg, and R. Pack, 2010, Incorporating LIDAR Data into Scintillometer-Based Estimation of Sensible Heat Flux Considering Different Atmospheric Stability Conditions, Remote Sensing and Hydrology 2010, Jackson Hole, Wyoming, USA.

Geli, H. M. E., and C. M.U. Neale, 2010, Spatial EvpoTranspiration Modeling Interface (SETMI), Remote Sensing and Hydrology 2010, Jackson Hole, Wyoming, USA.

Geli, H. M. E, C. M.U. Neale, D. Watts, S. Sritharan, 2010, Improved Scintillometer Estimates of Latent Heat and Sensible Heat Flux over Naturally Vegetated Heterogeneous Semi-arid Areas using LIDAR Data, Applied Remote Sensing of Evapotranspiration Conference, Las Vegas, NV, USA.

Geli, H. M. E., and C. M.U. Neale, 2009, A Hybrid Approach for Estimating Evapotranspiration Using Remote Sensing (HET), AGU Fall 09 Meeting, San Francisco, California, USA.

Geli, H. M. E., and C. M. U. Neale, 2009, Estimation of Spatial Evapotranspiration over Non-Irrigated Agricultural Areas using Two-source Energy Balance Model, Fifth Inter. Conf. Irrig. Drain., Salt Lake City, Utah, USA.

Geli, H. M. E., and C. M. U. Neale, 2008, Comparison of One-layer and the Two-source Energy Balance Model for the Estimation of Spatial Evapotranspiration over Irrigated Agricultural Areas, the 5th Spring Runoff Conf. and 14th Intermountain Meteor. Workshop, Utah State University, Logan, Utah, USA.

Professional Affiliations

American Geophysical Union (2007-2011).
American Meteorological Society (2008-2011).
U.S. Committee for Irrigation and Drainage (2008-2010)
International Association of Hydrological Sciences (2009-2011)
Sudan Engineering Society (2001-2011)
Sudan Engineering Council (2001-2011)